GEOPHYSICAL MEASUREMENT AND MONITORING OF PLANETARY ROCK GLACIER SURFACE PROCESSES

by

Tyler McGrew Meng

A Dissertation Submitted to the Faculty of the

DEPARTMENT OF PLANETARY SCIENCES

In Partial Fulfillment of the Requirements
For the Degree of

DOCTOR OF PHILOSOPHY

In the Graduate College

THE UNIVERSITY OF ARIZONA

2024

THE UNIVERSITY OF ARIZONA
GRADUATE COLLEGE

As members of the Dissertation Committee, we certify that we have read the dissertation prepared by: Tyler McGrew Meng

titled: Geophysical Measurement and Monitoring of Planetary Rock Glacier Surface Processes

and recommend that it be accepted as fulfilling the dissertation requirement for the Degree of Doctor of Philosophy.

Jack Holt — Date: Apr 23, 2024

Victor R. Baker
Victor R. Baker (Apr 24, 2024 09:44 PDT)
Victor R. Baker — Date: Apr 24, 2024

Shane Byrne — Date: Apr 23, 2024

Lynn Carter — Date: Apr 23, 2024

Christopher Harig — Date: Apr 23, 2024

Final approval and acceptance of this dissertation is contingent upon the candidate's submission of the final copies of the dissertation to the Graduate College.

I hereby certify that I have read this dissertation prepared under my direction and recommend that it be accepted as fulfilling the dissertation requirement.

Jack Holt — Date: Apr 23, 2024

Lunar and Planetary Laboratory, Planetary Sciences

DEDICATION

In memory of Mark Angeles.

TABLE OF CONTENTS

TABLE OF CONTENTS – *Continued*

LIST OF FIGURES

ABSTRACT

Buried glaciers with varying fractions of debris and ice (henceforth referred to as rock glaciers) are found in mountainous regions with transitional climates on both Earth and Mars. On both worlds, there are questions as to the thickness, composition, and evolutionary history of these types of landforms. A surface feature that is ubiquitous to rock glaciers across planetary settings is the transverse ridge and furrow morphology. Two endmember hypotheses exist for the formation mechanisms behind this morphology: climatic and compressional processes. This work uses in situ geophysical field data from terrestrial rock glaciers to evaluate the formation processes governing the ridge and furrow morphologies and to determine diagnostic characteristics for each type of ridge in order to infer the origins of the ridges observed on the analogous features on Mars. By determining these formation mechanisms and developing criteria for identifying climatic ridges, a climate record can be reconstructed by mapping the surface morphology of martian rock glacier populations. First, we review the prior work that this thesis builds on. Next, we present a novel method for using two ground-penetrating radar antenna configurations to measure rock glacier thickness, internal structure, and composition, all essential parameters for reconstructing an ice emplacement history. We then demonstrate the advancement of a photogrammetric change detection method for monitoring rock glacier surface motion using repeated imaging campaigns across drone, airborne, and satellite platforms. This section provides a snapshot into the three-dimensional change of rock glacier surfaces due to both ice flow and surface melt. The surface motion and internal structure measurements are then combined to determine the formation mechanisms for ridges on the terrestrial sites, providing criteria for ridge classification. The thesis concludes by applying these ridge formation criteria to four regions on Mars with dense rock glacier populations.

CHAPTER 1

Lithics and Ice: The Evolution of Rock Glaciers as Planetary Analogs

1.1 Rock glaciers on Earth and ridge formation hypotheses

The exploration of glaciated mountain terrains has long identified rock glaciers as transitional landforms with various processes governing their evolution. As their name suggests, rock glaciers are mixtures of ice and rock where the lithic component is delivered as rockfall and avalanche debris, and the distribution of this debris subsequently affects the ice mass balance of the rock glacier. The first detailed surveys of rock glacier populations were carried out in Alaska (Capps, 1910; Wahrhaftig and Cox, 1959). Both of these studies documented the characteristic transverse ridge and furrow morphology that is a significant identifying feature of rock glacier landforms. Wahrhaftig and Cox interpreted these features as being solely periglacial in origin (the ice within the rock glacier is sourced from liquid water infiltration and refreezing within the pore space of the rockfall debris), while Capps acknowledged the likely presence of various glacial and periglacial processes in a relatively small spatial area. Both processes involve the preservation of subsurface ice under an insulating overburden layer that significantly decreases the ablation of ice when the debris is thick enough to create a thermal barrier (Östrem, 1959).

Further investigations of other rock glacier sites fueled a heated debate regarding the origin of the ice within rock glaciers (Potter, 1972; Barsch, 1987). The "ice-cored" rock glacier proponents argued that some rock glaciers contain glacial ice that has has not melted and retains its original stratigraphy, essentially acting as a debris-covered glacier with thick debris (>50 cm) and a minimal or nonexistent accumulation zone during the present day (e.g. Potter (1972)). Skeptics of the ice-

Figure 1.1: Sourdough Rock Glacier (color; acquired via UAV) in Alaska, along with an analogous feature showing ridge and furrow morphology in Deuteronilus Mensae, Mars (black and white inset; cropped from HiRISE image ESP_017130_2255_RED). Both features are approximately 1 km wide at the toe.

cored conceptual model contended that rock glaciers are dominated by periglacial processes such as the interstitial infiltration of snowmelt and rainwater within a talus slope, freezing and thawing of an active layer, and viscous downslope creep of the surface (Barsch, 1987). Direct evidence for the glacial origin hypothesis was observed via a drill core that retrieved clean ice with crystal fabric orientations and geochemistry that support the glacigenic model (Potter et al., 1998; Steig et al., 1998).

The use of geophysical methods advanced the study of rock glaciers while un-

earthing more questions about rock glacier formation and evolution. In particular, ground-penetrating radar (GPR) provides a reliable method for non-invasive subsurface mapping of rock glaciers due to the low conductivity of ice at radio wavelengths. Multiple GPR surveys of rock glaciers across different regions revealed the presence of subsurface radar reflectors that dip towards the glacier's upstream direction (Berthling et al., 2000; Fukui et al., 2008; Monnier et al., 2009; Florentine et al., 2014; Petersen et al., 2018). The geophysical observation of the dipping reflectors, combined with the ridge and furrow morphology that is common on rock glaciers, led to multiple hypotheses regarding the formation and evolution of rock glacier structure and morphology. One hypotheses states that oscillations in climate causes changes in the relative accumulation rate of ice and debris, leading to the deposition of debris layers that are buried by ice accumulation and subsequently advect downslope while outcropping as transverse ridges at the glacier surface. GPR data from Mullins Glacier in the Antarctic Dry Valleys combined with cosmogenic surface exposure dating and a climate model supports this hypothesis, indicating that internal layering of rock glaciers can record climate oscillations due to orbital forcing (Mackay et al., 2014; Mackay and Marchant, 2016, 2017).

The other endmember hypothesis states that mechanical compression of the rock glacier and its supraglacial debris layer leads to the formation of surface ridges via englacial thrust faulting or viscous buckle folding of the debris layer (Fukui et al., 2008; Florentine et al., 2014). These compressional mechanisms have been conclusively shown to occur on a rock glacier in the Swiss Alps (Frehner et al., 2015), however there are no previous studies aimed at delineating compressional ridges from climate ridges on rock glaciers. Testing these hypotheses and determining the criteria for interpreting the formation mechanisms of specific ridges as climatic or compressional will directly inform paleoclimate reconstructions for rock glacier field sites that are not accessible for surface-based inquiry.

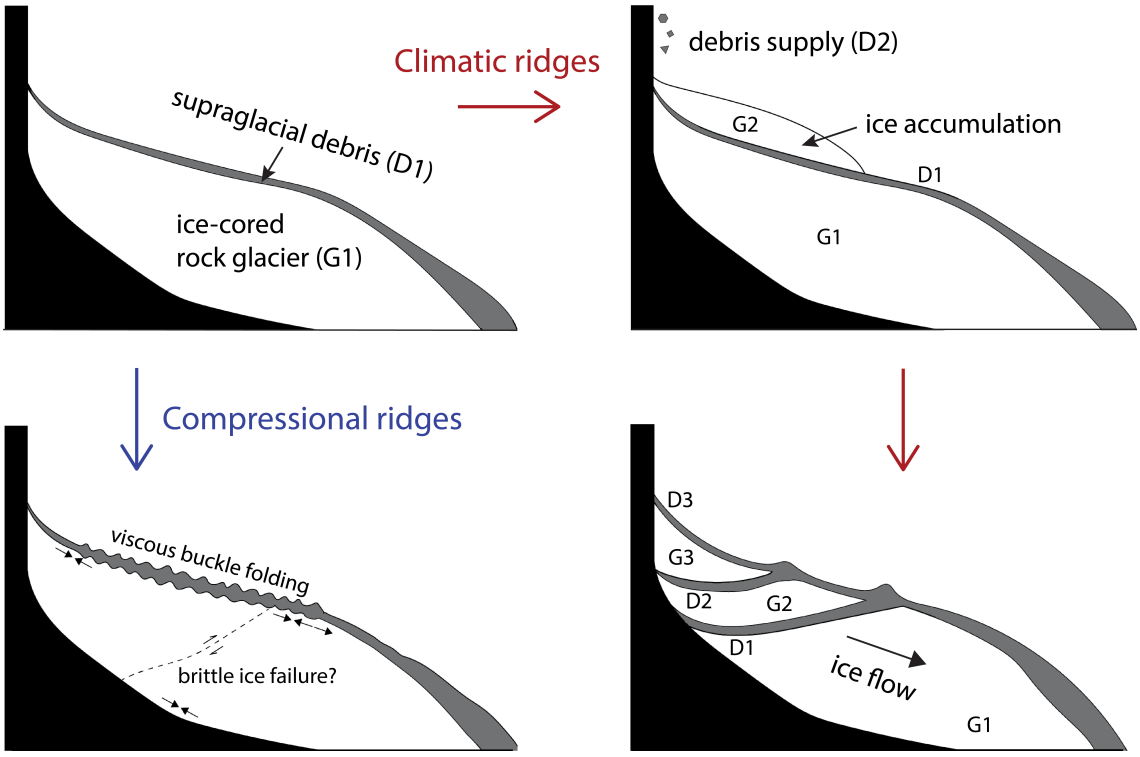

Figure 1.2: Schematic diagrams of endmember ridge formation hypothesis from the initial state of an ice-cored rock glacier (upper left). Ridges may form via compressional mechanisms (bottom left) or from climatic oscillations (top right and bottom right).

1.2 Rock glaciers on Mars as indicators of climate variability

As geophysical technology advanced the subsurface imaging capabilities for rock glaciers on Earth, this age of technological advancement also led to the dawn of planetary glaciology. Imagery acquired from the Viking orbiters revealed extensive landforms in the martian midlatitudes indicative of ground ice (Squyres and Carr, 1986). These landforms were described as lobate debris aprons and concentric crater fill. Global topography data acquired by Mars Orbiter Laser Altimeter (MOLA) revealed topographic smoothing above 30 degrees latitude in both hemispheres, and imagery from Mars Orbiter Camera (MOC) detected a latitude dependent dust mantle that exhibited evidence for multiple periods of deposition and removal (Head et al., 2003). These observations suggested oscillations of glacier accumulation and ablation in the midlatitudes driven by Mars' high-amplitude obliquity variations, leading to significant temperature oscillations and ice migration between the poles and equatorial regions (Laskar et al., 2002; Forget et al., 2006; Schorghofer, 2008).

The arrival of Mars Reconnaissance Orbiter, and specifically its Context Camera (CTX) instrument, provided imagery at 6 m/pixel over a significant portion of the planet. Significant efforts were undertaken to map the extent and surface morphology of these martian midlatitude glacial features, and it became apparent that these martian landforms are analogous to terrestrial debris-covered glaciers and rock glaciers with surface morphology consistent with obliquity-driven episodes of glacier accumulation (Morgan et al., 2009; Head et al., 2010; Baker et al., 2010; Fassett et al., 2014; Levy et al., 2014; Baker and Head, 2015). While the two planets differ greatly in surface temperature, atmospheric pressure, gravity, and several other factors, the strongest analogy between the martian and terrestrial populations of rock glaciers is their evidence of viscous flow and characteristic transverse ridge and furrow morphology. The transitional nature of both terrestrial and martian rock glaciers is also analogous; the martian population is found in the midlatitude

region transitioning from polar to equatorial climates, while rock glaciers and debris-covered glaciers on Earth are known to be transitional features between glacial and periglacial environments (Anderson et al., 2018).

In addition to the morphological mapping accomplished after the arrival of MRO at Mars, the spacecraft's Shallow Radar (SHARAD) instrument detected returns from the base of several of these glacial features (Holt et al., 2008; Plaut et al., 2009). After verifying the absence of off-nadir surface clutter, depth-correcting the basal return's travel time to agree with the elevation of the surrounding terrain suggests a dielectric constant consistent with nearly pure water ice. Hundreds of SHARAD tracks were analyzed and the results suggesting high-purity water ice remained consistent (Petersen et al., 2018). Despite this abundance of basal detections and the common ridge and furrow morphology for these features, SHARAD did not conclusively detect returns associated with englacial stratigraphy, such as the dipping reflectors analogous to those found in terrestrial rock glaciers. Still, geomorphic mapping of viscous flow features along with the identification of smaller glacier-like features (GLF) and the quantification of boulder density variation suggest that these glacial features have undergone multiple episodes of ice accumulation throughout the Amazonian period (Souness et al., 2012; Baker and Head, 2015; Levy et al., 2021).

This lack of internal reflectors in the martian debris-covered glaciers combined with the plethora of transverse ridges on their surface raises a question central to this work: how closely does the ridge and furrow surface morphology reflect englacial structure and stratigraphy, and what climate information can be inferred from this morphological connection with englacial layering. Previous work has mapped and classified ridges on a selection of martian midlatitude glacier surfaces with inconclusive results regarding the formation mechanisms (Stuurman, 2017).

This thesis presents a method for measuring and analyzing rock glacier structure and flow in order to determine the formation mechanisms of the transverse ridges

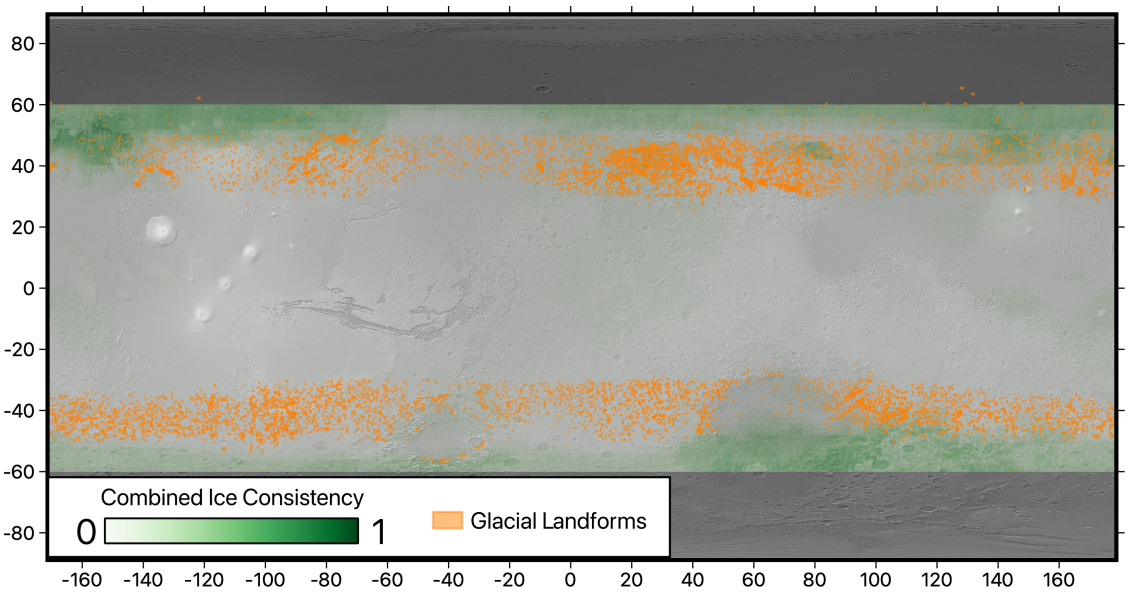

Figure 1.3: Global map of midlatitude glacial deposits on Mars and the consistency of remote sensing datasets with the presence of subsurface water ice below 60 degrees latitude (Levy et al., 2014; Morgan et al., 2021).

and to use identified climatic ridges to reconstruct paleoclimate scenarios for each planet. First, a method for measuring rock glacier thickness, debris thickness, internal structure, and composition with GPR is presented. Next, we use cross-platform photogrammetric methods to measure the three-dimensional surface change of our field sites, including horizontal flow and elevation change due to melt. We then perform a multidisciplinary geophysical analysis with both the GPR and the photogrammetric datasets to interpret the origin of individual ridges, create a gridded bed topography map, and evaluate the effects of driving stress and composition on rock glacier rheology. We conclude by using our interpretations and criteria for ridge formation on terrestrial rock glaciers to map stratigraphic contacts on selected martian features, and we give recommendations for applying our findings to future measurement campaigns on Earth and Mars.

CHAPTER 2

Rock Glacier Composition and Structure from Radio Wave Speed Analysis with Dipping Reflector Correction

2.1 Abstract

We assess the composition and geometry of four individual rock glaciers in Alaska, Wyoming and Colorado by measuring their radio wave speed and applying these results to ground-penetrating radar depth corrections and dielectric mixing models. Our method includes a correction for subsurface reflector dip angle, which we show can lead to an incorrect determination of wave speeds using common midpoint configurations. By observing the radar properties of the rock glaciers and their supraglacial debris, we find that some of the sites exhibit nearly pure ice cores, and all of the sites indicate volumetric ice fractions greater than 50%. These results have implications for terrestrial glaciology and hydrology because the present ice volume is connected to past ice accumulation and subsurface ice preservation, which may affect the future availability of alpine water resources. An understanding of the processes that govern rock glacier evolution over a wide range of latitudes and elevations will also contribute to the exploration of planetary surfaces such as Mars, which hosts a significant population of debris-covered glaciers. Our subsurface composition and geometry estimates will inform simulations of rock glacier formation and evolution to test hypothesized ice origin mechanisms along with the preservation of climate signals.

2.2 Publication in the Journal of Glaciology

This research was published in the Journal of Glaciology with coauthors Eric I. Peterson and John W. Holt, and a copy of the manuscript can be found in the Appendix of this dissertation. In the sections below, I present updated results for this study using the same methods to analyze 2022 and 2023 field data that were acquired after the publication of this article. Additionally, I have applied the techniques outlined in this publication to GPR data collected at Galena Creek in 2015 and 2016 to produce a holistic map of GPR measurements collected at our field sites to date.

As the lead author on this publication, I drove the survey design, I collected a significant amount of GPR data, I developed the novel analysis technique that uses a least squares approach with a dipping reflector correction to estimate the uncertainty envelope for radio wave speed measurements that use the common midpoint technique, and I led the writing and manuscript publication process. Not only does this publication present a method that will be essential for future GPR investigations of rock glaciers, but it also details several case studies at four individual rock glaciers. These case studies contribute to the expanding inventory of rock glacier datasets, which include ice and debris thickness measurements and volumetric ice fractions (RGIK, 2023).

2.3 Field data

Ground-penetrating radar (GPR) data was acquired at Galena Creek Rock Glacier in 2015, 2016, 2019, 2020, 2022, and 2023. GPR data was acquired at Sourdough Rock Glacier in 2015, 2018, 2019, 2021, and 2022. The results here present updates to the results from Meng et al. (2023b), which only included GPR data from 2018-2021 field campaigns and one common midpoint profile (CMP) from 2016 at Galena Creek. This updated dataset compiles all of the GPR measurements collected at

Galena Creek, Sulphur Creek, and Sourdough since 2015 (Petersen et al., 2019) and re-analyzes the wave speed and reflector depths using the least squares move out fit and dipping reflector correction method described in Meng et al. (2023b). The additions to the CMP dataset are as follows: two CMPs from 2015 at Galena Creek (one at the debris-covered glacier core site described by Clark et al. (1996) and one just below the debris-covered glacier/rock glacier transition), one CMP from 2015 at Sourdough, one CMP from the toe of the rock glacier directly to the east of Galena Creek in 2023, and one CMP from the toe of Sulphur Creek in 2023. We also collected 138, 297, and 915 m of new common offset data at 50, 100, and 200 MHz, respectively.

2.4 Updated results and discussion

2.4.1 Wyoming

The bulk rock glacier thickness The new CMP near the previous core site at Galena Creek is consistent with a geometrically complex subsurface that contains a pure ice unit along with dipping reflectors. Both the reflected wave and the refracted wave indicate a subsurface radio wave speed between 0.16 and 0.17 m/ns, which is consistent with a high ice fraction (Figure 2.1a).

The CMP near the DCG/RG transition indicates a significantly lower ice content in both the reflected and refracted wave. The CMP near the toe of East Galena Creek Rock Glacier, which represents the ice-poor end member scenario for this local population, indicates a wave speed of about 0.109 m/ns, demonstrating the transition from an ice-rich to ice-poor medium along the length of both rock glaciers.

2.4.2 Alaska

The addition of all CMP data collected at Sourdough revealed a trend in the wave speeds that generally increases down-glacier from 0.12 m/ns to 0.15 m/ns, suggesting

a higher ice content at the toe of the glacier than at the higher-elevation measurement points when using the two-phase dielectric mixing model. This observation may originate from multiple factors. First, the uppermost measurement, which has the lowest wave speed value of the Sourdough dataset, is located close to the western margin of the rock glacier in a region that exhibits crevasses and indicators of local extension (Meng et al., 2023a). At this location, it is possible that the ice fraction is significantly lower than at the rock glacier's toe due to its proximity to the glacier margins implying thicker ice along with the presence of crevasses that can enhance localized debris entrainment. However, this survey was conducted at an earlier time with an older system and potentially less accurate positioning information, demonstrating the importance of accurate positioning information when acquiring co-located common offset and common midpoint surveys.

2.5 Contribution and impact

This work contributes new measurements for ice thickness, debris thickness, internal structure, and composition for four rock glacier field sites. The method that was developed for measuring the ice fraction is novel and will significantly impact the rock glacier science community by providing a more robust technique to measure both the ice fraction along with an associated uncertainty envelope.

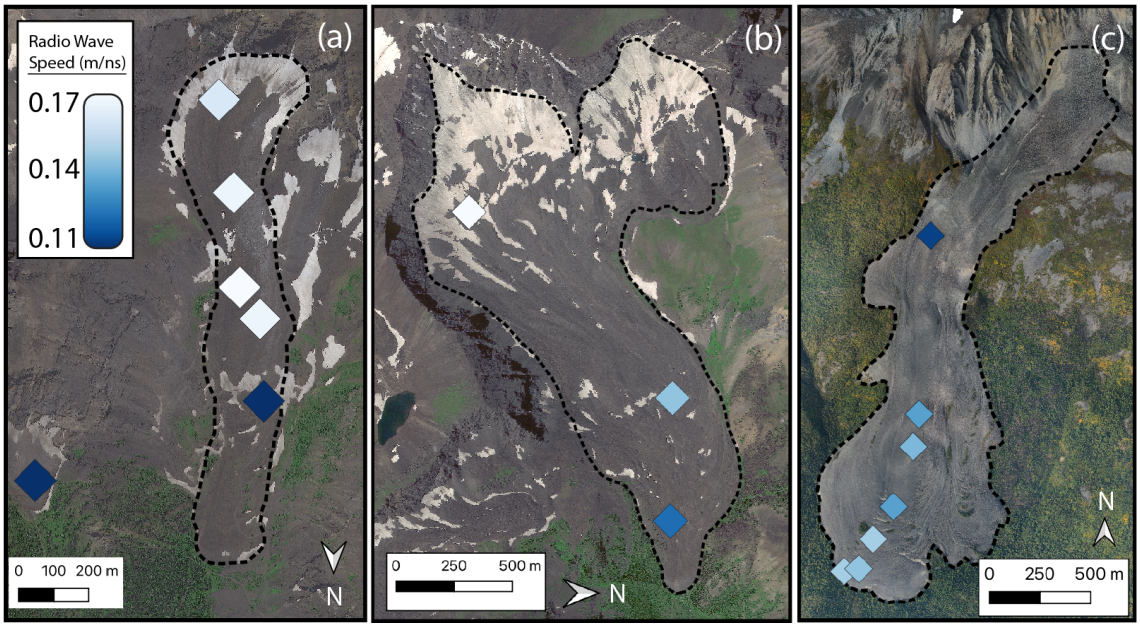

Figure 2.1: Updated map of bulk rock glacier radio wave speeds at (a) Galena Creek, WY, (b) Sulphur Creek, WY, and (c) Sourdough, AK.

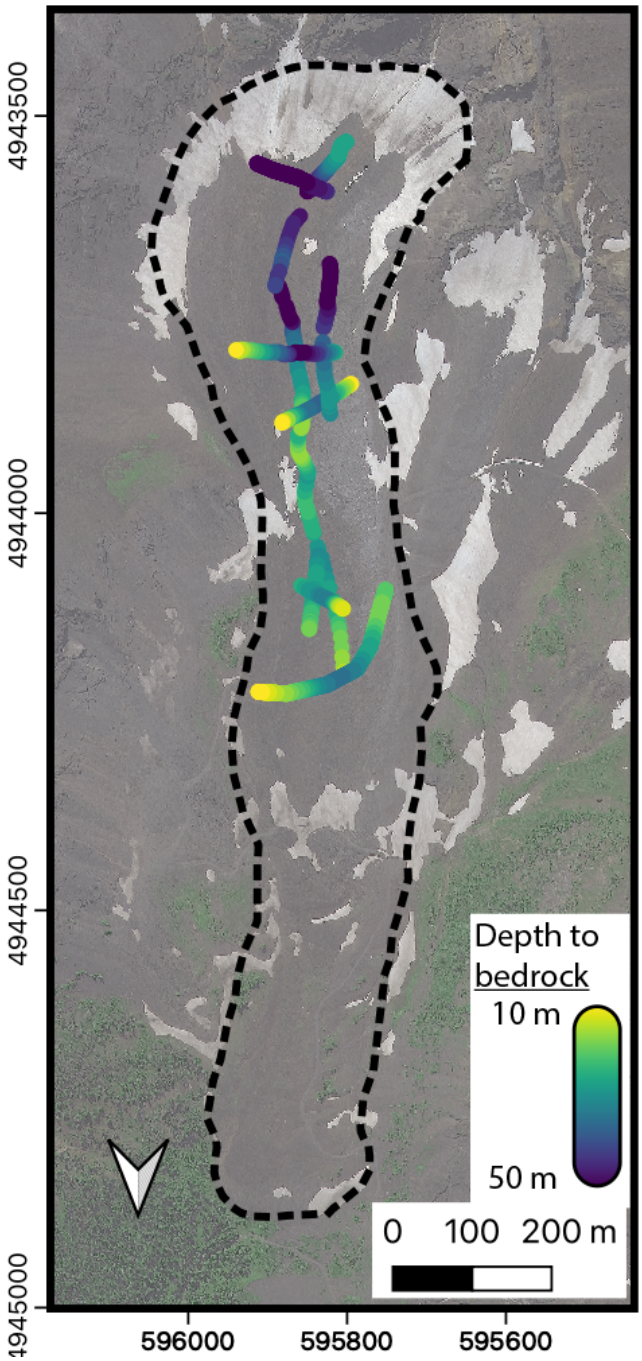

Figure 2.2: Updated map of bulk rock glacier thicknesses at Galena Creek, WY.

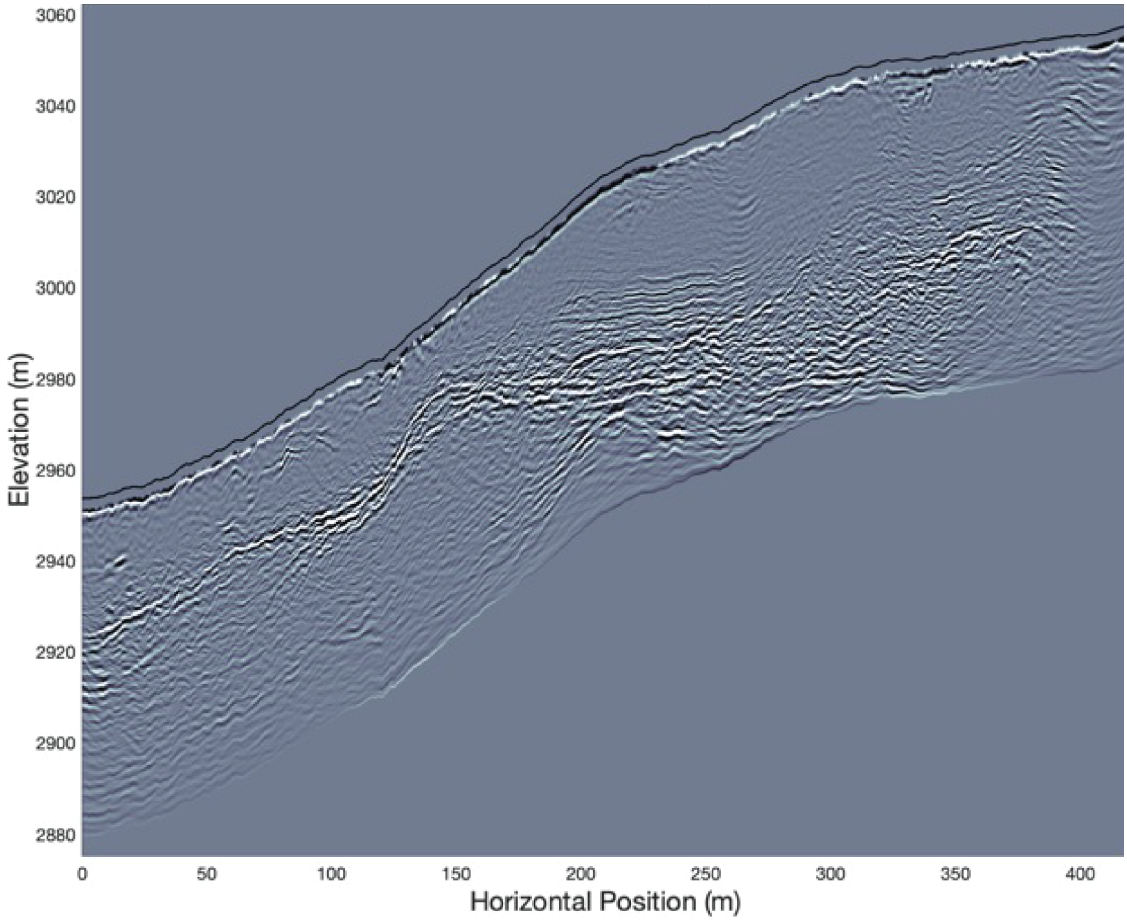

Figure 2.3: 50 MHz topographically corrected radargram using merged flow-parallel transects at Galena Creek acquired between 2019 and 2022. The rock glacier base is detected throughout, showing variations in rock glacier thickness along flow. The radio wave speed used for this transect is 0.165 m/ns.

CHAPTER 3

Photogrammetric Monitoring of Rock Glacier Motion Using High-resolution Cross-platform Datasets: Formation Age Estimation and Modern Thinning Rates

3.1 Abstract

The availability of remote sensing imagery at high spatiotemporal resolutions presents the opportunity to monitor the surface motion of rock glaciers, a key constraint for characterizing the dynamics of their evolution. In this paper, we investigate four North American rock glaciers by automatically measuring their horizontal surface displacement using photogrammetric data acquired with crewed and uncrewed aircraft along with orbital spacecraft over monitoring periods of up to eight years. We estimate vertical surface changes on these rock glaciers with photogrammetrically generated digital elevation models (DEM) and digitized topographic maps. Uncertainty analysis shows that the imagery with the highest resolution and most precise positioning have the best performance when used with the automated change detection algorithm. This investigation produces gridded velocity fields over the entire surface area of each study site, from which we estimate the age of rock glacier formation using along-flow velocity integration. Though the age estimates vary, the ice within the modern extent of these landforms began flowing between 3000 and 7000 years before present, postdating the last glacial maximum. Surface elevation change maps indicate present-day thinning at the lower latitude/higher elevation sites in Wyoming, while the higher latitude/lower elevation sites in Alaska exhibit relatively stable surface elevations.

3.2 Publication in Remote Sensing

This research was published in Remote Sensing with coauthors Roberto Aguilar, Michael Christoffersen, Eric Petersen, Chris Larsen, Joe Levy, and Jack Holt. A copy of the manuscript can be found in the Appendix of this dissertation. My contribution as the lead author of this study was to consolidate, process, and present the photogrammetry data that was acquired by the research team beginning at Sourdough, Alaska, in 2014. I contributed to the photogrammetric data collection by acting as the observer or pilot for UAV flights at the Wyoming field sites in 2020, 2022, and 2023, and I also contributed to the planning and execution the geodetic ground-control point survey used for the photogrammetric post processing. I produced the majority of the orthomosaics and DEMs used in the study using Agisoft Metashape photogrammetric processing software, and I also produced almost all of the displacement fields between image pairs using the automated change detection algorithm. Finally, I developed the analysis code to estimate the rock glacier's kinematic age and refined a thermal conduction model to validate the measured surface elevation changes. In the sections below, I present updated results for this study using the same methods to analyze 2023 field data that were acquired after the publication of this article.

3.3 2023 Field Data

In addition to the results presented in the published article, we collected photogrammetry data during our August 2023 field campaign to Galena and Sulphur Creek, Wyoming. We successfully acquired full orthophotos and DEMs of both rock glaciers, allowing us to perform an identical analysis to the methods present in the *Remote Sensing* publication. This is the first complete UAV photogrammetry survey covering Sulphur Creek, resulting in the highest-resolution orthomosaic of the landform to date. At 6.67 cm/pixel, this significantly improves the ability of the

change detection algorithm to detect surface motion relative to the 2020 airborne base image, which has a 10 cm/pixel resolution. In Meng et al. (2023a), the limiting resolution for Sulphur Creek was 42 cm/pixel due to the reliance on SkyMap50 satellite imaging. Decreasing the limiting resolution results in the ability to track smaller surface features over smaller displacements, allowing for more precise measurements. The 2023 Galena Creek orthomosaic is 3.56 cm/pixel, which is also an improvement from the 2020 and 2022 surveys.

3.4 Results

We acquired the first UAV orthomosaic of Sulphur Creek Rock Glacier, and this imaging supports previous inferences of rapid ice loss and surface subsidence in the upper part of the Sulphur Creek cirque. We also note that the toe of the lower rock glacier has an elevated surface velocity, indicating a potential destabilization and collapse of this region of the rock glacier (Figure 3.1).

To test the uncertainty and lower limit of displacement detections for the new datasets, we sampled a selection of off-glacier stable points to characterize the average measurement error. For 159 sample points at Galena Creek, the mean displacement was 4.5 cm and the standard deviation was 2.8 cm. For 238 sample points at Sulphur Creek, the mean displacement was 6.5 cm and the standard deviation was 10.1 cm. We perform an additional quality check by examining the distributions of the displacement magnitudes and maximum correlation coefficients output from the change detection algorithm (Figure 3.2).

To estimate the surface subsidence rate due to assumed ice melt, we used the new 2023 DEMs to measure elevation change for Galena Creek (e.g. Figure 3.3) and Sulphur Creek. The 2023 data shows subsidence rates on the order of 10 cm/yr, consistent with previous estimates (Meng et al., 2023a). While there is conclusive evidence of widespread thinning at both Wyoming rock glaciers with possible zones of extremely rapid melt, the measurement accuracy and precision is affected by an

apparent bias between the DEMs in each pair. For example, this bias appears as a systematic decrease in the stable terrain elevation for the 2020-2023 Galena Creek DEM pair. Future work should robustly address the specific causes of this bias, but for this photogrammetric method using ground-control points (GCP), the error in the stable terrain likely arises from two sources. One potential error source is the different UAV flight conditions for the acquisitions that occur years apart. While the surveys are flown using the same software-based flight plan for each campaign, differences in the weather have a real effect on the acquisition parameters. For example, wind may change the UAV battery efficiency and camera error, and the presence of clouds and shadows present different conditions affecting the final photogrammetric products. This effect may be particularly noticeable in steep terrain, such as the stable ground directly east of Galena Creek (Figure 3.3).

The second proposed source of bias in the DEM data stems from the GCPs used in the photogrammetric processing. The GCPs are not permanent, therefore they must be deployed and surveyed for each flight. As a result, the GCP locations and post processing parameters are not exactly the same for each flight; the exact parameters are detailed in the processing reports in the published supplementary materials (Meng et al., 2023a). The off-glacier GCP locations display the least bias in the elevation change maps, such as the terrain immediately north and west of the glacier outline. This indicates a high data fidelity for the locations near where the GCP are present. The rest of the GCPs are located on the glacier. The off-glacier stable terrain on the east side of the profile in Figure 3.3 has a steep slope and there is no GCP in this location, which may explain the systematic decrease in the elevation change data approaching the edge of the survey grid.

3.5 Contribution and impact

This work demonstrates the viability of using cross-platform imaging data sets for monitoring the three-dimensional motion of rock glacier surfaces. We discuss the

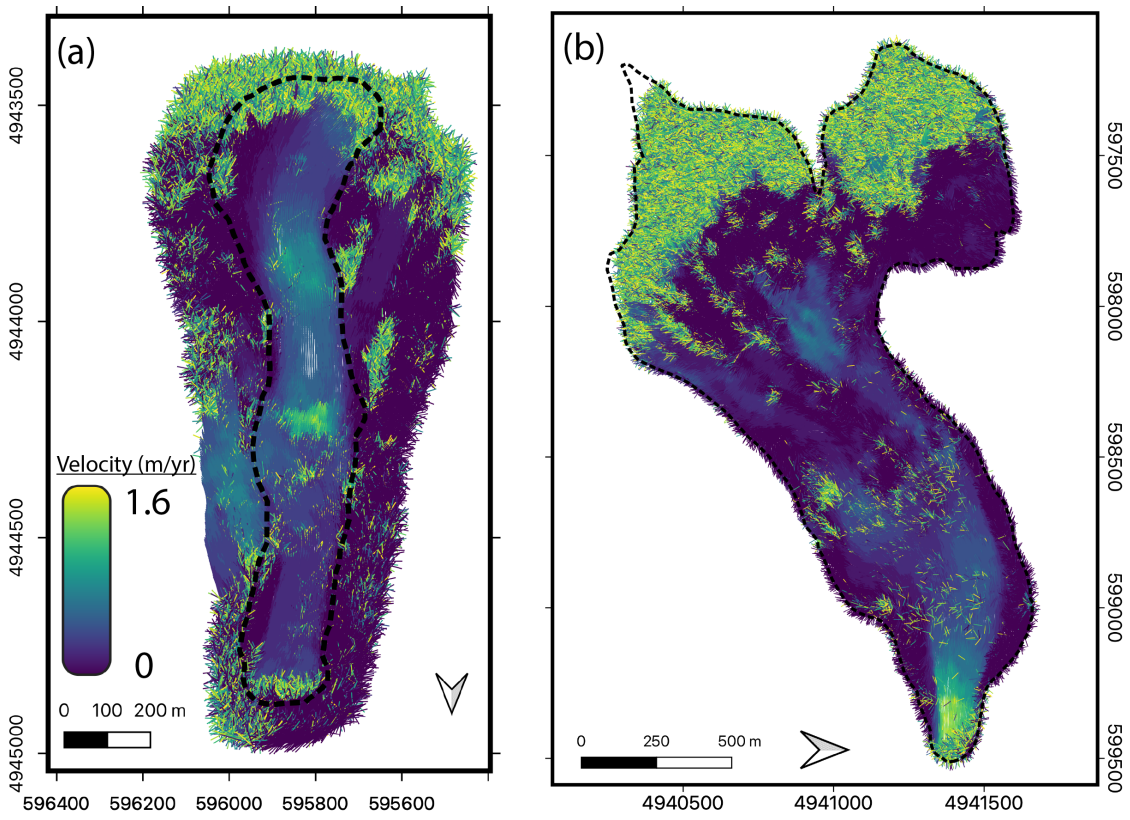

Figure 3.1: Surface velocity vector fields between August 2020 and August 2023 for (a) Galena Creek and (b) Sulphur Creek, WY. Both maps use the WGS 84/UTM 12N coordinate system and they have been rotated so that the predominant down-valley direction is roughly down on the page.

bias and uncertainty in the displacement measurements using the apparent displacement of stable terrain and we also examine the relationship between the quality of displacement measurements and the characteristics of histograms showing the distributions of displacement measurements. Finally, we use these kinematic data to estimate the ages of each of our rock glacier field sites. As a result, this study provides new time series of the surface change at each of our field sites while also presenting methods for evaluating the measurement uncertainty and the relationship of rock glacier surface motion with their estimated ages.

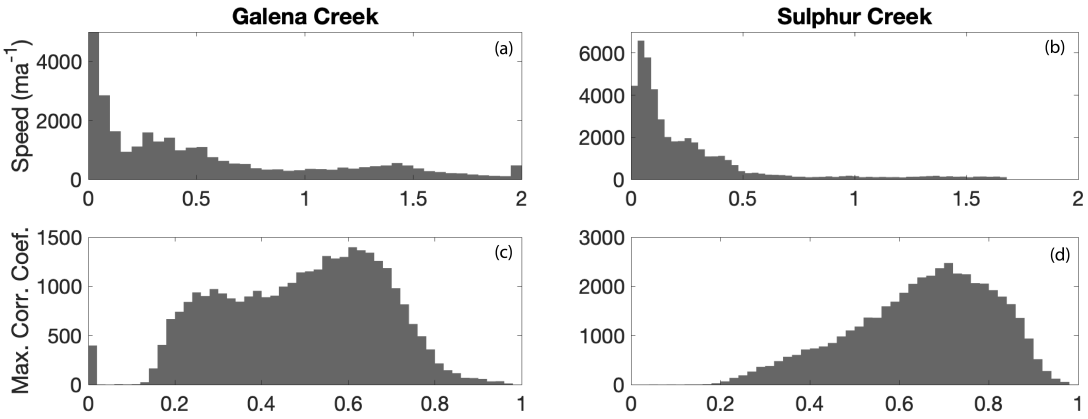

Figure 3.2: Updated histograms of surface velocities for Galena Creek (a) and Sulphur Creek (b) and the corresponding maximum correlation coefficients for each grid point on both Wyoming rock glaciers ((c) and (d)) using 2023 data.

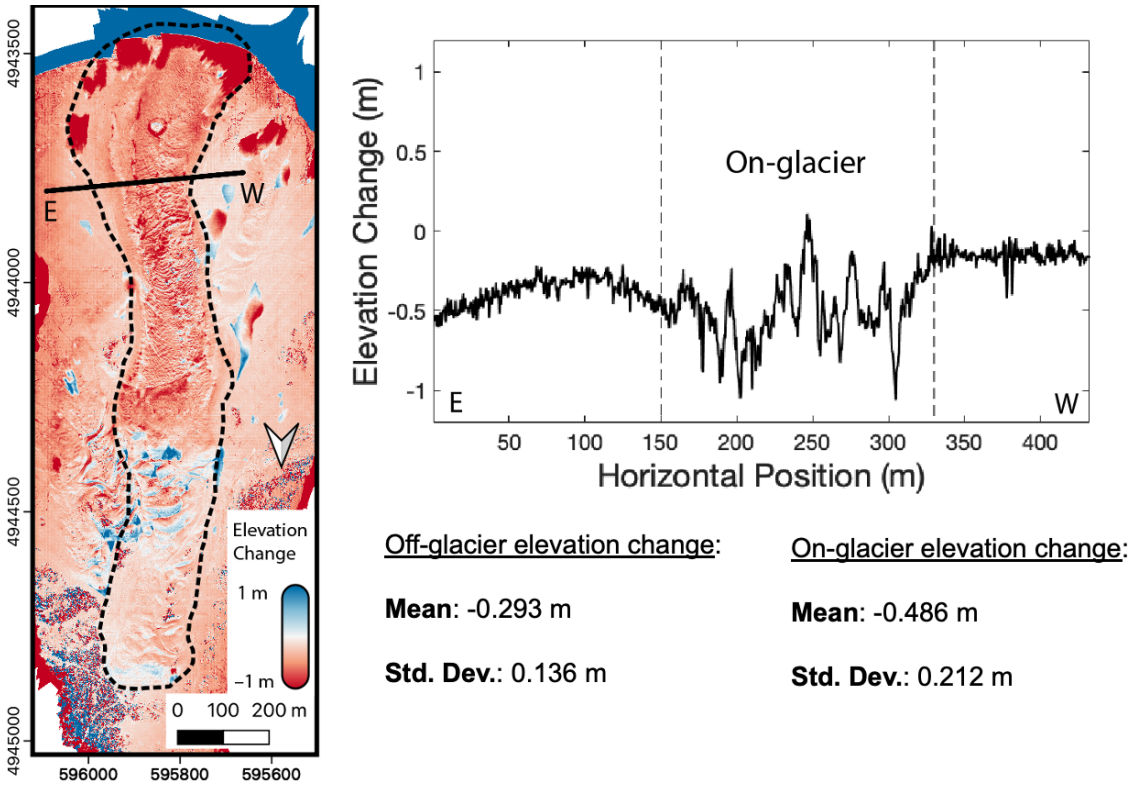

Figure 3.3: Galena Creek elevation change from 2020-2023, indicating approximately 20 cm of glacier surface subsidence and elevated variability relative to stable terrain. The off-glacier stable terrain also provides an indication for potential bias in each individual photogrammetric DEM.

CHAPTER 4

Effects of Rock Glacier Dynamics on Surface Morphology

4.1 Abstract

We apply static and kinematic geophysical measurements of rock glaciers to characterize active surface processes and to understand their effects on rock glacier dynamics. We primarily focus on the processes governing the formation of transverse ridge morphology, which include both compressional and climatic mechanisms. Supraglacial and englacial debris distribution imaged by ground-penetrating radar is examined in the context of high-resolution surface velocity measurements acquired via repeated drone photogrammetry surveys. We estimate the years of low ice accumulation represented by climatic ridges at Galena Creek, Wyoming, and we also observe evidence for active compressional ridge formation through a joint analysis of debris thickness distribution and surface strain. The strain analysis also has implications for mapping flow margins and regions of enhanced melt. To assist with efforts in numerically modeling rock glacier dynamics, we explore the multidisciplinary use of subsurface radar and surface velocity data to constrain the boundary conditions and rheological parameters necessary to simulate ridge formation and assist remote sensing data interpretation in terrestrial and planetary settings.

4.2 Introduction

One of the most ubiquitous features of rock glaciers, regardless of their location, is transverse arcuate furrow and ridge morphology. Not only are these ridges a common characteristic of rock glaciers on Earth, but they have also been documented on large debris-covered glaciers on Mars, which has led the Mars Polar Science community to

conclude that these terrestrial and martian landforms originated through analogous processes where subsurface ice is preserved by a thermal barrier created by the lithic overburden layer. With sufficient ice thickness, these deposits experience gravity-driven flow that is governed by the rheology of the subsurface ice/rock distribution.

We consider two different processes related to rock glacier flow contribute to this common transverse ridge morphology. These ridges are often referred to as "compressional ridges" (Frehner et al., 2015) because a common mechanism for ridge formation is the viscous buckle folding of the supraglacial debris layer under flow-induced compressional stresses. Strain rates on the order of $10^{-3}a^{-1}$ have been measured on rock glaciers in North America and Europe (Kääb and Vollmer, 2000; Leonard et al., 2005).

Additionally, subsurface imaging via ground-penetrating radar (GPR) has revealed the presence of dipping radar reflectors interpreted to be englacial debris bands that outcrop at the glacier surface in the form of transverse ridges. The debris bands are assumed to be prior supraglacial debris layers that amassed during a period of low ice accumulation, and these layers were subsequently buried during high ice accumulation, implying that rock glaciers have the potential to preserve climate signals on timescales ranging from decadal atmospheric oscillations to multi-millennial orbital variations related to the planet's Milankovitch cycles (Petersen et al., 2019; Mackay and Marchant, 2017). This presents an opportunity to use englacial debris stratigraphy as a proxy for paleoclimate signals. Further, if englacial stratigraphy preserves climate signals and these internal layers are also expressed unambiguously at the surface, climate signals may be inferred from surface morphology alone. This type of characterization could have implications for mapping the variability in paleoclimate indicators on rock glaciers where high-resolution subsurface geophysical data are unavailable, such as inaccessible mountainous terrain along with the midlatitudes of Mars, where there remains significant uncertainty regarding the accumulation and flow history of large debris-covered glacial deposits.

In addition to challenges in understanding the distribution of debris within and on top of the rock glacier and this distribution's relationship with ice kinematics and dynamics, the basal topography of rock glaciers and debris covered glaciers is notoriously difficult to map in a gridded fashion. This difficulty arises from the steep surface and subsurface slopes controlled by the regional high-relief terrain, which creates irregular GPR grids and complex basal geometries with no straightforward interpolation. Compositional heterogeneity, basal shearing, and diffuse reflections due to internal scattering also likely contribute to the uncertainty of GPR-derived basal topography of rock glaciers. Here, we explore three methods for creating basal topography maps for constraining flow models to test hypotheses related to paleoclimate and the flow of debris-rich ice. We apply our results to an analytical cross-flow velocity model to test rheological scenarios constrained by the derived rock glacier geometry.

4.3 Materials and Methods

4.3.1 Study Sites

We base our analysis primarily on photogrammetrically derived velocity fields of two pairs of rock glaciers. The first pair consists of the Galena Creek and Sulphur Creek rock glaciers systems in northwest Wyoming, USA (Figure 4.1). Galena Creek has one of the oldest bodies of scientific research for a rock glacier in the USA due to its relatively low latitude and ease of accessibility for data collection (Potter, 1972; Potter et al., 1998). This location served as a laboratory to test the debated hypotheses of the origins of the ice within rock glaciers, with an ice core retrieval ultimately supporting the inference that rock glaciers may be derived from debris-covered glaciers with relatively thick supraglacial debris layers (Clark et al., 1998; Steig et al., 1998). Despite its relatively close proximity to Galena Creek, Sulphur Creek has received much less scientific attention by comparison. Recent

field measurements have indicated the presence of glacial ice in the cirque, but it exhibits evidence of rapid ice melt and surface subsidence (Meng et al., 2023b,a). Galena Creek also shows a surface subsidence signal on its upper half, but it appears to be more stable than Sulphur Creek due to its thicker debris layer and ice mass.

The second pair of sites that we analyze is Sourdough and McCarthy Creek Rock Glaciers, Alaska, which respectively flow down the southern and northwestern slopes of Sourdough Peak. Only Sourdough has been measured for composition and structure using GPR (Meng et al., 2023b), but both Sourdough and McCarthy Creek were imaged in a repeat airborne photogrammetry campaign spanning from May 2014 to July 2022 (Meng et al., 2023a).

4.3.2 Strain Rate Mapping

To test the hypothesis of ridge formation via compressional buckle folding, we calculate the horizontal strain tensor components of the rock glacier using gridded displacement measurements derived from repeated photogrammetric overflights (Meng et al., 2023a). Horizontal surface displacement vectors are measured by applying a normalized cross-correlation change detection algorithm to repeated optical images of each rock glacier (Kääb and Vollmer, 2000; Heid and Kääb, 2012), providing an average surface velocity field for the time interval between images. The strain rate components are the gradients of the velocity's x and y components along each dimension, represented by i and j in the following equation (e.g. Cuffey and Paterson (2010)):

$$\dot{\epsilon}_{ij} = \frac{1}{2}(\frac{\delta u_i}{\delta x_j} + \frac{\delta u_j}{\delta x_i}), \tag{4.1}$$

This step produces two longitudinal strain rate maps ($\dot{\epsilon}_{xx}$ and $\dot{\epsilon}_{yy}$) and one shear map ($\dot{\epsilon}_{xy}$). We assess the relationships between the strain rate distributions and field observations of surface morphology recorded via photogrammetric digital elevation

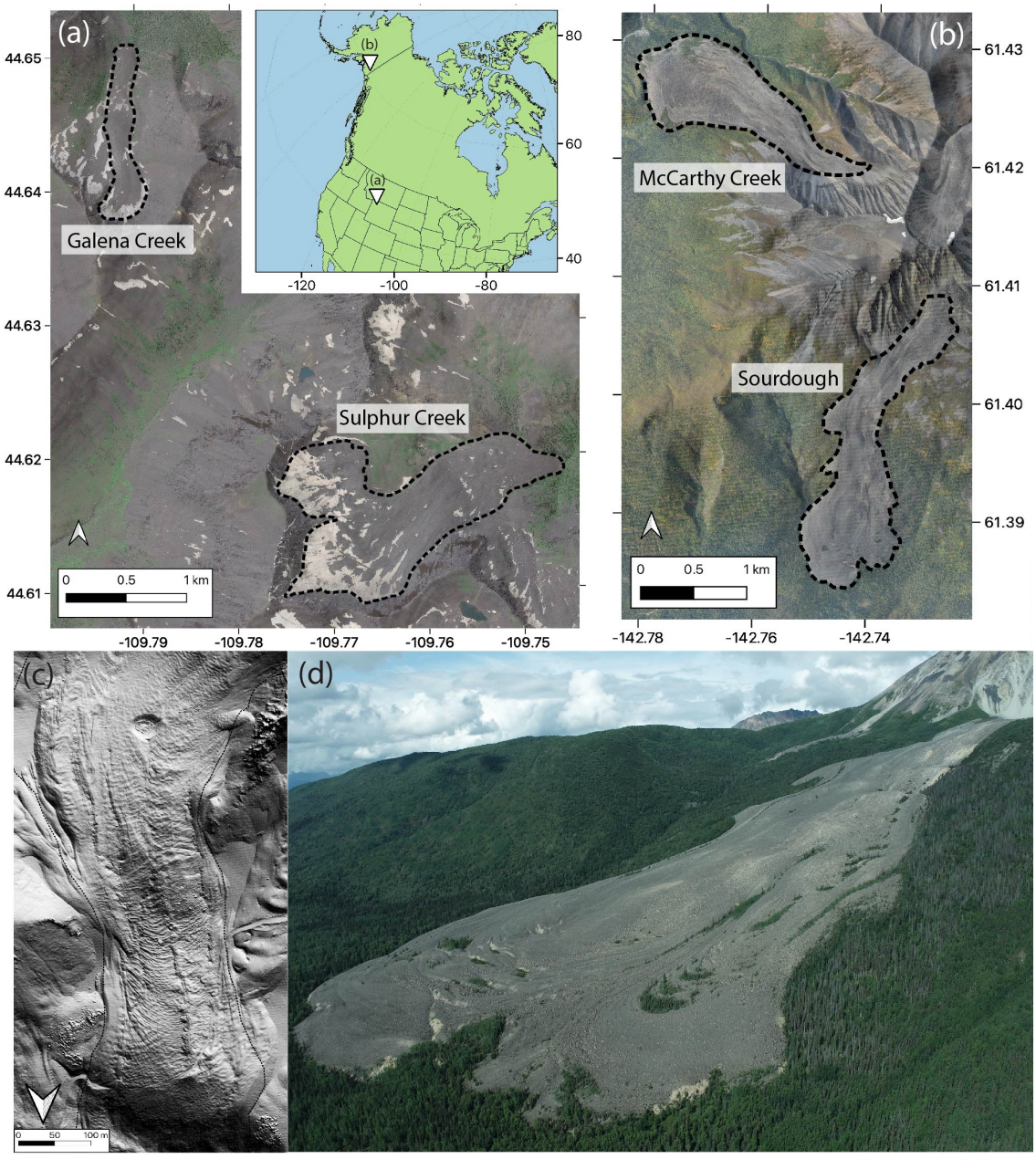

Figure 4.1: Context maps showing field sites for ridge formation analysis in Wyoming (a) and Alaska (b) along with examples of transverse ridge morphology apparent in shaded relief map at Galena Creek, WY (c), and oblique UAV image at Sourdough, AK (d).

models (DEM), supraglacial and englacial debris distribution measured by GPR, and in situ mapping of ice exposures and sub-debris melt stream locations.

4.3.3 Bed Topography Reconstruction

In order to simulate rock glacier flow and test various rheological scenarios to reproduce observed rock glacier strain, it is necessary to use a gridded bed topography map as a geometric boundary condition impacts the ice thickness value and the driving stress. Ground-penetrating radar (GPR) measurements provide precise measurements of rock glacier thickness are sporadically available for our target sites (Meng et al., 2023b), but not on a regular grid that is sufficient to directly assemble a bed map. To combat this limitation, we test three methods for generating a gridded rock glacier bed topography map that can be used to run finite element flow simulations. These methods use various combinations of photogrammetrically derived topography and velocity measurements (Meng et al., 2023a) with GPR-based rock glacier thickness measurements (Meng et al., 2023b).

The first method we test directly uses the field-derived surface velocities in concert with the GPR-derived thickness and compositional information. We base this technique on the mass-conservation approach described by Mcnabb et al. (2012). The second method we use combines surface topography with GPR thickness measurements to invert for a bed topography grid (Langhammer et al., 2019). The final method is a Glen's Flow Law approximation with a modification for the inclusion of the debris density and thickness (Konrad et al., 1999). We compare all three of these gridded bed maps with the surface-coupled GPR observations and discuss the advantages and limitations.

4.3.4 Rheological Analysis

To test the dependence of rock glacier rheology on driving stress and ice fraction we compare our measured velocity fields with an analytical cross-flow velocity profile

for five examples at Galena Creek. The objective of the cross-flow velocity analysis is to fit the observed transverse flow profile to an empirical relationship describing a glacier's flow characteristics as a function of two free rheological parameters: Glen's creep parameter (A) and the flow exponent (n) in order to inform the rheological input parameters to a numerical flow model. The analytical model that we use to fit the cross-flow velocity profiles is an expression for a valley glacier in the following form where α is the surface slope, τ is the yield stress for ice (100 kPa), H is the glacier thickness estimated from GPR data, and W is the half-width of each profile (Cuffey and Paterson, 2010):

$$v(x) = \frac{2A}{n+1}[\rho g \alpha - \frac{\tau}{H}]^n W^{n+1}[1 - [1 - \frac{x}{W}]^{n+1}], \tag{4.2}$$

At Galena Creek, we analyzed two profiles on flat sections of the upper debris-covered glacier (Profiles 1 & 3), two profiles on steep sections with increased driving stress (Profiles 2 & 4), and one profile on the lower rock glacier where there is a higher lithic fraction (Profile 5). Since we acquired UAV orthomosaics in 2020, 2022, and 2023, we assess the velocity fields using two image pairs with time intervals of two years or greater: 2020-2022 and 2020-2023. To quantitatively test the rheological parameters of the glacier using flow data, we calculate a simple cost function equal to the squared sum of misfits between the data and the forward model over a parameter space where $10^{-30} <= A <= 10^{-20}$ and $1 <= n <= 5$. The model parameters with the minimum cost relative to the observations are considered to be the best fit.

4.4 Results & Discussion

4.4.1 Strain-Induced Debris Modifications

Note: To avoid confusion between the glaciological and mechanical uses of the term "longitudinal", we will use the term "longitudinal" to refer to lengthwise strain, and

we use the terms flow-perpendicular and flow-parallel to describe direction relative to each glacier's orientation.

The maximum strain rate magnitudes at Galena Creek are on the order of $10^{-2}a^{-1}$, which is an order of magnitude greater than the strain rates reported for rock glaciers with smaller velocity gradients (Kääb and Vollmer, 2000; Leonard et al., 2005). The strain rate tensor components at Galena Creek show a strong correlation with surface morphology and debris thickness at Galena Creek. For example, $\dot{\epsilon}_{xx}$, which is the flow-perpendicular longitudinal strain rate for Galena Creek, exhibits an evident association with observed ice exposures and sub-debris melt streams, where a compressional signal follows the documented exposure and stream waypoints along the length of the upper debris-covered glacier. This is interpreted to result from an incision an subsidence sequence, where a melt stream incises a localized channel in the ice. When the debris slumps inwards to fill this new channel, it appears as a horizontal compression signal in the strain rate map. These linear features are consistent with observed melt channels, thermokarst ice exposures, and regions of enhanced surface elevation decrease (Meng et al., 2023a), suggesting that flow-perpendicular longitudinal strain rate maps can assist in monitoring areas of increased localized melt.

The $\dot{\epsilon}_{yy}$ map illustrates a strong correlation between flow-parallel longitudinal strain rate and flow-parallel topographic curvature (Fig. 4.2b), in accordance with the correlation between surface velocity and slope. Convex-up topography is associated with extensional strain, and concave-up topography is associated with compressional strain. Furthermore, GPR data indicates a relationship between debris thickness variability and glacier surface deformation. The supraglacial debris in the cirque of Galena is approximately 1.0 $\pm$ 0.1 m thick, but as it flows over the convex-up cirque outlet, the surface extends and stretches the debris to approximately 0.75 $\pm$ 0.05 m thick, effectively decreasing the debris thickness and the debris thickness variability due to the re-extension of previously existing compressional ridges. This

decrease in debris thickness reduces the ice's thermal stability and increases surface melt, which is consistent with the observation of persistent ice exposures in this location.

After flowing through the extensional region with increased velocity, the topographic curvature transitions to convex-up, which leads to compressional buckling. The GPR data reveals this buckling, along with the associated increase in debris thickness to 1.2 $\pm$ 0.2 m, directly at the location where the glacier transition to a compressional regime. These compressional ridges persist along the subsequent section of the glacier until the surface is modified by another transition to extension. This compressional mechanism is also apparent in the uppermost cirque, where there is a compressional signal in $\dot{\epsilon}_{xx}$ associated with a set of flow-perpendicular ridges in between the two linear surface melt pathways.

At Sulphur Creek, the upper debris-covered glacier does not exhibit periodic ridges, and its flow velocity does not appear to be directed down valley, indicating an ongoing destabilization event (Meng et al., 2023a). Mapping the strain rates and ice exposure locations here is consistent with the results of Galena Creek: ice exposure locations are strongly correlated with flow-perpendicular compression (Figure 4.4, likely due to localized incision by surface melt followed by subsidence and inward collapse. This reinforces the hypothesis that strain maps can be used to monitor the locations of sub-debris melt creeks and their effects on glacier thinning. Additionally, the toe of Sulphur Creek exhibits strong flow-parallel extension. This observation, along with the observation of frequent mass wasting off of the rock glacier toe, suggests possible destabilization and acceleration of the lower rock glacier. The rest of the rock glacier does not exhibit strong strain signals, but several ridges exist on the lower rock glacier below a concave-up topographic inflection where debris thickening has observed, suggesting that these ridges were formed by compression during a previous episode of flow.

The strain map at Sourdough also revealed maximum strain rates on the or-

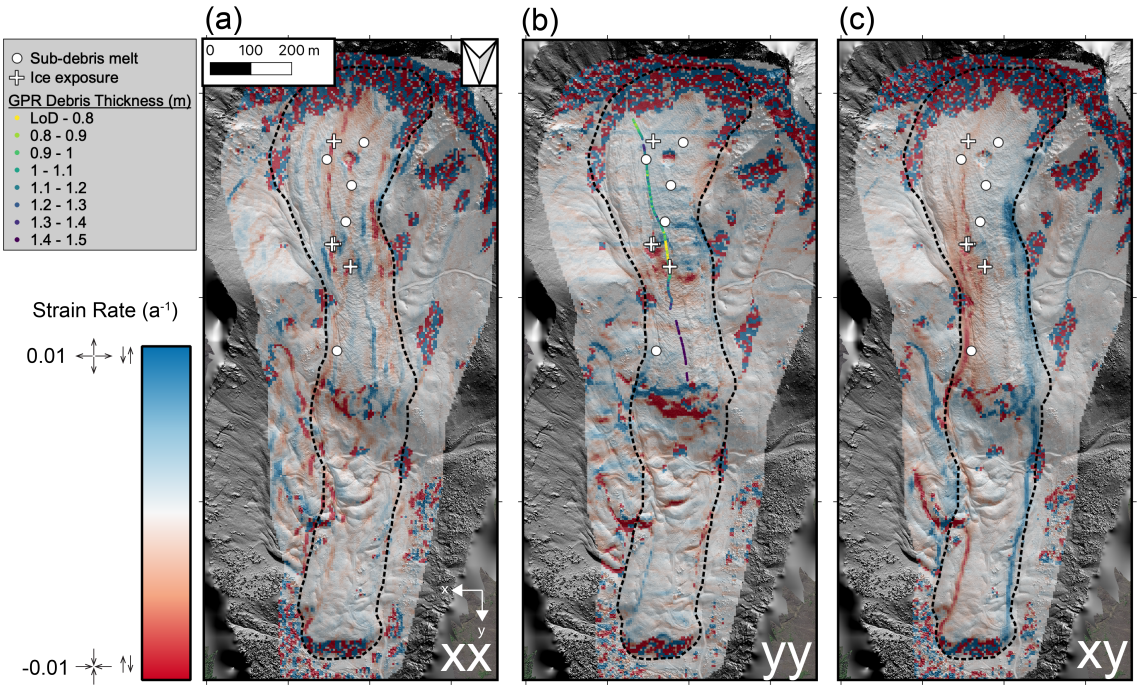

Figure 4.2: Galena Creek strain maps showing the correlation between flow-perpendicular compression and sub-debris melt along with the correlation between flow-parallel compression/extension and debris thickness and the presence of compressional buckle folding.

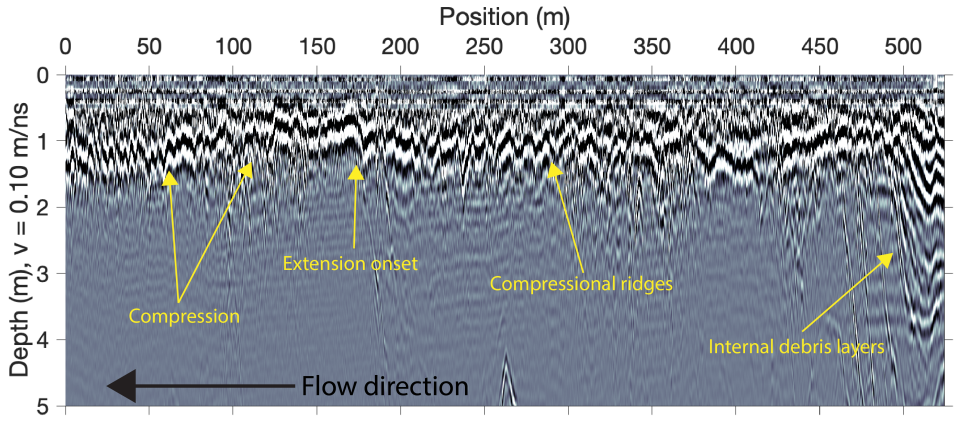

Figure 4.3: Radargram showing effects of extension and compression on the debris layer thickness and thickness variability at Galena Creek.

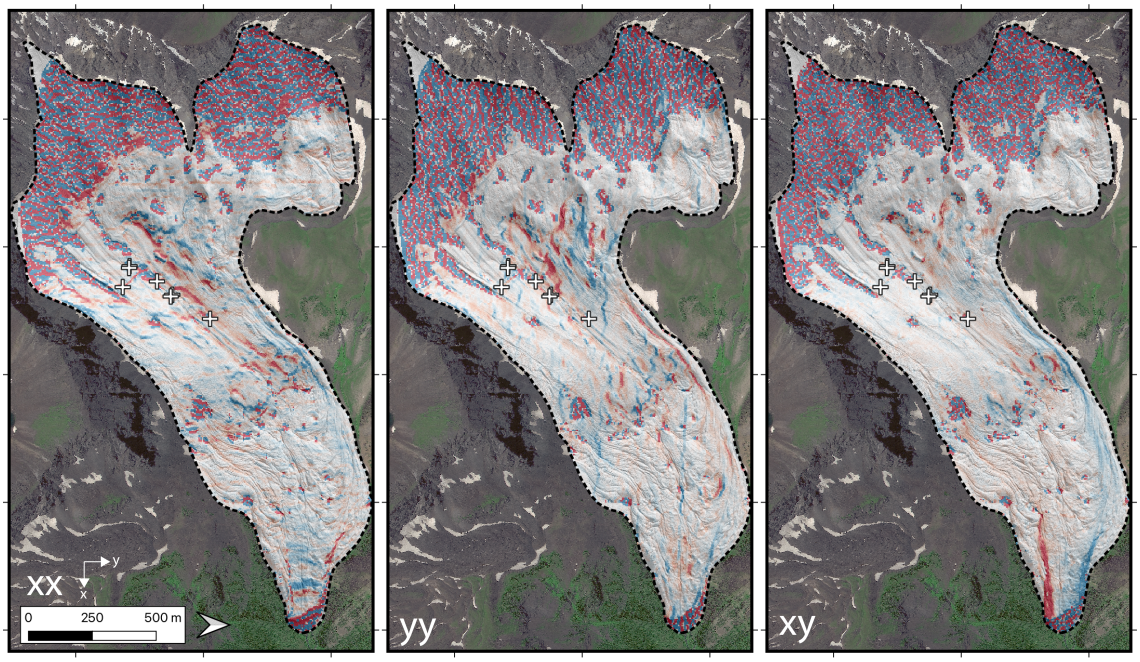

Figure 4.4: Sulphur Creek strain maps; symbology is the same as for Galena Creek.

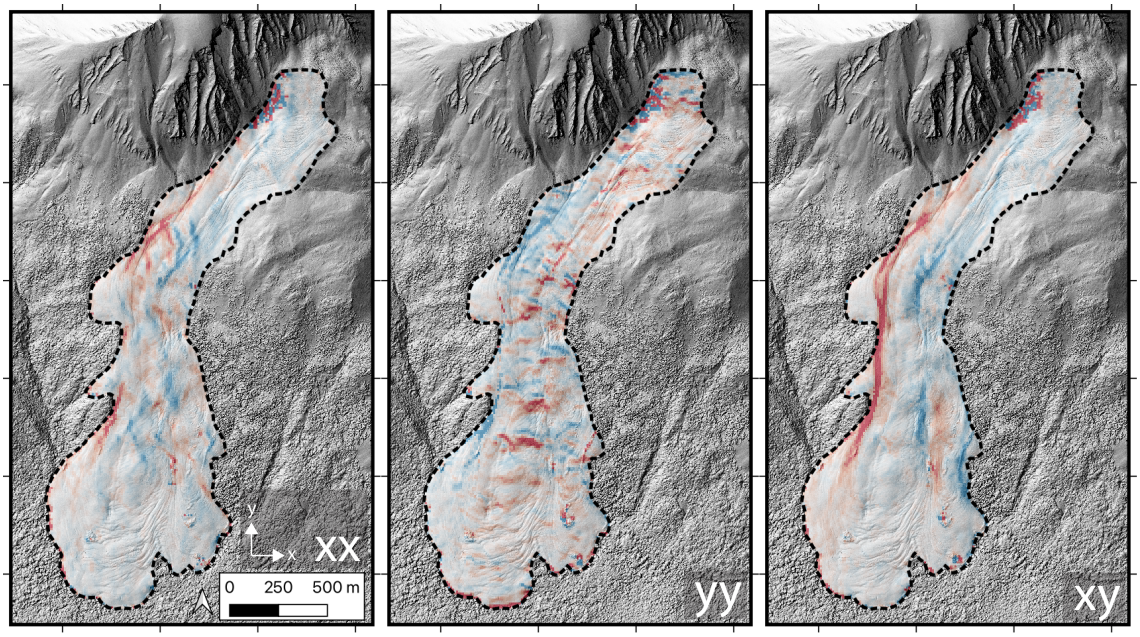

Figure 4.5: Sourdough strain maps; symbology is the same as for previous strain maps.

der of 0.01 a^{-1} with several regions of flow-parallel extension and compression in accordance with the slope curvature (Figure 4.5). We argue that this is the dominant mechanism of periodic ridge formation on Sourdough due to the abundance of compressional zones and the lack of GPR detections of internal layers that crop out at the surface. This suggests the complex topography and multiple exposures to strain and melt water infiltration through its flow history, the ice and rock were homogenized and thus any internal debris layers that may have preserved signatures of oscillating ice accumulation were erased. In addition to the recurring flow-parallel zones of extension and compression, we observe a complex signal of compression and shear strain where the flow changes direction from southwest to due south. This suggests further internal deformation at this location, along with localized surface uplift.

McCarthy Creek displays significantly slower velocities and smaller velocity gra-

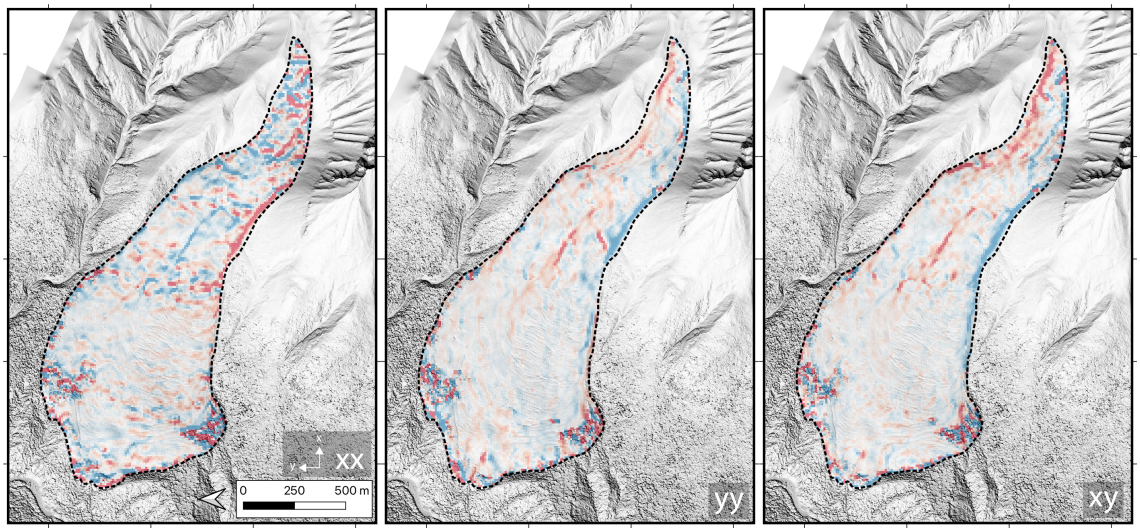

Figure 4.6: McCarthy Creek strain maps; color stretch is half that of previous rock glacier strain maps.

dients than its neighbor, Sourdough. As a result, its maximum strain rate is about half that of the other rock glacier field sites. The upper rock glacier exhibits clear shear margins (Figure 4.6), supporting the hypothesis that these strain maps are useful for mapping the flow margins of rock glaciers. Moving down the rock glacier, the surface experiences a zone of flow-parallel compression, below which ridges form. Below this section, the shear margins become more diffuse, while the ridges appear to advect downglacier. Therefore we interpret all of the ridges on McCarthy Creek to be compressional in nature.

4.4.2 Surface Ridges of Climatic Origin

The shaded relief map and GPR data in upper Galena Creek provide evidence of internal debris layers outcropping as arcuate surface ridges (Figures 4.7, 4.8). These combined datasets document observable characteristics that may be used as criteria for classifying ridges as “compressional” or “climatic” on other debris-

covered glacier systems. We observe climatic ridges extending into the subsurface at two locations of Galena Creek. The first location is below a large granitic intrusion in the andesite of the cirque's western headwall, and the second location occurs at the intersection of a debris cone, an ice-cored moraine, and the eastern shear margin of the debris-covered glacier. The climatic ridges are typically broader with a greater yet more irregular spacing in comparison with the compressional ridges. This is because the ridge spacing is dictated by ice accumulation variations and flow speed rather than the mechanical viscosity ratio that controls compressional buckling wavelengths. Furthermore, we observe that the climatic ridges display evidence of differential deformation, a nested spoon geometry, and debris layer emergence due to ice flow and ablation. In contrast, the appearance and disappearance of compressional ridges is directly related to the local stress regime, they are quasi-linearly oriented perpendicular to flow, and their wave number and amplitude both increase with magnitude of compression.

Under the assumption that internal debris layers represent warm periods between ice accumulation episodes, we estimate the frequency of climate oscillations recorded in the Galena Creek ridges/internal layers using their outcrop spacing relative to the current surface velocity field (Figure 4.7).

Below the western set of ridges, the surface slope and velocity both increase, putting the glacier into extension and thinning the surface debris as described in the previous section. This thinning of debris leads to increased melt and surface lowering. The surface-relative emergence velocity of an englacial particle is $v_e = w_s + u_s tan(\alpha)$, where w_s is the surface elevation change rate, u_s is the horizontal velocity, and α is the surface slope (Cuffey and Paterson, 2010). Increases to all of these parameters within the extensional section of the rock glacier should lead to a significant increase in debris emergence velocity, and this is consistent with the observation of an increased concentration of very large boulders of granitic provenance in this section. We argue that most of these boulders were previously

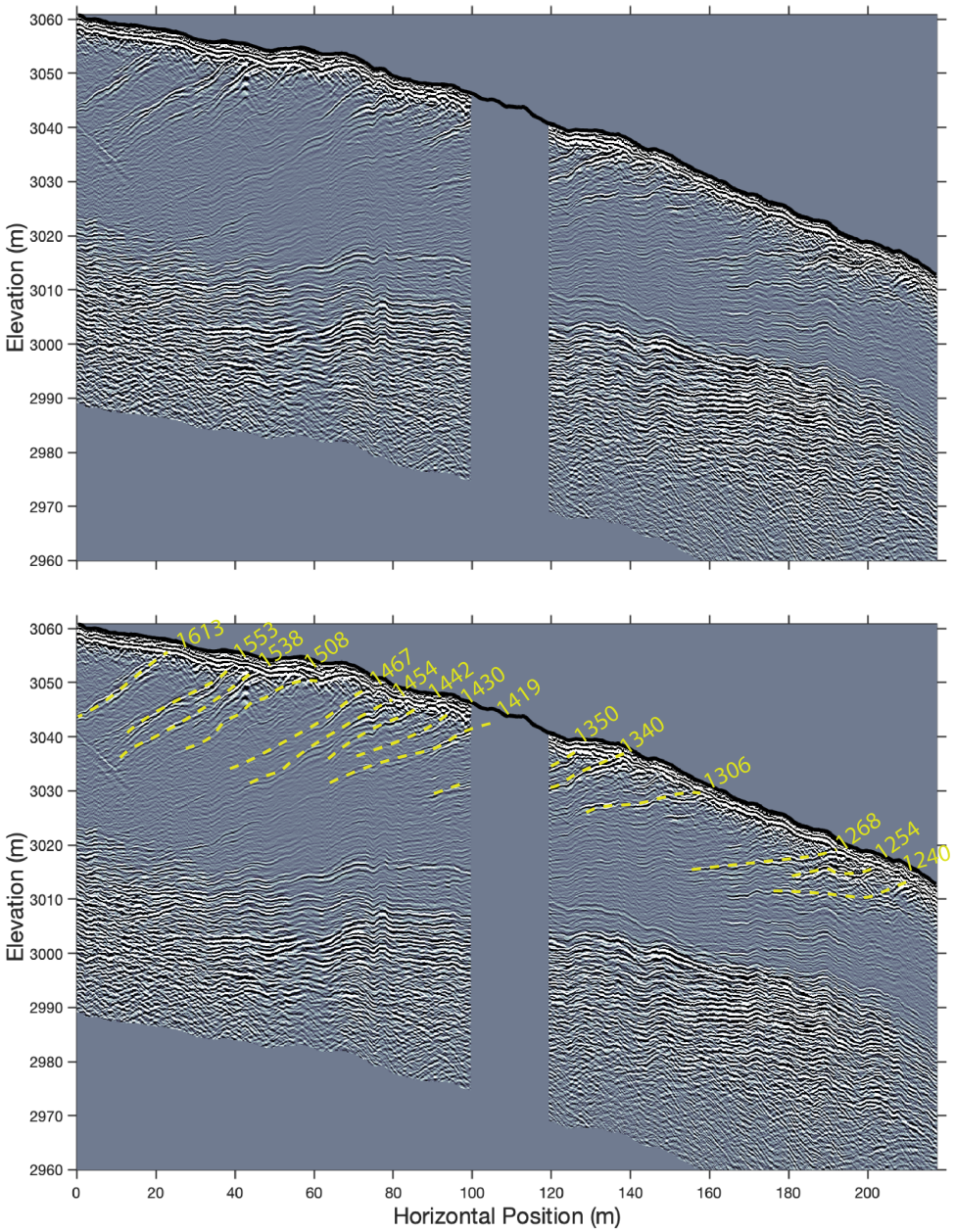

Figure 4.7: Radargram at Galena Creek, Wyoming, showing uninterpreted internal reflectors (top) along with estimated kinematic ages of each debris surface converted to the approximate year (A.D.) of debris deposition during the Little Ice Age (bottom).

buried within the glacier similarly to the internal bands that currently exist beneath the granitic intrusion in the cirque. However, as these layers encountered extension and increased surface melt, rapid debris emergence and mechanical sorting of fines led to this high boulder density in the middle of the glacier. This hypothesis is also consistent with the lack of observed outcropping internal layers downstream from the zone of extension and emergence, though GPR detects possible englacial interfaces related to separate Holocene glacial advances that deposited a series of lateral moraines (Ackert, 1998).

There is not conclusive evidence of outcropping internal layers at nearby Sulphur Creek, nor is there such evidence at either of the Alaskan sites. While added GPR surveys could detect more of these layers, their scarcity suggests that they must form under specific conditions and that they can be modified and erased by glacial deformation. For example, Galena Creek and Sulphur Creek experience the same regional climate, but Galena Creek's cirque hosts climatic ridges, while none have been conclusively documented at Sulphur Creek. Furthermore, the debris layer in the uppermost cirque of Sulphur Creek is thinner than at Galena Creek, leading to rapid ice thinning and stagnation (Meng et al., 2023b,a). We argue that local valley geometry plays an important role in the potential of each individual glacier to preserve climate signals via ridges. One morphometric parameter to describe the potential of ice preservation and climate signal preservation is the ratio of the ice accumulation area to the cirque headwall perimeter (AA/HP) for different individual glaciers in a regional population. For this case, the Galena Creek accumulation area is approximately $9.07\ x\ 10^4\ m^2$ and its headwall ridge runs approximately 1.5 km. By comparison, Sulphur Creek's accumulation area is approximately $4.80\ x\ 10^5\ m^2$ with a headwall perimeter of 2.5 km. As a result, Sulphur Creek's AA/HP ratio is more than three times greater than that of Galena Creek, implying that under the assumption of constant erosion rates, Sulphur Creek would require a headwall over three times taller than Galena Creek in order to bury its accumulation area under a

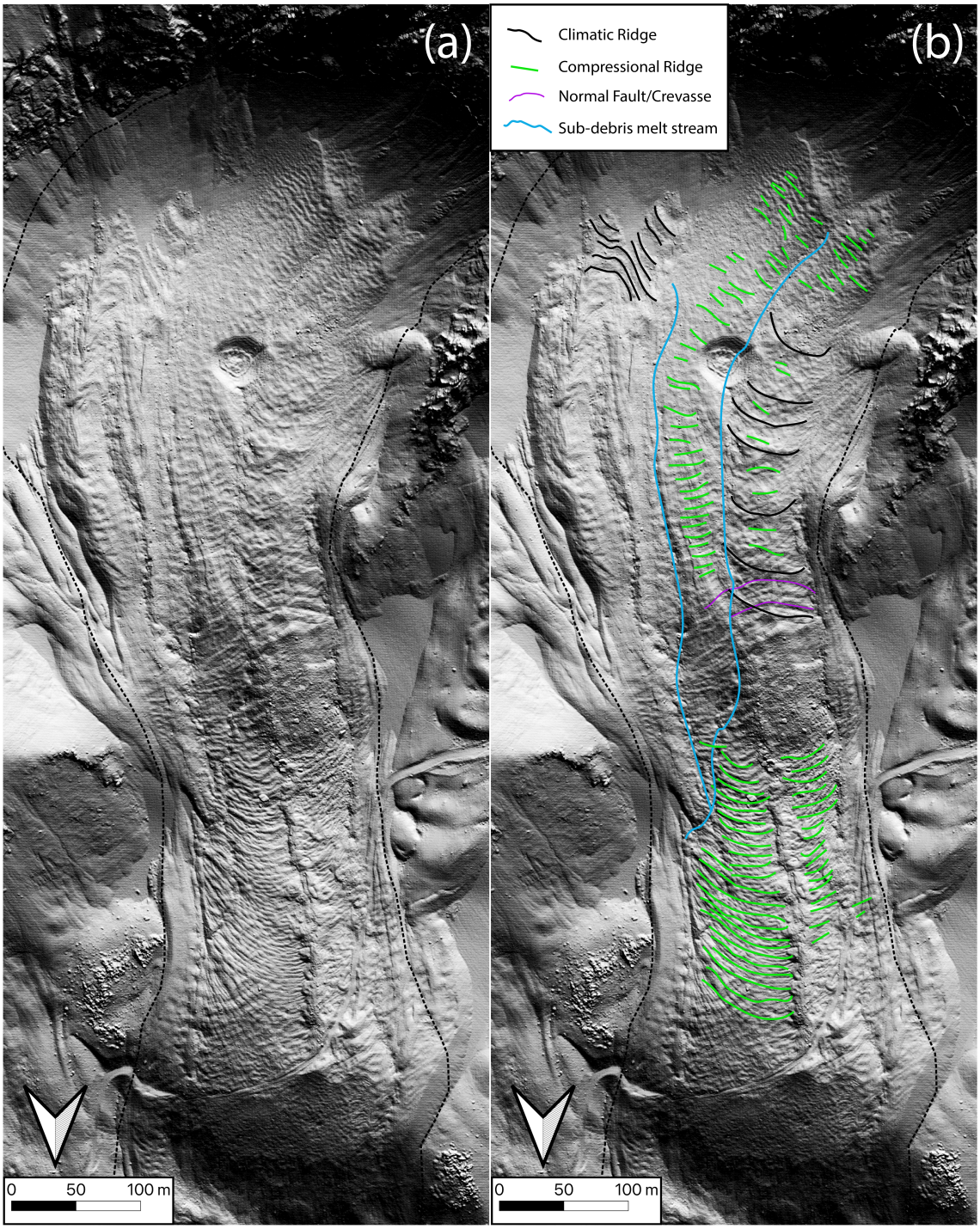

Figure 4.8: Galena Creek hillshade (a) with ridge interpretation (b).

debris layer of equivalent thickness. However, both headwalls rise between 150 and 200 m above their accumulation areas, providing an explanation for the relatively thin supraglacial debris, the lack of internal debris layers, and the rapid surface melt at upper Sulphur Creek compared with Galena Creek.

Another hypothesis for localized variability in rock glacier evolution is the topographic effects on incoming annual solar radiation, which has a direct effect on glacier energy balance and subsurface thermal state. By estimating the fraction of solar radiation that is obscured by local topography throughout the year, we find that Galena Creek receives less solar radiation than neighboring Sulphur Creek (Figure 4.9), which is consistent with the observation that ice is more readily preserved at Galena Creek than Sulphur Creek. Similarly, McCarthy Creek receives approximately 10% less solar radiation than Sourdough, which could explain the drastic difference in maximum flow velocity due to ice's temperature-dependent viscosity.

4.4.3 Gridded Bed Topography

The three methods for producing a gridded bed map showed similarities and differences in the derived thickness distribution (Figure 4.10). All three of the bed maps agreed with the flow-parallel trend where the thickness is the greatest in the cirque, then it decreases as it flows over the upper steep section of the rock glacier before thickening again as the glacier surface flattens out and experiences compression. All of these maps are generally consistent with the expected U-shaped trough that is common for alpine valley glaciers. The mass conservation method is the most limited in terms of spatial extent because it requires the use of a flux gate within the flow field of the rock glacier, and the continuity of the flow lines depends on a noise-free vector field, as an errant displacement vector will lead to a non-physical flow line. The glacier thickness inversion estimate uses a natural neighbor interpolation of existing GPR data alongside a photogrammetrically derived elevation model to generate a joint inversion using typical Glen's flow parameters. This inversion

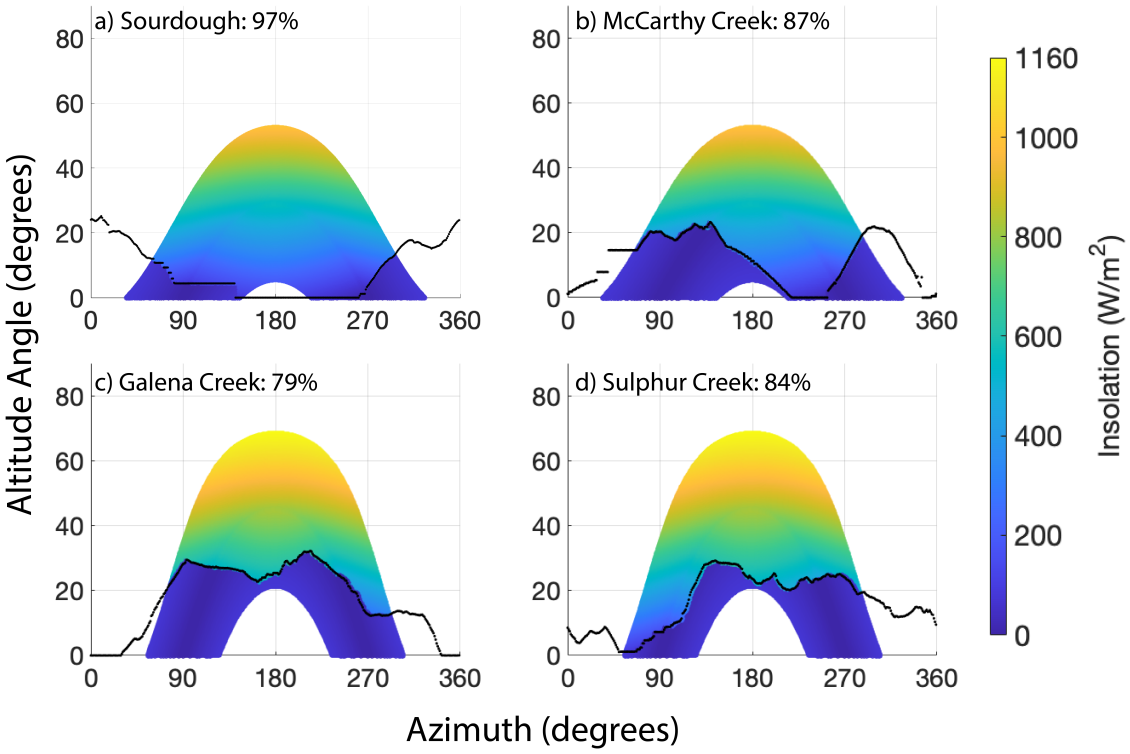

Figure 4.9: Estimated fraction of solar radiation that reaches each rock glacier surface relative to a flat surface at the same latitude. The black lines indicate the horizon as viewed from the trunk of each rock glacier; direct solar radiation is removed when the solar altitude angle is below the horizon.

produces a smooth map of the glacier thickness, although regions outside of the GPR interpolation appear to be either thicker that expected (such as the eastern portion of the cirque where there are sequential moraines with no observed flow) or thinner than expected (such as the region in the middle of the glacier that appears to be much thinner than its surroundings with no evidence in the surface velocity data). The third method uses Glen's flow law using the photogrammetric velocity data without any GPR input, but it incorporates the supraglacial debris layer to more accurately represent the bulk density, which affects the driving stress. This debris-modified Glen's flow law generates a map that is rough, but the overall trends are consistent with the existing thickness measurements. Future efforts may consider combining these methods to create a self-consistent bed map that incorporates all of the geophysical data available.

4.4.4 Rheological Analysis

The flow-perpendicular velocity analysis did not reveal conclusive quantitative trends in the Glen creep parameter A or flow exponent n at Galena Creek; both of these parameters were consistently best fit near the values expected for ice ($A \sim 10^{-24}$ & $n \sim 3$) with no relationship to slope or ice fraction. However, there is a distinct qualitative relationship apparent in the profiles (Figure 4.11) that may be further investigated by considering the assumptions governing the quantitative expressions representing rock glacier flow that are used for this type of cost function analysis. These assumptions may include the vertical velocity distribution and the state of the basal interface where plastic yield is occurring (Joughin et al., 2004). Profiles 1 and 3, which were the two profiles taken from the flat section of the upper debris-covered glacier, show the closest qualitative fit to the model, closely replicating its shape. This is consistent with the fact that these profiles most closely fit the assumptions of the analytical model: an ice stream with a flat surface and nearly pure ice.

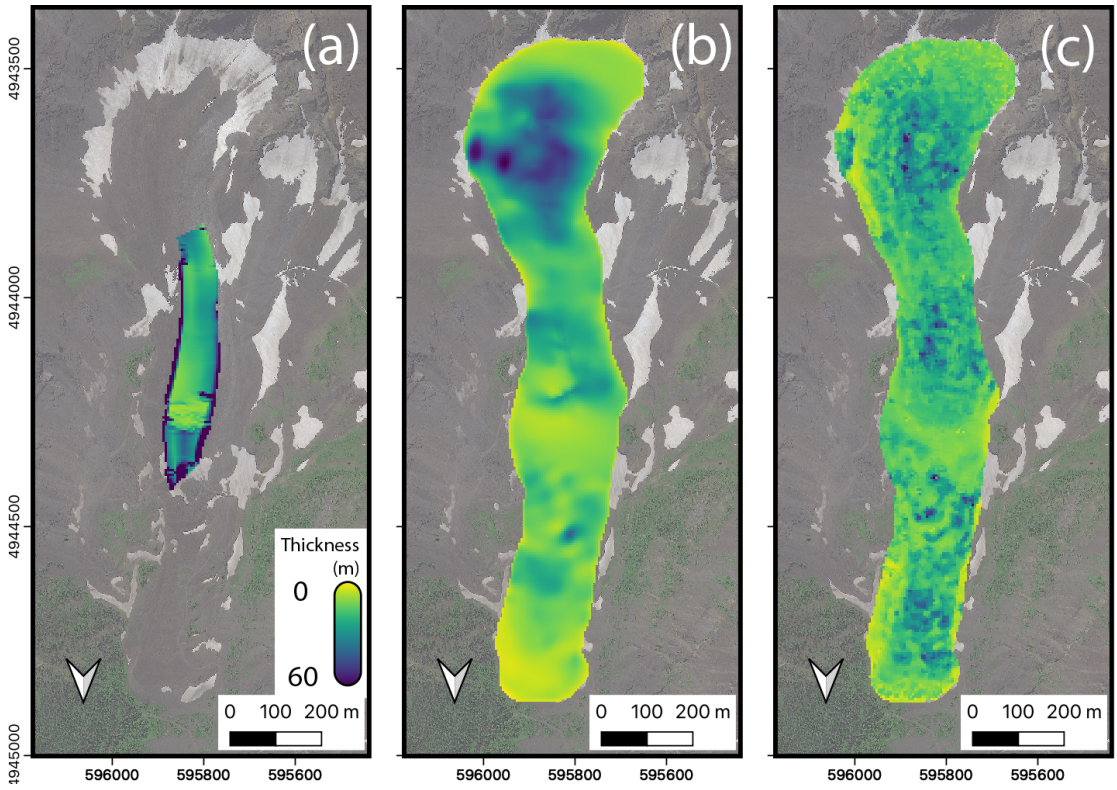

Figure 4.10: Gridded bed topography products for Galena Creek, WY: (a) mass conservation method (Mcnabb et al., 2012), (b) glacier thickness inversion (Langhammer et al., 2019), and (c) debris-modified Glen's flow law (Konrad et al., 1999).

Profiles 2 and 4 were taken from steeper sections of the rock glaciers, but still exhibit high levels of ice purity. These two profiles show similar deviations from the model: they have a relatively gentle flow-perpendicular velocity gradient and a narrow peak. The steeper surface (Profile 4) has the narrowest peak. This is consistent with the hypothesis that the rheology of the ice is stress-dependent since steeper surfaces will generally have greater driving stresses. Finally, Profile 5 was taken from the lower rock glacier, where the surface is flat but there is a much higher internal lithic component. This profile displays the opposite trend in relation to the steep sections: it has a sharp gradient at the margins with a wide peak velocity, suggesting plug flow of this lower rock glacier. Since the surface is flat but the lithic content is significantly higher than the upper debris-covered glacier, we conclude that the elevated lithic components acts to stiffen the rock glacier rheology, effectively decreasing the creep parameter or increasing the flow exponent. The qualitative pattern in the cross-flow velocity profiles is observed for both the 2020-2022 and the 2020-2023 time intervals.

4.4.5 Conclusion

Out of our four rock glacier field sites, only one of them (Galena Creek, Wyoming) displays conclusive geophysical evidence of internal debris layers outcropping as climatic ridges. Strain maps of all four glaciers suggest that compressional ridges are the dominant mechanism of ridge formation on rock glaciers, as the topographic setting where a rock glacier flows from a headwall onto a more gently sloping surface is strongly conducive to compression and subsequent thickening and buckle folding of debris. We also found that extensional strain is correlated with debris thinning and associated melt enhancement, leading to higher rates of surface subsidence and ice exposure incidence. Our method of generating strain maps with remote sensing data may also be used to map sub-debris melt streams where in situ observation is difficult.

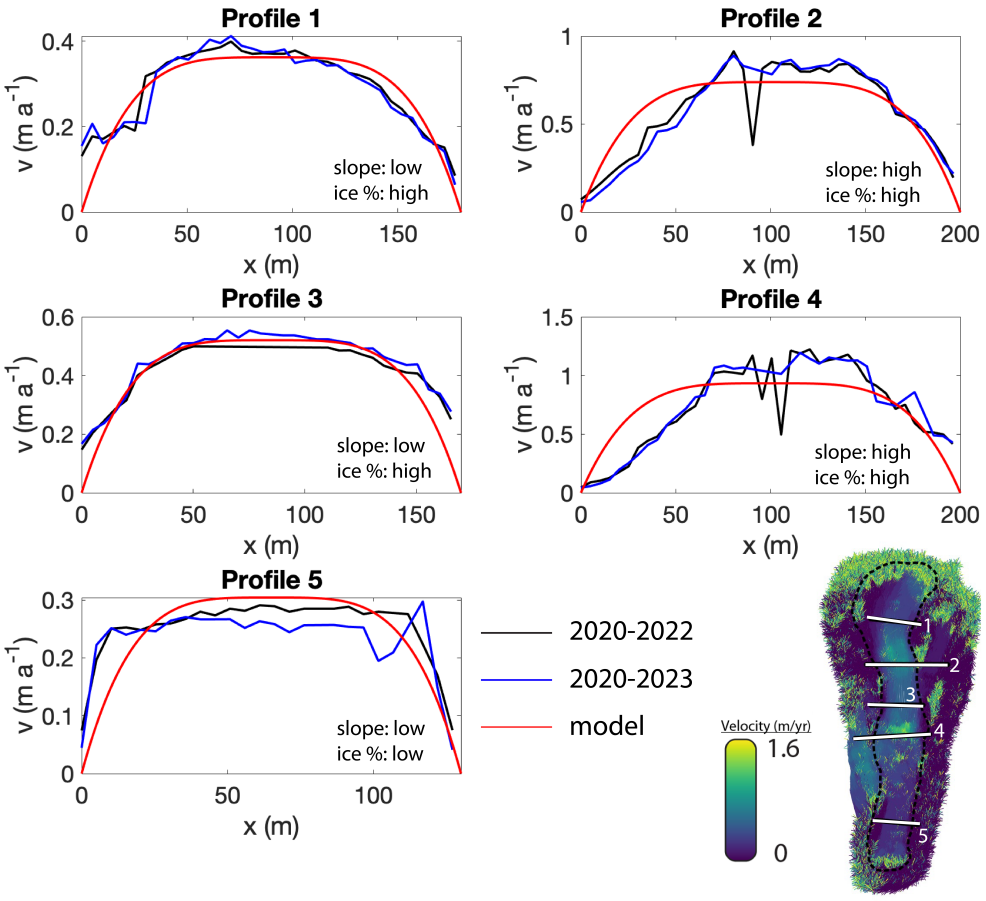

Figure 4.11: Cross-flow surface velocity analysis for Galena Creek, Wyoming. Plots show the surface velocity data measured with the 2020-2022 orthomosaic pair (black) and the 2020-2023 orthomosaic pair (blue) compared with an analytical cross-flow velocity model (red; Cuffey and Paterson (2010)).

To further estimate the total ice volume and the rheology of rock glaciers, we test three methods of generating gridded bed topography maps and we also evaluate cross-flow velocity profiles in relation to an analytical ice flow model. We find that each bed topography method has advantages and drawbacks, with the debris-modified Glen's flow law being the most robust method. Despite the lack of clear quantitative trends in the best-fit rheological parameters for the cross-flow velocity profiles, we observe qualitative trends that suggest relationships between rock glacier driving stress, lithic content, and rheology. These findings can directly inform numerical modeling efforts to simulate the dynamics of rock glacier formation and evolution.

CHAPTER 5

Implications for Planetary Rock Glacier Inventories, Stratigraphic Correlation, and Climate History

5.1 Abstract

Rock glaciers with ridges are common in the midlatitudes of Mars. We propose a stratigraphic sequence for these midlatitude ice by considering ridges as climatic or compressional in origin. This sequence includes a unit of recent flow features, a midlatitude layered deposit, and an early glacial deposit that has a higher degree of degradation. We map these units in four regions in the midlatitudes of Mars and consider their absolute and relative ages in comparison with Mars' polar ice deposits. This interpretation suggests the earliest Amazonian ice accumulation occurred in the southwestern midlatitudes, and the accumulation center migrated throughout the Amazonian period to the northeastern midlatitudes. Further mapping of these units in the global dataset will reveal martian climate signals in unprecedented detail while benefiting both terrestrial and planetary glaciology communities.

5.2 Observations of Ridges on Martian Rock Glaciers

Innovations in measurement resolution and data volume capacity have led to significant focus on the martian midlatitudes as hosts to glacial remnants of past climatic cycles. Both of its poles presently host ice with indications of climate oscillations recorded by their dusty stratigraphy (Smith et al., 2016; Lalich and Holt, 2017; Nerozzi and Holt, 2018; Whitten and Campbell, 2018; Nerozzi and Holt, 2019; Nerozzi et al., 2022). Massive subsurface ice deposits approaching latitudes as low

as 30 degrees have been detected through morphological mapping and radar sounding. There are indicators of past tropical glaciation, with recent results suggesting that the Medusae Fossae formation consists of significant water ice volumes (Watters et al., 2024). Moraines and rock glacier-like deposits suggest previously flowing cold-based glaciers on the Tharsis Montes (Parsons et al., 2020). Debris-covered glaciers and buried ice sheets likely accumulated during periods of high orbital obliquity when water is transported between the poles and equatorial latitudes (Forget et al., 2006; Schorghofer, 2008).

A complicating factor in mapping the surface stratigraphy of the midlatitude glacial deposits on Mars is that a significant fraction of this region's surface area is draped by a fine-grained latitude dependent mantling deposit (Baker and Head, 2015). This material mutes or entirely obscures the arcuate ridges that may be diagnostic of climatic or compressional surface processes. Due to surface modification from the emplacement of this mantle material along with deformation due to glacier flow or ice removal, absolute age dating of martian rock glaciers via crater size/frequency distributions has an extra layer of complexity compared to less weathered surfaces. Broadly, stratigraphic cross-cutting relationships combined with crater mapping yield average ages in the hundreds of millions of years for the homogenized population of midlatitude glacial deposits (Fassett et al., 2014). Detailed mapping of crater degradation sequences on midlatitude glacier surfaces in Deuteronilus Mensae showed that while the total crater retention age is in the hundreds of millions of years, the distribution of well-preserved bowl-shaped craters is consistent with an age on the order of tens of millions of years (Baker and Carter, 2019), These crater degradation observations suggest glacier flow and surface modification throughout the middle to late Amazonian, and the geographic trends in crater density and texture development suggest a slightly younger age in the northern and eastern subregions compared with the southwestern subregion. Here, the objective is to map textures on the surfaces of martian midlatitude glaciers from four separate

regions around the planet using the context gained from the terrestrial analog ridge classification results. We observe and document three major stratigraphic units in our regions of interest, which we then discuss in the context of the accumulation history of Mars' polar layered deposits and previous crater retention analyses.

For our global mapping experiment, we use the CTX global mosaic produced by the Murray Lab to evaluate the surface morphology that is not obscured by mantling deposits on debris-covered glaciers. We examined four regions that host high spatial densities of debris covered glaciers mapped by Levy et al. (2014). In the northern hemisphere, we examined Deuteronilus Mensae and Phlegra Montes. In the southern hemisphere, we examined the rim terrain of Eastern Hellas and southern Argyre basins. Across all four of these regions, we have identified surface stratigraphy that mirrors the radar stratigraphy of the northern polar layered deposits, supporting the hypothesis that periodic water exchange occurs between the poles and midlatitudes. Using our criteria from the terrestrial analog study presented in the previous chapter, we identified two sets of ridges that are likely climatic in origin, representing contacts between major glacial periods during the Amazonian, and these contacts can be traced across all four of these regions. The youngest contact occurs near the glacier headwalls, and it is characterized by a broad continuous ridge that appears unrelated to compressional mechanisms, suggesting an ablation surface that was subsequently buried by more ice accumulation. This contact often coincides with the termini of mapped glacier-like features (Souness et al., 2012). For simplicity, we classify this stratigraphic unit as "recent flow features" (RFF).

Below this major climatic ridge, there is a unit containing many closely spaced ridges. Due to their close proximity to one another and the lack of high-resolution geophysical data, these individual ridges cannot be classified as climatic or compressional, but it is likely that this middle section of the glacier contains a combination of both types of ridges, which is consistent both with climate oscillations and the strongly concave-up topography that is associated with the transition from the steep

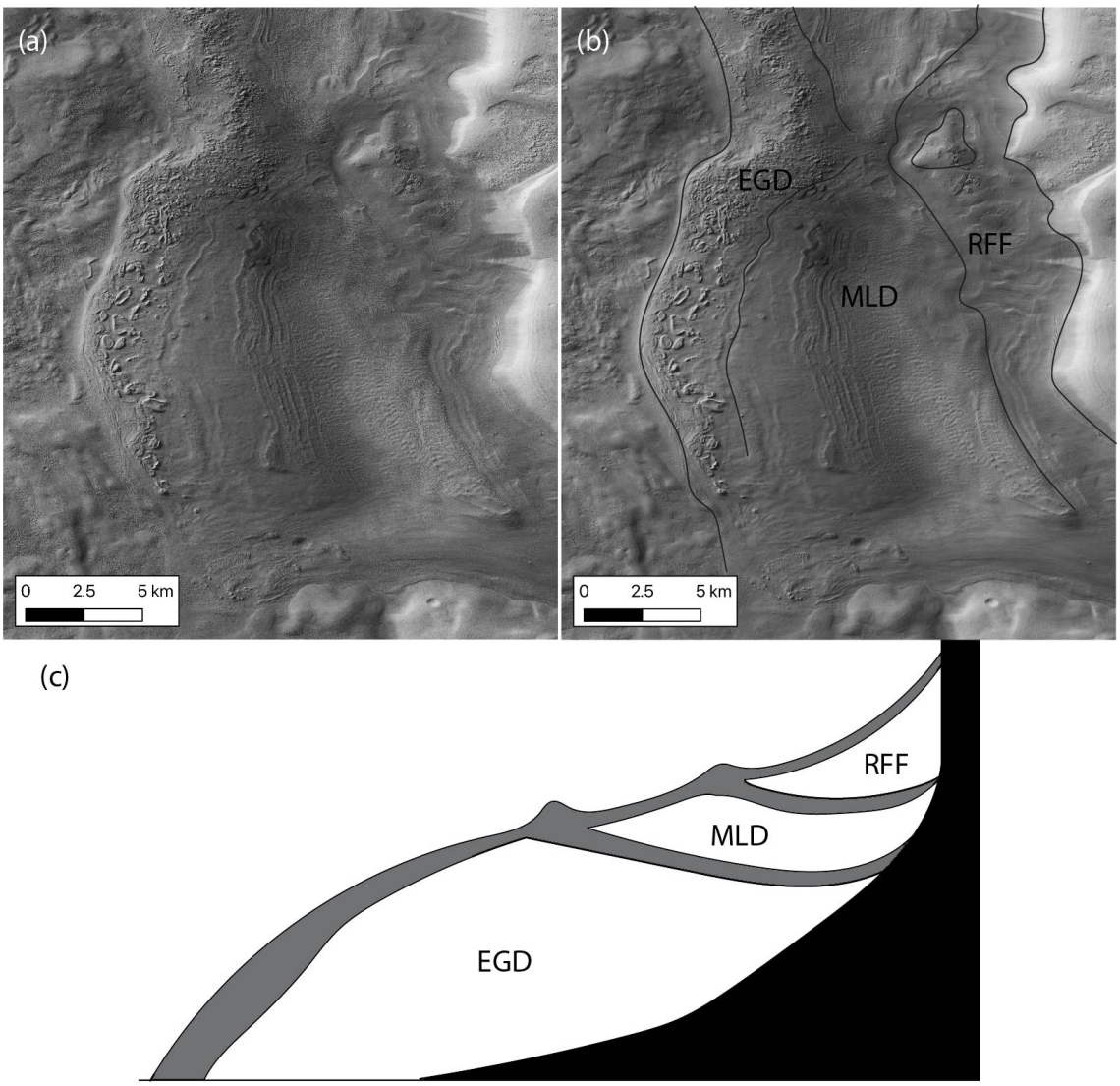

Figure 5.1: (a) Example of surface morphology and (b) contact mapping for a lobate debris apron in the Eastern Hellas region using the global CTX mosaic. North is up on the page. (c) Schematic diagram of proposed stratigraphic sequence of Mars' midlatitude glaciers. This sequence includes recent flow features (RFF) on top of the midlatitude layered deposits (MLD), both of which overly the earliest glacial deposits (EGD). This diagram is not to scale and compressional ridges may also be present on individual glaciers.

headwall where the RFF is located to the wider and more-gently sloped lobate debris aprons. We classify this unit as the "midlatitude layered deposits" (MLD) due to the abundance of relatively continuous ridges and likely minor climatic layers. It is also noted that many of these minor ridges cannot be distinguished as climatic or compressional with existing remote sensing data. Further downslope from the MLD, the surface transitions to a degraded and chaotic surface with fewer continuous ridges, indicating significant reworking and possible ice ablation since its initial emplacement. In some regions, this contact is marked by a broad climatic ridge, but it is often obscured by mantling material or sublimation features. Since this unit exists at the most distal parts of the glaciers and it has undergone the most reworking, we classify this unit as the "earliest glacial deposits" (EGD). This sequence of units is demonstrated for a glacier in Eastern Hellas in Figure 5.1.

In Deuteronilus Mensae, sufficient SHARAD density has permitted the production of a 3D radar sounding volume (Perry et al., 2023). One candidate internal reflector in a lobate debris apron has been identified in this dataset. Although further analysis is needed to entirely rule out aliasing or clutter, the intersection of this candidate reflector with the glacier surface agrees with the location of the mapped contact between the MLD and the EGD surface facies on this particular feature (Figure 5.2). As a whole, northern and eastern sites have a greater fraction of young deposits compared with the southern and western sites, and this hypothesis may be further explored by additional geographic analysis.

5.3 Stratigraphic Interpretations

By using the lengths of the glacier-like features associated with our RFF unit (Souness et al., 2012) along with the estimated maximum flow velocity of 20 mm/a on the massif headwalls (Parsons and Holt, 2016), we estimate the kinematic ages of each feature using the method from Meng et al. (2023a) (Figure 5.3). The age distribution for both the northern and southern hemisphere glacier-like features has

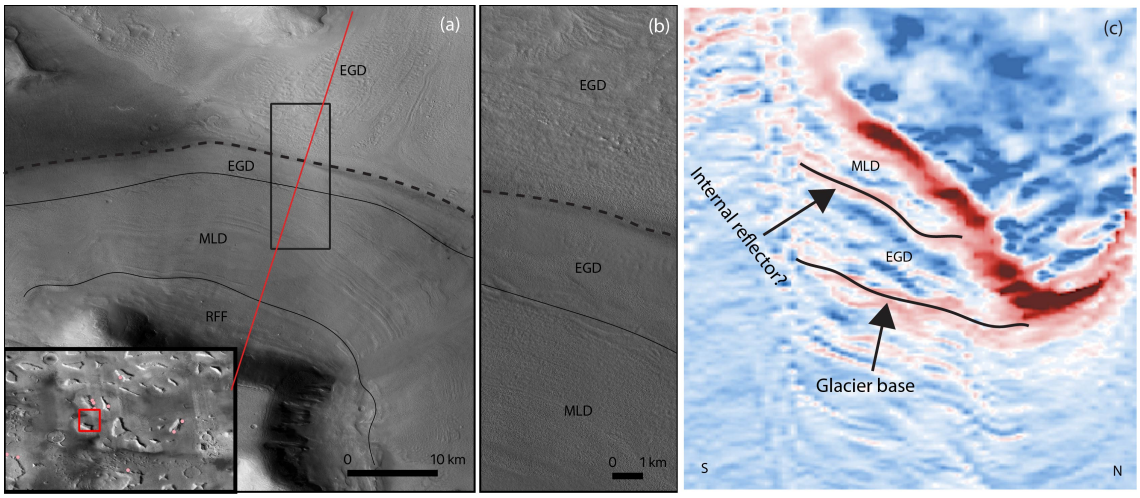

Figure 5.2: Contact mapping in Deuteronilus Mensae between the three identified stratigraphic units for the midlatitude glaciers: (a) CTX mosaic, (b) HiRISE image located at black box in (a), and (c) 3D SHARAD radargram from south to north over the same glacier (Perry et al., 2023), showing the candidate internal reflector potentially intersecting with the surface at the mapped MLD/EGD contact. For all maps shown in this chapter, north is up on the page.

a mean of a few hundred thousand years, strongly agreeing with the age of the widespread recent accumulation package of the northern ice cap mapped by Smith et al. (2016). This strong correlation suggests the need for more investigation into the ongoing and very recent migration of ice between Mars' poles and midlatitudes.

The Phlegra Montes region shows similar stratigraphic trends as Deuteronilus Mensae throughout its population of lobate debris aprons and concentric crater fill. The example shown in Figure 5.4 depicts concentric crater fill with similar stratigraphic trends as those identified in Deuteronilus Mensae. The distribution of these different units in the two northern regions we explored can further elucidate the migration of ice accumulation centers in the midlatitudes throughout the Amazonian. For example, a preliminary survey of Phlegra Montes reveals a greater amount of exposed EGD terrain compared with Deuteronilus Mensae, suggesting that northern hemisphere midlatitude ice accumulation was centered over Phlegra Montes in the early Amazonian but transitioned to Deuteronilus Mensae more recently.

The regions in the southern hemisphere display similar stratigraphic trends on their glacier surfaces, and they also exhibit spatial variability. Eastern Hellas basin has one of the highest densities of debris-covered glaciers in the southern midlatitudes, and it contains evidence of all three of the major polar stratigraphic units that we have identified. Preliminary mapping indicates similar distributions of the stratigraphic units as is observed in Phlegra Montes, suggesting that these two regions experienced ice accumulation during similar periods of the early to middle Amazonian, compared to the more recent ice accumulation in Deuteronilus Mensae.

The glacial features in Galle Crater, which is located along the edge of the larger Argyre basin, show a unique stratigraphic distribution compared to the other three regions (Figure 5.5). Here the EGD deposit appears to be disconnected from the rest of the lobate debris apron, and it consists of a layered mound that appears to have a surface that is presently eroding due to a complete absence of craters. The layering of this unit is pronounced and it resembles outcrops of the Rupes

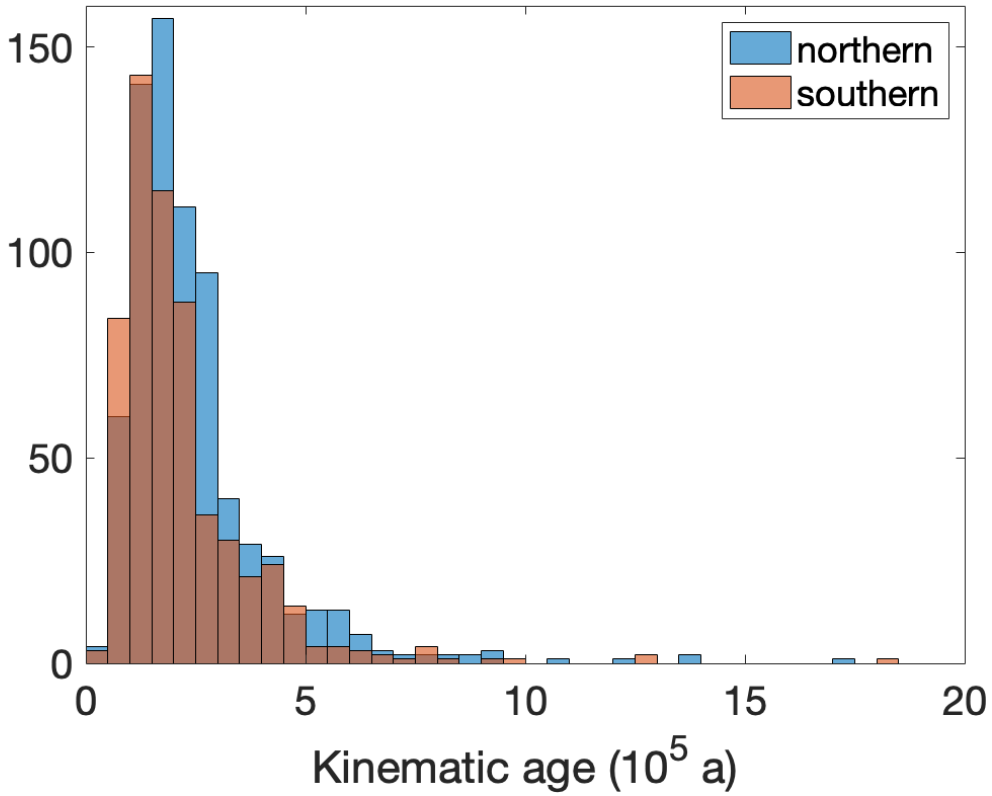

Figure 5.3: Distributions of RFF kinematic ages in each hemisphere of Mars using the landform lengths mapped by Souness et al. (2012) and the maximum flow velocities described by Parsons and Holt (2016). These flow timescales are in good agreement with the age of the recent polar ice deposits from Smith et al. (2016), suggesting a pause in midlatitude ice accumulation correlated to the onset of the most recent polar ice accumulation.

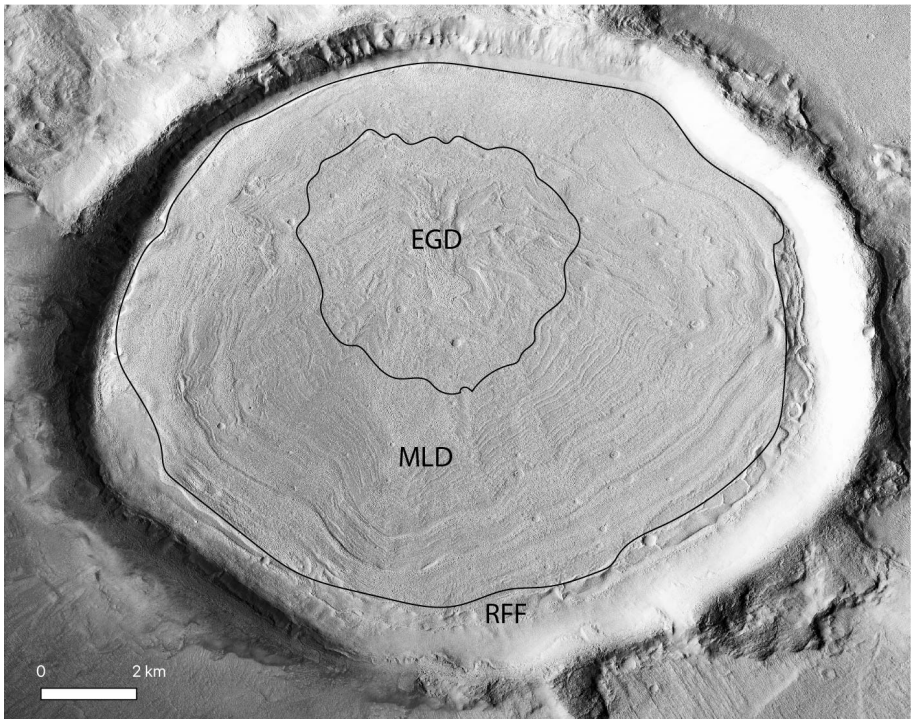

Figure 5.4: Contact mapping for a concentric crater filling glacier in Phlegra Montes. North is up on the page.

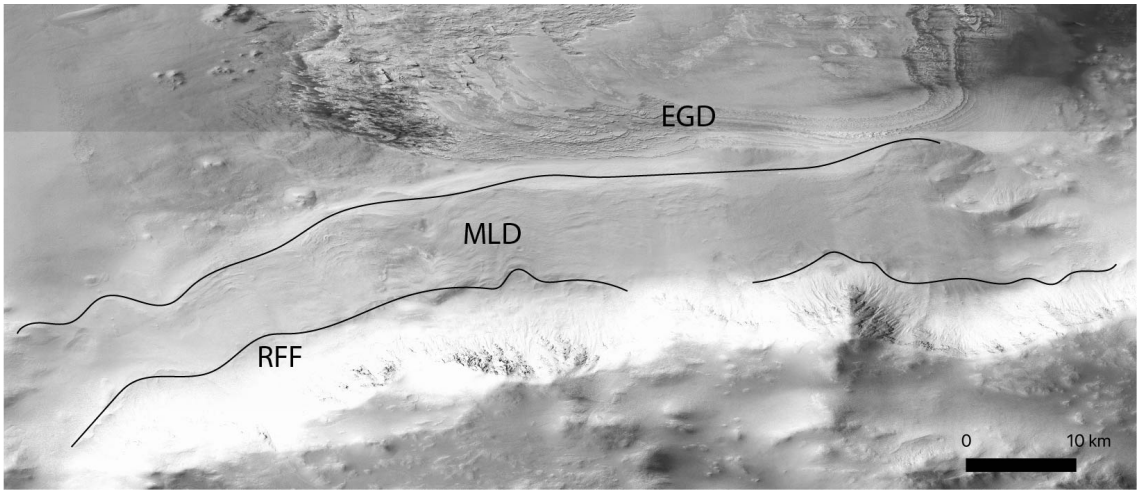

Figure 5.5: Contact mapping for a lobate debris apron complex in the Argyre/Galle crater region of Mars' southern midlatitudes. North is up on the page.

unit in the northern polar layered deposits (Nerozzi et al., 2022). The surface of the overlying lobate debris aprons display evidence of a RFF and a MLD unit, but these contacts and surface morphologies are less developed than those in the other regions we examined. This could indicate that Argyre and Galle crater were strong ice accumulation centers in the earliest Amazonian period, but they received relatively less ice accumulation during the middle and late Amazonian compared with the other regions with dense glacier populations.

Using these relative distributions of the stratigraphic units throughout each of the four regions we examined, we can reconstruct a rough ice accumulation history throughout the Amazonian. The early Amazonian period consisted of significant ice accumulation in the Argyre region, and some early Amazonian ice accumulation also occurred in Eastern Hellas and Phlegra Montes. Throughout the middle Amazonian, this ice accumulation continued in Eastern Hellas and Phlegra Montes, while the accumulation strengthened in Deuteronilus Mensae and weakened in the Argyre region. Finally, the heaviest recent ice accumulation occurred in Deuteronilus Men-

sae, consistent with the significant mantling deposits in this region, although there was widespread recent accumulation throughout each region that was investigated. The Argyre region has experienced the least recent ice accumulation, and is possibly experiencing ongoing ice removal. This interpreted sequence of ice deposition, which trends towards the early Amazonian in the southern hemisphere and the mid to late Amazonian in the northern hemisphere, is consistent with the observation that the northern polar layer deposits are younger than the southern polar layered deposits. Further detailed stratigraphic mapping combined with Amazonian climate models may corroborate this proposed sequence of martian ice migration.

The lower two units (MLD & EGD) qualitatively coincide with the polar layered deposits (PLD) and the early basal unit composed of a lower ice fraction (Nerozzi and Holt, 2018, 2019; Nerozzi et al., 2022). These observations support the hypothesis that ice is directly transferred from the poles to the midlatitudes due to orbital variability, while also being affected by broader global trends of ice emplacement and removal. However, the absolute ages estimated by crater age dating indicate that ice preservation may not occur on perfectly equivalent timescales between the poles and midlatitudes. For example, the northern and southern PLD both range in age from millions to tens of millions of years old (Byrne, 2009), while the crater distribution on the midlatitude glaciers suggests ages in the hundreds of millions of years (Fassett et al., 2014; Baker and Carter, 2019). The RFF are too small and too young to effectively date via crater mapping. While the specificity of ridge formation requirements precludes a one-to-one correlation of Amazonian glacial/interglacial periods between the poles and midlatitudes, general trends can still be inferred. For example, the preserved cryosphere in the southern hemisphere appears to be older than in the north, both in the polar layered deposit ages and the interpreted stratigraphic distribution of midlatitude deposits discussed here. Future work should continue to examine crater degradation sequences on regional populations of midlatitude glaciers with different distributions of these proposed stratigraphic units. Coupling

this geomorphic and geophysical investigation with the latest global climate models will deepen our insight into the spatiotemporal variability of ice accumulation throughout the Amazonian period.

5.4 Ongoing Applications on Earth

This work will directly inform the targeted observables driving future terrestrial rock glacier measurement and monitoring campaigns with implications for planetary analogs and mission planning. We have demonstrated a technique for measuring rock glacier composition and structure, along with the associated uncertainty, using a single bistatic GPR system with two antenna configurations. We have also shown the viability of leveraging cross-platform optical imaging to measure rock glacier flow fields and estimating their age based on kinematic constraints. While this method was successful for high-resolution optical imaging, future campaigns may choose to incorporate multidisciplinary datasets, such as InSAR, to increase the temporal resolution of rock glacier monitoring while also mitigation problems caused by clouds that can interfere with optical imaging. Finally, the combination of GPR and photogrammetric data can be used predict and confirm the origin of surface ridges as climatic or compressional. Applying all of these techniques to field sites in the rock glacier kinematics inventory will more accurately constrain the water budget contained in these alpine regions while also providing information about the climatic history of each region of interest. By studying the rock glaciers close to home with an awareness of their planetary cousins, we gain a deeper appreciation for the value they provide for us here and now, we decode their past lives while forecasting their future behavior, and we maintain our senses of curiosity and perseverance that will drive us to the depths of exploration in this solar system and onward.

REFERENCES

Ackert, R. P., jr. (1998). A Rock Glacier/Debris-Covered Glacier System at Galena Creek, Absaroka Mountains, Wyoming. *Geografiska Annaler: Series A, Physical Geography*, **80**(3–4), p. 267–276. ISSN 0435-3676, 1468-0459. doi: 10.1111/j.0435-3676.1998.00042.x.

Anderson, R. S., L. S. Anderson, W. H. Armstrong, M. W. Rossi, and S. E. Crump (2018). Glaciation of alpine valleys: The glacier – debris-covered glacier – rock glacier continuum. *Geomorphology*, **311**, p. 127–142. ISSN 0169555X. doi:10.1016/j.geomorph.2018.03.015.

Baker, D. M. and L. M. Carter (2019). Probing supraglacial debris on Mars 2: Crater morphology. *Icarus*, **319**, p. 264–280. ISSN 00191035. doi:10.1016/j.icarus.2018.09.009.

Baker, D. M. and J. W. Head (2015). Extensive Middle Amazonian mantling of debris aprons and plains in Deuteronilus Mensae, Mars: Implications for the record of mid-latitude glaciation. *Icarus*, **260**, p. 269–288. ISSN 00191035. doi: 10.1016/j.icarus.2015.06.036.

Baker, D. M., J. W. Head, and D. R. Marchant (2010). Flow patterns of lobate debris aprons and lineated valley fill north of Ismeniae Fossae, Mars: Evidence for extensive mid-latitude glaciation in the Late Amazonian. *Icarus*, **207**(1), p. 186–209. ISSN 00191035. doi:10.1016/j.icarus.2009.11.017.

Barsch, D. (1987). The problem of the ice-cored rock glacier. *In Rock Glaciers; Giardino, J.R., Shroder, J.E., Jr., Vitek, J.D., Eds.*, pp. 45–53.

Berthling, I., B. Etzelmuller, K. Isaksen, and J. L. Sollid (2000). Rock Glaciers on Prins Karls Forland. II: GPR Soundings and the Development of Internal Structures. p. 13.

Byrne, S. (2009). The Polar Deposits of Mars. *Annual Review of Earth and Planetary Sciences*, **37**(1), p. 535–560. ISSN 0084-6597, 1545-4495. doi:10.1146/annurev.earth.031208.100101.

Capps, S. R. (1910). Rock Glaciers in Alaska. *The Journal of Geology*, **18**(4), p. 359–375. ISSN 0022-1376, 1537-5269. doi:10.1086/621746.

Clark, D. H., E. J. Steig, N. Potter, A. Updike, J. Fitzpatrick, and G. M. Clark (1996). Old ice in rock glaciers may provide long-term climate records. *Eos, Transactions American Geophysical Union*, **77**(23), p. 217. ISSN 0096-3941. doi: 10.1029/96EO00149.

Clark, D. H., E. J. Steig, N. Potter, jr., and A. R. Gillespie (1998). Genetic variability of rock glaciers. *Geografiska Annaler: Series A, Physical Geography*, **80**(3–4), p. 175–182. ISSN 0435-3676, 1468-0459. doi:10.1111/j.0435-3676.1998.00035.x.

Cuffey, K. and W. S. B. Paterson (2010). *The physics of glaciers*. Butterworth-Heinemann/Elsevier, Burlington, MA, 4th ed edition. ISBN 978-0-12-369461-4.

Fassett, C. I., J. S. Levy, J. L. Dickson, and J. W. Head (2014). An extended period of episodic northern mid-latitude glaciation on Mars during the Middle to Late Amazonian: Implications for long-term obliquity history. *Geology*, **42**(9), p. 763–766. ISSN 1943-2682, 0091-7613. doi:10.1130/G35798.1.

Florentine, C., M. Skidmore, M. Speece, C. Link, and C. A. Shaw (2014). Geophysical analysis of transverse ridges and internal structure at Lone Peak Rock Glacier, Big Sky, Montana, USA. *Journal of Glaciology*, **60**(221), p. 453–462. ISSN 0022-1430, 1727-5652. doi:10.3189/2014JoG13J160.

Forget, F., R. M. Haberle, F. Montmessin, B. Levrard, and J. W. Head (2006). Formation of Glaciers on Mars by Atmospheric Precipitation at High Obliquity. *Science*, **311**(5759), p. 368–371. ISSN 0036-8075, 1095-9203. doi:10.1126/science.1120335.

Frehner, M., A. H. M. Ling, and I. Gärtner-Roer (2015). Furrow-and-Ridge Morphology on Rockglaciers Explained by Gravity-Driven Buckle Folding: A Case Study From the Murtèl Rockglacier (Switzerland): Rockglacier Furrow-and-Ridge Morphology Explained by Buckle Folding. *Permafrost and Periglacial Processes*, **26**(1), p. 57–66. ISSN 10456740. doi:10.1002/ppp.1831.

Fukui, K., T. Sone, J. A. Strelin, C. A. Torielli, J. Mori, and Y. Fujii (2008). Dynamics and GPR stratigraphy of a polar rock glacier on James Ross Island, Antarctic Peninsula. *Journal of Glaciology*, **54**(186), p. 445–451. ISSN 0022-1430, 1727-5652. doi:10.3189/002214308785836940.

Head, J. W., D. R. Marchant, J. L. Dickson, A. M. Kress, and D. M. Baker (2010). Northern mid-latitude glaciation in the Late Amazonian period of Mars: Criteria for the recognition of debris-covered glacier and valley glacier landsystem deposits.

Earth and Planetary Science Letters, **294**(3–4), p. 306–320. ISSN 0012821X. doi: 10.1016/j.epsl.2009.06.041.

Head, J. W., J. F. Mustard, M. A. Kreslavsky, R. E. Milliken, and D. R. Marchant (2003). Recent ice ages on Mars. *Nature*, **426**(6968), p. 797–802. ISSN 0028-0836, 1476-4687. doi:10.1038/nature02114.

Heid, T. and A. Kääb (2012). Evaluation of existing image matching methods for deriving glacier surface displacements globally from optical satellite imagery. *Remote Sensing of Environment*, **118**, p. 339–355. ISSN 00344257. doi:10.1016/j.rse.2011.11.024.

Holt, J. W., A. Safaeinili, J. J. Plaut, J. W. Head, R. J. Phillips, R. Seu, S. D. Kempf, P. Choudhary, D. A. Young, N. E. Putzig, D. Biccari, and Y. Gim (2008). Radar Sounding Evidence for Buried Glaciers in the Southern Mid-Latitudes of Mars. *Science*, **322**(5905), p. 1235–1238. ISSN 0036-8075, 1095-9203. doi:10.1126/science.1164246.

Joughin, I., D. R. MacAyeal, and S. Tulaczyk (2004). Basal shear stress of the Ross ice streams from control method inversions: SHEAR STRESS OF THE ROSS ICE STREAMS. *Journal of Geophysical Research: Solid Earth*, **109**(B9), pp. n/a–n/a. ISSN 01480227. doi:10.1029/2003JB002960.

Konrad, S. K., N. F. Humphrey, E. J. Steig, D. H. Clark, N. Potter, and W. T. Pfeffer (1999). Rock glacier dynamics and paleoclimatic implications. *Geology*, **27**(12), p. 1131. ISSN 0091-7613. doi:10.1130/0091-7613(1999)027⟨1131:RGDAPI⟩2.3.CO;2.

Kääb, A. and M. Vollmer (2000). Surface Geometry, Thickness Changes and Flow Fields on Creeping Mountain Permafrost: Automatic Extraction by Digital Image Analysis. *Permafrost and Periglacial Processes*, **11**, p. 315–326.

Lalich, D. E. and J. W. Holt (2017). New Martian climate constraints from radar reflectivity within the north polar layered deposits. *Geophysical Research Letters*, **44**(2), p. 657–664. ISSN 0094-8276, 1944-8007. doi:10.1002/2016GL071323.

Langhammer, L., M. Grab, A. Bauder, and H. Maurer (2019). Glacier thickness estimations of alpine glaciers using data and modeling constraints. *The Cryosphere*, **13**(8), p. 2189–2202. ISSN 1994-0424. doi:10.5194/tc-13-2189-2019.

Laskar, J., B. Levrard, and J. F. Mustard (2002). Orbital forcing of the martian polar layered deposits. *Nature*, **419**(6905), p. 375–377. ISSN 0028-0836, 1476-4687. doi:10.1038/nature01066.

Leonard, E. M., P. Staab, and S. G. Weaver (2005). Kinematics of Spruce Creek rock glacier, Colorado, USA. *Journal of Glaciology*, **51**(173), p. 259–268. ISSN 0022-1430, 1727-5652. doi:10.3189/172756505781829403.

Levy, J. S., C. I. Fassett, J. W. Head, C. Schwartz, and J. L. Watters (2014). Sequestered glacial ice contribution to the global Martian water budget: Geometric constraints on the volume of remnant, midlatitude debris-covered glaciers: Buried martian glaciers. *Journal of Geophysical Research: Planets*, **119**(10), p. 2188–2196. ISSN 21699097. doi:10.1002/2014JE004685.

Levy, J. S., C. I. Fassett, J. W. Holt, R. Parsons, W. Cipolli, T. A. Goudge, M. Tebolt, L. Kuentz, J. Johnson, F. Ishraque, B. Cvijanovich, and I. Armstrong (2021). Surface boulder banding indicates Martian debris-covered glaciers formed over multiple glaciations. *Proceedings of the National Academy of Sciences*, **118**(4), p. e2015971118. ISSN 0027-8424, 1091-6490. doi:10.1073/pnas.2015971118.

Mackay, S. L. and D. R. Marchant (2016). Dating buried glacier ice using cosmogenic 3He in surface clasts: Theory and application to Mullins Glacier, Antarctica. *Quaternary Science Reviews*, **140**, p. 75–100. ISSN 02773791. doi:10.1016/j.quascirev.2016.03.013.

Mackay, S. L. and D. R. Marchant (2017). Obliquity-paced climate change recorded in Antarctic debris-covered glaciers. *Nature Communications*, **8**(1), p. 14194. ISSN 2041-1723. doi:10.1038/ncomms14194.

Mackay, S. L., D. R. Marchant, J. L. Lamp, and J. W. Head (2014). Cold-based debris-covered glaciers: Evaluating their potential as climate archives through studies of ground-penetrating radar and surface morphology: Cold-based debris-covered glaciers. *Journal of Geophysical Research: Earth Surface*, **119**(11), p. 2505–2540. ISSN 21699003. doi:10.1002/2014JF003178.

Mcnabb, R., R. Hock, S. O'Neel, L. Rasmussen, Y. Ahn, M. Braun, H. Conway, S. Herreid, I. Joughin, W. Pfeffer, B. Smith, and M. Truffer (2012). Using surface velocities to calculate ice thickness and bed topography: a case study at Columbia Glacier, Alaska, USA. *Journal of Glaciology*, **58**(212), p. 1151–1164. ISSN 0022-1430, 1727-5652. doi:10.3189/2012JoG11J249.

Meng, T. M., R. Aguilar, M. S. Christoffersen, E. I. Petersen, C. F. Larsen, J. S. Levy, and J. W. Holt (2023a). Photogrammetric Monitoring of Rock Glacier Motion Using High-Resolution Cross-Platform Datasets: Formation Age Estimation

and Modern Thinning Rates. *Remote Sensing*, **15**(19), p. 4779. ISSN 2072-4292. doi:10.3390/rs15194779.

Meng, T. M., E. I. Petersen, and J. W. Holt (2023b). Rock glacier composition and structure from radio wave speed analysis with dipping reflector correction. *Journal of Glaciology*, **69**(275), p. 639–657. ISSN 0022-1430, 1727-5652. doi: 10.1017/jog.2022.90.

Monnier, S., C. Camerlynck, and F. Rejiba (2009). Ground-penetrating radar surveys on rock glaciers in the Vanoise Massif (Northern French Alps): methodological issues Investigations au radar géologique sur des glaciers rocheux dans le massif de la Vanoise (Alpes du Nord françaises): aspects méthodologiques. p. 12.

Morgan, G. A., J. W. Head, and D. R. Marchant (2009). Lineated valley fill (LVF) and lobate debris aprons (LDA) in the Deuteronilus Mensae northern dichotomy boundary region, Mars: Constraints on the extent, age and episodicity of Amazonian glacial events. *Icarus*, **202**(1), p. 22–38. ISSN 00191035. doi: 10.1016/j.icarus.2009.02.017.

Morgan, G. A., N. E. Putzig, M. R. Perry, H. G. Sizemore, A. M. Bramson, E. I. Petersen, Z. M. Bain, D. M. H. Baker, M. Mastrogiuseppe, R. H. Hoover, I. B. Smith, A. Pathare, C. M. Dundas, and B. A. Campbell (2021). Availability of subsurface water-ice resources in the northern mid-latitudes of Mars. *Nature Astronomy*, **5**(3), p. 230–236. ISSN 2397-3366. doi:10.1038/s41550-020-01290-z.

Nerozzi, S. and J. Holt (2018). Earliest accumulation history of the north polar layered deposits, Mars from SHARAD. *Icarus*, **308**, p. 128–137. ISSN 00191035. doi:10.1016/j.icarus.2017.05.027.

Nerozzi, S. and J. W. Holt (2019). Buried Ice and Sand Caps at the North Pole of Mars: Revealing a Record of Climate Change in the Cavi Unit With SHARAD. *Geophysical Research Letters*, **46**(13), p. 7278–7286. ISSN 0094-8276, 1944-8007. doi:10.1029/2019GL082114.

Nerozzi, S., M. R. Ortiz, and J. W. Holt (2022). The north polar basal unit of Mars: An Amazonian record of surface processes and climate events. *Icarus*, **373**, p. 114716. ISSN 00191035. doi:10.1016/j.icarus.2021.114716.

Parsons, R. and J. Holt (2016). Constraints on the formation and properties of a Martian lobate debris apron: Insights from high-resolution topography, SHARAD radar data, and a numerical ice flow model: EURIPUS MONS LDA ANALYSIS.

Journal of Geophysical Research: Planets, **121**(3), p. 432–453. ISSN 21699097. doi:10.1002/2015JE004927.

Parsons, R. A., T. Kanzaki, R. Hemmi, and H. Miyamoto (2020). Cold-based glaciation of Pavonis Mons, Mars: evidence for moraine deposition during glacial advance. *Progress in Earth and Planetary Science*, **7**(1), p. 13. ISSN 2197-4284. doi:10.1186/s40645-020-0323-9.

Perry, M. R., A. T. Russell, M. B. Russell, F. J. Foss, F. C. Chuang, G. A. Morgan, Z. M. Bain, B. A. Campbell, and N. E. Putzig (2023). Three-dimensional imaging of martian glaciated terrain using Mars Reconnaissance Orbiter Shallow Radar (SHARAD) observations. *Icarus*, p. 115716. ISSN 00191035. doi:10.1016/j.icarus.2023.115716.

Petersen, E. I., J. W. Holt, and J. S. Levy (2018). High Ice Purity of Martian Lobate Debris Aprons at the Regional Scale: Evidence From an Orbital Radar Sounding Survey in Deuteronilus and Protonilus Mensae. *Geophysical Research Letters*, **45**(21), pp. 11,595–11,604. ISSN 00948276. doi:10.1029/2018GL079759.

Petersen, E. I., J. S. Levy, J. W. Holt, and C. M. Stuurman (2019). New insights into ice accumulation at Galena Creek Rock Glacier from radar imaging of its internal structure. *Journal of Glaciology*, **66**(255), p. 1–10. ISSN 0022-1430, 1727-5652. doi:10.1017/jog.2019.67.

Plaut, J. J., A. Safaeinili, J. W. Holt, R. J. Phillips, J. W. Head, R. Seu, N. E. Putzig, and A. Frigeri (2009). Radar evidence for ice in lobate debris aprons in the mid-northern latitudes of Mars. *Geophysical Research Letters*, **36**(2), pp. n/a–n/a. ISSN 00948276. doi:10.1029/2008GL036379.

Potter, N. (1972). Ice-Cored Rock Glacier, Galena Creek, Northern Absaroka Mountains, Wyoming. *Geological Society of America Bulletin*, **83**(10), p. 3025. ISSN 0016-7606. doi:10.1130/0016-7606(1972)83[3025:IRGGCN]2.0.CO;2.

Potter, N., E. J. Steig, D. H. Clark, M. A. Speece, G. M. Clark, and A. B. Updike (1998). Galena Creek rock glacier revisited—new observations on an old controversy. *Geografiska Annaler: Series A, Physical Geography*, **80**(3–4), p. 251–265. ISSN 1468-0459. doi:10.1111/j.0435-3676.1998.00041.x.

RGIK (2023). Guidelines for inventorying rock glaciers: Baseline and practical concepts (Version 1.0). *IPA Action Group Rock glacier inventories and kinematics*. doi:10.51363/unifr.srr.2023.002.

Schorghofer, N. (2008). Temperature response of Mars to Milankovitch cycles. *Geophysical Research Letters*, **35**(18), p. L18201. ISSN 0094-8276. doi: 10.1029/2008GL034954.

Smith, I. B., N. E. Putzig, J. W. Holt, and R. J. Phillips (2016). An ice age recorded in the polar deposits of Mars. *Science*, **352**(6289), p. 1075–1078. ISSN 0036-8075, 1095-9203. doi:10.1126/science.aad6968.

Souness, C., B. Hubbard, R. E. Milliken, and D. Quincey (2012). An inventory and population-scale analysis of martian glacier-like forms. *Icarus*, **217**(1), p. 243–255. ISSN 00191035. doi:10.1016/j.icarus.2011.10.020.

Squyres, S. W. and M. H. Carr (1986). Geomorphic Evidence for the Distribution of Ground Ice on Mars. *Science*, **231**(4735), p. 249–252. ISSN 0036-8075, 1095-9203. doi:10.1126/science.231.4735.249.

Steig, E. J., J. J. Fitzpatrick, N. Potter, jr., and D. H. Clark (1998). The geochemical record in rock glaciers. *Geografiska Annaler: Series A, Physical Geography*, **80**(3–4), p. 277–286. ISSN 0435-3676, 1468-0459. doi:10.1111/j.0435-3676.1998.00043.x.

Stuurman, C. M. (2017). *Ridges on martian debris-covered glaciers*. Master's thesis, University of Texas.

Wahrhaftig, C. and A. Cox (1959). Rock glaciers in the Alaska Range. *Geological Society of America Bulletin*, **70**(4), p. 383. ISSN 0016-7606. doi: 10.1130/0016-7606(1959)70[383:RGITAR]2.0.CO;2.

Watters, T. R., B. A. Campbell, C. J. Leuschen, G. A. Morgan, A. Cicchetti, R. Orosei, and J. J. Plaut (2024). Evidence of Ice-Rich Layered Deposits in the Medusae Fossae Formation of Mars. *Geophysical Research Letters*, **51**(2), p. e2023GL105490. ISSN 0094-8276, 1944-8007. doi:10.1029/2023GL105490.

Whitten, J. L. and B. A. Campbell (2018). Lateral Continuity of Layering in the Mars South Polar Layered Deposits From SHARAD Sounding Data. *Journal of Geophysical Research: Planets*, **123**(6), p. 1541–1554. ISSN 2169-9100. doi: 10.1029/2018JE005578.

Östrem, G. (1959). Ice Melting under a Thin Layer of Moraine, and the Existence of Ice Cores in Moraine Ridges. *Geografiska Annaler*, **41**(4), p. 228–230. ISSN 2001-4422. doi:10.1080/20014422.1959.11907953.

Journal of Glaciology

Article

Cite this article: Meng TM, Petersen EI, Holt JW (2023). Rock glacier composition and structure from radio wave speed analysis with dipping reflector correction. *Journal of Glaciology* **69**(275), 639–657. https://doi.org/10.1017/jog.2022.90

Received: 1 April 2022
Revised: 2 August 2022
Accepted: 9 September 2022
First published online: 21 October 2022

Key words:
Debris-covered glaciers; ground-penetrating radar; permafrost; supraglacial debris

Author for correspondence:
Tyler M. Meng, E-mail: tmeng@arizona.edu

cambridge.org/jog

Rock glacier composition and structure from radio wave speed analysis with dipping reflector correction

Tyler M. Meng[1], Eric I. Petersen[2] and John W. Holt[1]

[1]Lunar and Planetary Laboratory, University of Arizona, Tucson, AZ, USA and [2]Geophysical Institute, University of Alaska Fairbanks, Fairbanks, AK, USA

Abstract

We assess the composition and geometry of four individual rock glaciers in Alaska, Wyoming and Colorado by measuring their radio wave speed and applying these results to ground-penetrating radar depth corrections and dielectric mixing models. Our method includes a correction for subsurface reflector dip angle, which we show can lead to an incorrect determination of wave speeds using common midpoint configurations. By observing the radar properties of the rock glaciers and their supraglacial debris, we find that some of the sites exhibit nearly pure ice cores, and all of the sites indicate volumetric ice fractions >50%. These results have implications for terrestrial glaciology and hydrology because the present ice volume is connected to past ice accumulation and subsurface ice preservation, which may affect the future availability of alpine water resources. An understanding of the processes that govern rock glacier evolution over a wide range of latitudes and elevations will also contribute to the exploration of planetary surfaces such as Mars, which hosts a significant population of debris-covered glaciers. Our subsurface composition and geometry estimates will inform simulations of rock glacier formation and evolution to test hypothesized ice origin mechanisms along with the preservation of climate signals.

1. Introduction

Rock glaciers and debris-covered glaciers occupy a unique position in the alpine cryospheric continuum. While the origins of individual features can arise from glacial or periglacial processes (Wahrhaftig and Cox, 1959; Potter and others, 1998; Anderson and others, 2018), they both require high topographic relief and sufficient talus supply to inhibit the surface ablation of an ice unit that viscously deforms downslope with gravity. Their internal structure and stratigraphy contains information about the climatic conditions under which they formed and evolved; internal debris layers could signify broad fluctuations between glacial and interglacial periods (Mackay and Marchant, 2017) or shorter cycles of seasonal snow/firn preservation by rockfall events (Petersen and others, 2019a). Additionally, the presence of folds or brittle fractures depends on viscoelastic properties related to ice/debris clast distribution, particle anisotropy and thermal regime (Giardino and Vitek, 1988; Cuffey and Paterson, 2010). Measuring and monitoring rock glacier/debris-covered glacier structure and volumetric ice fraction has implications for water budget in alpine hydrological systems in changing climates (e.g. Jones and others, 2018a, 2018b). Constraining the properties of such features on Earth also provides information about the total ice volume and surface processes controlling the evolution and preservation of analogous ice-rich features in Mars' midlatitudes (Petersen and others, 2018; Baker and Carter, 2019; Levy and others, 2014, 2021), which in turn has implications for planetary climate science and in situ resource utilization.

Ground-penetrating radar (GPR) is a valuable tool for imaging the subsurfaces of accessible rock glaciers (e.g. Degenhardt and Giardino, 2003; Maurer and Hauck, 2007; Monnier and others, 2008; Monnier and Kinnard, 2013; Florentine and others, 2014; Mackay and others, 2014; Petersen and others, 2019a; see Table 1). The low dielectric loss of ice allows for surveys capable of detecting the base of the ice and resolving internal structure at GPR wavelengths. In order to accurately convert the travel times of recorded radar echoes to depths, it is important to use an accurate dielectric model of the subsurface, which controls the electromagnetic wave propagation speed through the medium. The bulk dielectric permittivity (thus wave speed) is sensitive to the fraction of lithics in an ice/rock mixture, an effect which we explore using dielectric mixing models. We show that variations in wave speed measurements can lead to significant uncertainty in fractional ice volume estimates for individual rock glaciers, which may have a significant effect when extrapolating ice volume over broader rock glacier populations. This demonstrates the importance of accurate wave speed measurements on geometric and compositional constraints for individual rock glaciers and for estimating regional/global buried ice volumes. Here, we analyze the radio wave speed characteristics of four North American rock glaciers and their supraglacial debris layers. These analyses provide new constraints on their composition and geometry, and we discuss our results in the context of previous measurements reported in the literature.

https://doi.org/10.1017/jog.2022.90 Published online by Cambridge University Press

Table 1. List of rock glacier GPR wave speed measurements

Study site	Measured wave speed ($m\ ns^{-1}$)	Reference
Murtèl, Switzerland	0.15^{CMP}	Lehmann and Green (2000)
	–	–
	0.120^{CMP}	Maurer and Hauck (2007)
Forlandet, Svalbard	0.14^{CMP}	Berthling and others (2000)
Hiorthfjellet, Svalbard	0.14^{CMP}	Isaksen and others (2000)
Gilpin Peak, Colorado	0.12^{CMP}	Degenhardt and others (2003)
	–	–
	0.14^{CMP}	This study
Mount Mestas, Colorado	0.15^{CMP}	Jorgensen (2007)
Plan du Lac, France	0.12^{COH}	Monnier and others (2008)
Tumbledown Norte, Antarctica	0.17^{COH}	Fukui and others (2008)
Quebrada Noroeste, Chile	$0.13–0.16^{CMP,\ COH}$	Monnier and Kinnard (2013)
Mullins Valley, Antarctica	0.167^{COH}	Shean and Marchant (2010)
	–	–
	$0.160–0.168^{B,COH}$	Mackay and others (2014)
Lone Peak, Montana	0.157^{CMP}	Florentine and others (2014)
Galena Creek, Wyoming	0.156^{CMP}	Petersen and others (2019a)
	–	–
	$0.16–0.169^{CMP}$	This study
Sulphur Creek, Wyoming	$0.147–0.17^{CMP,\ COH}$	This study
Sourdough, Alaska	0.149^{CMP}	This study

^{CMP}: derived via common midpoint analysis, ^{COH}: derived via common offset hyperbola analysis, ^{B}: derived via borehole depth correlation with radar reflector.

2. Sites and methods

2.1. Study sites

We acquired GPR data between 2018 and 2021 at four rock glaciers: Sourdough Peak, Alaska; Galena Creek, Wyoming; Sulphur Creek, Wyoming and Gilpin Peak, Colorado. These sites provide comparisons between rock glacier populations ranging from ~40° to 60° north latitude and spanning a few kilometers in elevation. Sourdough Rock Glacier is located in the Wrangell Mountains of southeast Alaska. This feature ranges in elevation from ~550 to 1400 m a.s.l. It is ~2.7 km long by 0.8 km wide, and it flows southward (Fig. 1). The peak on which the rock glacier lies is composed of an andesitic hypabyssal volcanic complex intruding a unit of Cretaceous sediments (MacKevett, 1978). There has been no previous geophysical work on Sourdough Rock Glacier, although seismic and electromagnetic surveys on nearby Fireweed Rock Glacier indicated surface debris thicknesses of 2–4 m and bulk glacier thicknesses up to 60 m (Bucki and others, 2004). Observation of an ice exposure at Fireweed Rock Glacier in July 1994 led to estimates of >50% fractional ice volume (Elconin and LaChapelle, 1997). Air temperature measurements at the rock glacier toe between 2016 and 2021 indicate a mean annual air temperature close to freezing. There are also significant valley glaciers with an equilibrium line altitude (ELA) of 1500 m a.s.l. in this region (Anderson and others, 2021), which is ~100 m higher than the upper reaches of Sourdough Rock Glacier. However, it is still unclear whether or not this regional population of rock glaciers contains glacigenic ice or if they are purely periglacial in origin. Our GPR surveys shed light on the specific structure and composition of Sourdough Rock Glacier, and they provide a new contextual measurement for rock glaciers in the Wrangells.

Galena and Sulphur Creek Rock glaciers are located at elevations ranging from 2800 to 3200 m a.s.l. in the Absaroka Mountains of northwest Wyoming, with bedrock consisting of basaltic and andesitic volcanic deposits (Potter, 1972). Galena Creek Rock Glacier flows north (Fig. 2); it is ~1.4 km long by 0.2 km wide. It has been studied extensively, with significant prior debate as to whether the feature was glacial or periglacial in origin. Noel Potter initially advocated for the glacigenic ice-cored formation hypothesis in 1972, while Dietrich Barsch argued against the hypothesis that this site is an ice-cored debris-covered

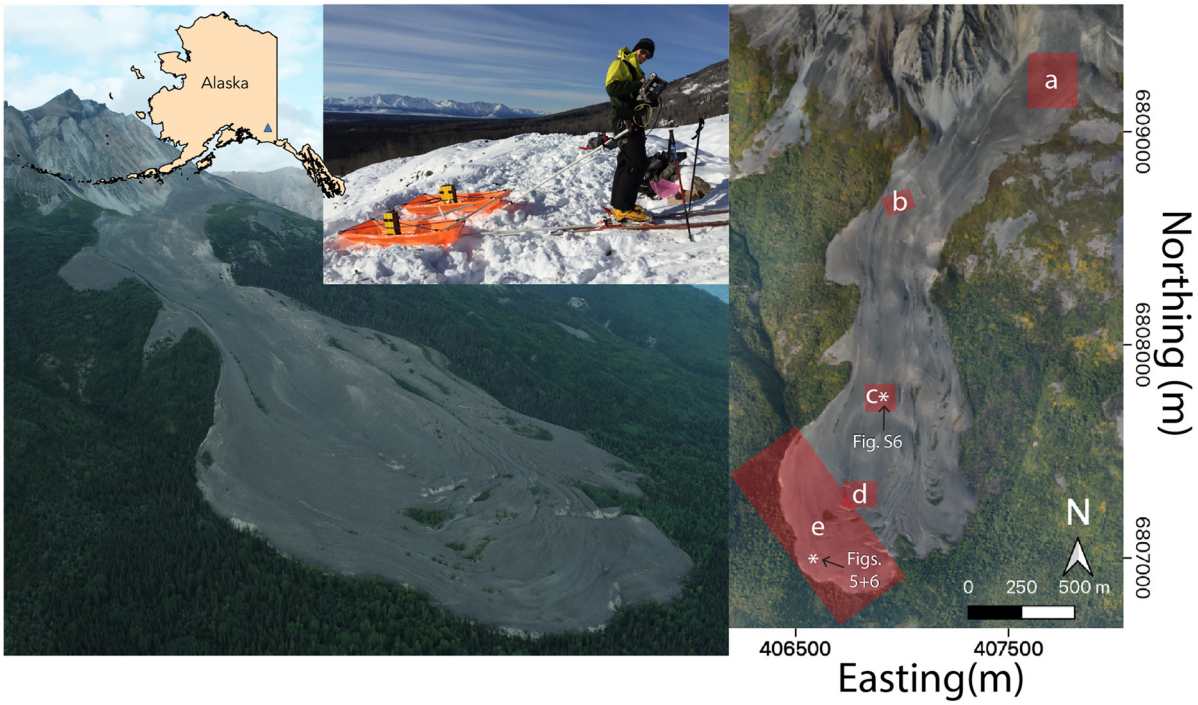

Fig. 1. Sourdough Rock Glacier, Alaska (geographic context shown as blue triangle on Alaska inset). The oblique aerial image acquired in August 2021 (left) highlights the lobate morphology with superimposed furrows and ridges along with the site's topographic relief. Sourdough Peak stands ~1 km higher than the rock glacier snout. Surface conditions during March 2019 GPR data acquisition with sled-mounted antenna configuration are shown in the photographic inset. Highlighted regions in context map (right) show locations of ice and debris thickness results detailed in Figures 7 and 20, respectively. The white asterisks show the locations of the radio wave speed measurements which are detailed in the results section. Map projection: WGS84/UTM 7N.

https://doi.org/10.1017/jog.2022.90 Published online by Cambridge University Press

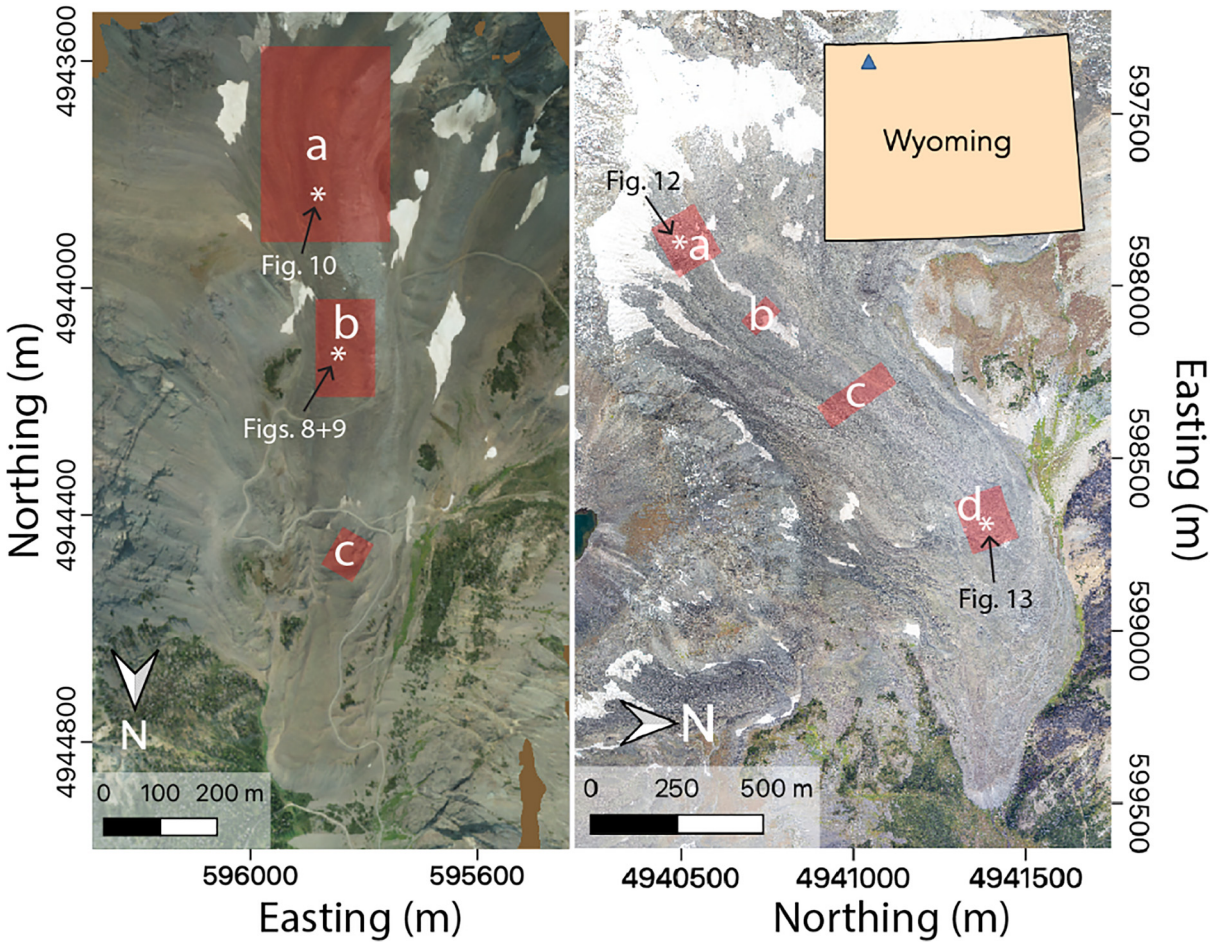

Fig. 2. Context maps of Galena Creek (left) and Sulphur Creek (right) Rock Glaciers, Wyoming. The highlighted areas show locations of ice and debris thickness results detailed in Figures 11 and 19 for Galena Creek and Figures 14 and 18 for Sulphur Creek. The white asterisks show the locations of the radio wave speed measurements which are detailed in the results section. Map projection: WGS84/UTM 12N.

glacier, but instead suggested that it is a periglacial, ice-cemented rock glacier (Barsch, 1987). A borehole at the Galena Creek cirque revealed a nearly pure ice core with a geochemical signature of meteoric glacier ice, strongly supporting the existence of a buried ice core (Clark and others, 1996; Potter and others, 1998; Steig and others, 1998). More recently, GPR surveys have revealed dipping internal layers and resulted in a measured radio wave speed of ~0.16 m ns^{-1} (Petersen and others, 2019a). These observations are consistent with a high bulk ice fraction, but there are new questions about the continuity, age and evolutionary history of the subsurface ice deposits. Regional estimates suggest a mean annual air temperature below freezing and an ELA of ~3000 m a.s.l., close to the heads of each rock glacier (Potter, 1972). The neighboring Sulphur Creek Rock Glacier is ~3 km south of the Galena Creek cirque. It flows northeast and is ~2.2 km long by 0.6 km wide (Fig. 2). We are not aware of prior published geological or geophysical analysis focused on Sulphur Creek, and it provides an opportunity to compare and contrast the characteristics of two rock glaciers in the same geographic region.

Located in southwest Colorado and ranging from 3700 to 4000 m a.s.l., Gilpin Peak Rock Glacier offers a relatively low-latitude and high-elevation site to study preserved ice in North America. It trends northeast with dimensions ~0.7 km long by 0.4 km wide, making it the smallest of our study sites by surface area (Fig. 3). It is located in the San Juan Mountains, which is a volcanic field consisting of flows, breccias and tephra of intermediate to felsic composition (Degenhardt and others, 2003). Nearby weather stations suggest mean annual air temperatures at or below freezing at elevations above 3700 m a.s.l., and the orographic snowline in the San Juan range has been measured between 3700 and 4000 m a.s.l., which is close to the modern ELA (Leonard, 1984). This rock glacier was previously surveyed with GPR at 25 and 50 MHz by Degenhardt and others in the 2000 and 2001 field seasons and the results were published in 2003, which we use as comparison for our 2019 survey (Degenhardt and others, 2003; Fig. 3). The 2003 study concluded that this rock glacier is predominantly periglacial in origin, consisting of 60–70% lithics with some clean ice lenses and flowing downslope from the cirque in discrete lobes. They reported an interpreted GPR wave speed of 0.12 m ns^{-1}. These results provide an estimation for the composition and suggest a predominantly periglacial formation mechanism for rock glaciers throughout the San Juan region. Our objective at this site was to survey Gilpin Peak Rock Glacier with higher GPR frequencies (50, 100 and 200 MHz) in order to measure debris thickness, detect internal reflectors and further estimate the rock glacier composition through wave speed measurements in comparison with the results of Degenhardt and others (2003).

2.2. Data and methods

For GPR data collection, we used a Sensors and Software PulseEKKO system with 50, 100 and 200 MHz antennas. The acquisition parameters for each antenna pair and survey configuration are described in Table S1. Common offset surveys, diagrammed schematically in Figure 4a, were employed to image

https://doi.org/10.1017/jog.2022.90 Published online by Cambridge University Press

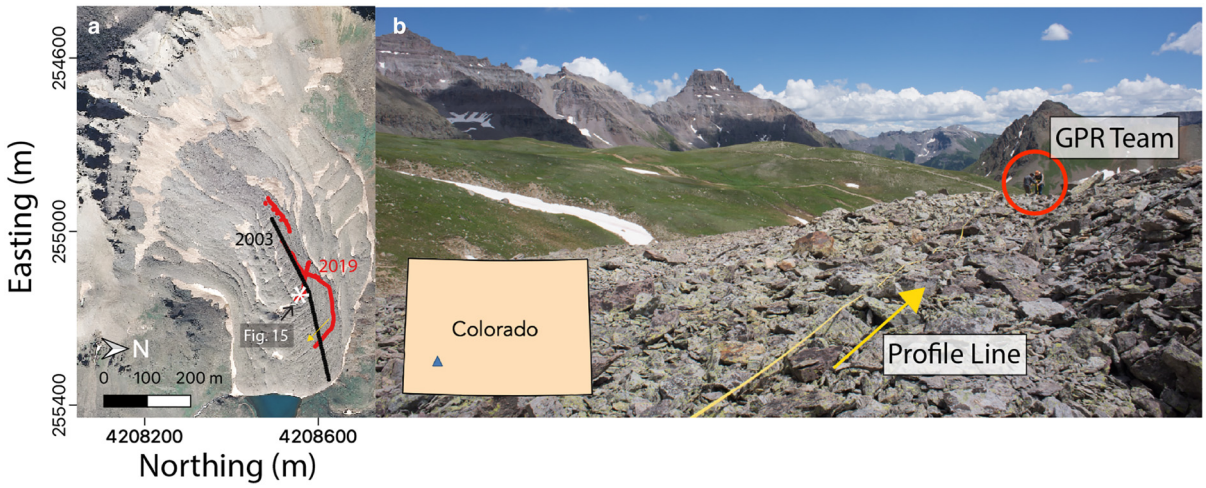

Fig. 3. Gilpin Peak Rock Glacier, Colorado (a) context map showing locations of the 2003 (black line) and 2019 (red line) GPR survey lines, along with the location of the radio wave speed measurement detailed in Figure 15 (white asterisk). (b) Southeast-facing photograph showing the surface conditions while team members conduct a 200 MHz GPR survey in August 2019. The yellow arrow denoting the profile line corresponds to the yellow arrow in (a). Map projection: WGS84/UTM 13N.

subsurface contrasts in the dielectric permittivity at the glacier base, internal interfaces and the bottom of the supraglacial debris layer. For the March 2018 and March 2019 campaigns to Sourdough, Alaska, the common offset traces were collected continuously using sleds for efficient movement over the seasonal snowpack. This required a broadside parallel antenna orientation and 1 m antenna offset for all frequencies. The snowpack was <1 m thick and compressed further by our survey efforts, therefore it was thinner than the vertical resolution associated with our antenna wavelengths. All of the datasets collected in the summer, including an August 2021 campaign to Sourdough, were acquired point-by-point in a broadside perpendicular configuration, where antenna offset and step size increase with decreasing frequency (Supplementary Table S1). The positioning system used to record the locations of each GPR trace was a Topcon SGR-1 DGPS receiver attached to the PulseEKKO operator. This DGPS system allows geolocation of GPR measurements with a horizontal accuracy of 0.4 m and a vertical accuracy of 0.6 m.

To accurately assess the subsurface depth of GPR reflectors measured with two-way travel time (TWTT) between transmitter and receiver, we must assume a radio wave propagation speed (thus assuming a relative dielectric permittivity) through the medium between the surface and the reflector. We collected common midpoint profiles (CMPs) on each rock glacier, which allow us to geometrically estimate the wave speed assuming a known ray path (Fig. 4b) using the normal moveout equation corrected for a dipping reflector:

$$\left(\frac{v}{\cos\theta}\right)^2 = \frac{x^2}{t^2 - t_0^2} \tag{1}$$

where x is the antenna offset, t is the two-way travel time, t_0 is the zero-offset travel time, θ is the apparent dip of the subsurface reflector relative to the CMP survey and v is the bulk radio wave speed of the medium (Yilmaz, 1987). Equation (1) demonstrates that if one assumes a flat reflector ($\theta = 0$) when the true dip of the subsurface reflector is >0, the apparent velocity will exceed the true velocity of the medium by a factor that increases with increasing dip angle. Since common offset data from several past studies have demonstrated the presence of dipping radar reflectors within rock glaciers (Fukui and others, 2008; Florentine and others, 2014; Mackay and others, 2014; Petersen and others, 2019a), it is essential to analyze the subsurface structure using co-located common offset profiles when making wave speed measurements and compositional estimates with CMP on geophysical targets.

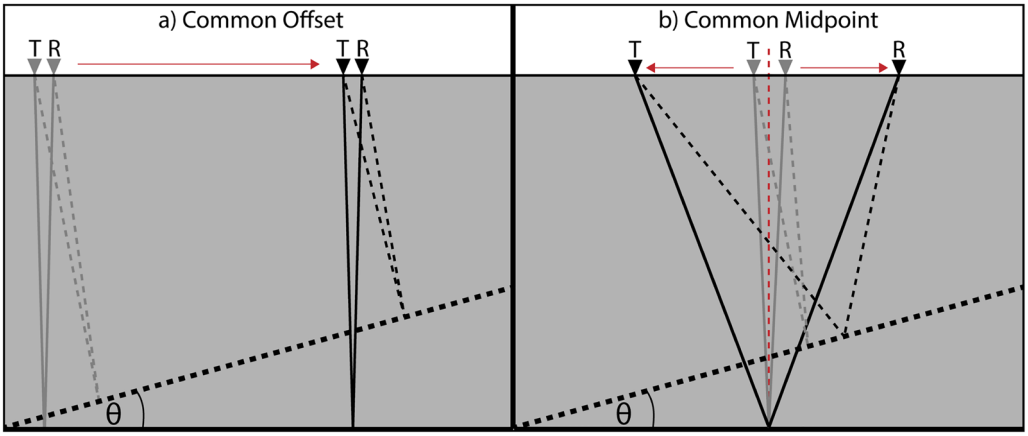

Fig. 4. Common offset (a) and common midpoint (b) configurations for measuring subsurface geometry and radio wave speed. The dashed lines illustrate the effects of a dipping reflector on the reflected ray path between transmitter (T) and receiver (R). The red dashed line in (b) denotes the center of the CMP.

https://doi.org/10.1017/jog.2022.90 Published online by Cambridge University Press

For each CMP survey, we manually interpreted horizons with the goal of tracing continuous hyperbola-shaped arrivals, ranging in number from three to ten per profile depending on data continuity and depth of deepest arrival. We chose to manually pick these horizons due to ambiguous results from the CMP/WARR processing algorithm in Sensors and Software EKKO Project software. We fit our picks to Eqn (1) in a least squares sense to solve for zero-offset travel time t_0 and apparent wave speed $v_a = v/\cos\theta$. The std dev. of travel time residuals between the interpreted horizon and the least squares solution is propagated to estimate an apparent wave speed uncertainty.

As a point of comparison, we plot this least squares best fit alongside the wave speed obtained by applying Eqn (1) to the minimum travel time and maximum offset data points for each horizon (labeled 'high offset' in Figs 5, 8–10, 12, 13 and 15). To determine the dip of the reflector and estimate the true bulk wave speed, we picked horizons in the co-located common offset image which correlate in travel time with horizons in the CMP data to determine a horizontal position/travel time relationship for the selected reflector. For common offset reflectors with a dip angle that changes within the ~40 m boundary of the CMP section, we used the maximum dip angle within that section to estimate an upper bound for the required wave speed correction. A geometric equivalence between dip angle and wave speed can also be established for common offset data:

$$\frac{\sin\theta}{v} = \frac{\Delta t}{2\Delta x} \tag{2}$$

where Δx and Δt represent the changes in the reflector's horizontal position and travel time, respectively (Yilmaz, 1987). With co-located common midpoint and common offset data, we can find the intersection of Eqns (1) and (2) to solve for the combination of wave speed and dip angle that is most consistent with both datasets at each location. This workflow is illustrated in Figure 5. We use the wave speed results to inform our depth corrections of GPR-derived ice and debris thickness measurements for all common offset profiles collected on the targeted rock glaciers (see Results).

To estimate the uncertainty of our wave speed and composition measurements, we calculated the std dev. of the travel time residuals with respect to the least squares fit for each horizon. Since the std dev. for the linear solution has units of time squared, this std dev. is propagated through Eqn (1) to estimate the associated upper and lower bounds for wave speed in units of m ns^{-1}, assuming higher order terms are negligible and that there is no error in the t_0 estimate. These uncertainties are converted to bounds for fractional ice composition at the survey location (Table 2) using three variations of a unified ice/rock dielectric mixing model (Sihvola, 2008) which assumes isotropic spherical inclusions. This model varies a dimensionless homogenization parameter to estimate fractional compositions under Maxwell Garnett, Bruggeman and coherent potential approximations. We compare these mixing models with the complex refractive index method, which has been previously applied to dielectric measurements in hydrological experiments (Knight and Endres, 1990). For all mixing models, we assume a dielectric constant of 3 for ice (Matsuoka and others, 1997) and 9 for debris (Campbell and Ulrichs, 1969) due to the igneous and metamorphic bedrock which supplies the debris at our study sites. Using this method, the upper velocity and ice fraction uncertainties are slightly larger than the lower uncertainties due to the square root relationship between the residuals of the linearized least squares solution and the wave speed term in Eqn (1). The physical upper wave speed limit in pure ice is assumed to be 0.17 m ns^{-1} ($\varepsilon_{ice} \sim 3$) because porosities required to further decrease bulk dielectric constant are considered unrealistic.

In addition to the CMP wave speed analysis, we also use the GPR data to observe wave speed trends in diffraction hyperbolas and headwave arrivals. To specifically target the wave speed in surface debris, we excavated the debris layer at a location on Sulphur Creek Rock Glacier where the shallow debris/ice interface was resolved in a 200 MHz GPR profile. The objective of this experiment was to directly measure the debris thickness at this location and tie it with the travel time measurement from the GPR, thus providing an independent measurement of the wave speed in the debris for comparison with CMP estimates. It also allowed for direct observation of the structure of the debris layer, which can assist in understanding the surface processes governing debris accumulation and the nature of the debris/ice contact.

3. Results

3.1. Sourdough, Alaska

Three CMP surveys were collected in March 2019 – one for each antenna frequency – at one location near the rock glacier toe (marked SP19; Figs 5, 7 and 7e). The co-located common offset sections show that these profiles were acquired over a relatively thin portion of the glacier with a continuous, flat base (Fig. 5b, with context shown in Fig. S1). The CMP for each frequency displays an identifiable, continuous reflection corresponding to the glacier base (Fig. 6). The three CMP datasets were analyzed using the least squares wave speed fit, which consistently found bulk wave speeds of ~0.149 m ns^{-1} with uncertainties ~0.005 m ns^{-1}. These uncertainties are the lowest for all velocities calculated among the sites visited, which we postulate is primarily due to the smoothness and continuity of the rock glacier base along this 40 m section. Comparison with the common-offset profile of this location confirms a nearly flat base, so there is no significant dipping reflector correction and we use this wave speed of 0.149 m ns^{-1} as the baseline for depth correcting the common-offset transects on Sourdough (Fig. 7). The measured bulk thickness of the rock glacier ranges from ~10 to 50 m, with the thickness patterns indicating the presence of a subglacial trough which directs the rock glacier's flow.

Two more CMP datasets were collected at the Sourdough site in August 2021, one of which was located at the SP19 location, with the other measurement collected at a higher elevation on the rock glaciers, labeled SP21a (Figs 7c, S5 and S6). Location SP19 returned a wave speed of 0.15 m ns^{-1}, replicating the March 2019 measurement, while SP21a indicated a wave speed of 0.14 m ns^{-1}. CMP measurements were not collected near the upper end of the rock glacier due to time constraints. After applying the two-phase dielectric mixing models for the permittivities of ice and rock, we find the fractional ice composition of this CMP section ranges between 69 and 81%, with the best fit at 75%. The uncertainty in the velocity measurement contributes significantly more to the uncertainty in composition than the type of dielectric mixing model used, and this is consistent for all of the rock glacier analyses described below. In Figure 6, we observe that a shallow horizon consistent with the debris/ice interface has a best fit wave speed of ~0.18 m ns^{-1}, exceeding the 0.17 m ns^{-1} upper bound for pure ice, which we discuss further in Section 4.3.

3.2. Galena Creek, Wyoming

We acquired common offset and common midpoint GPR surveys along longitudinal and transverse transects of the rock glacier.

https://doi.org/10.1017/jog.2022.90 Published online by Cambridge University Press

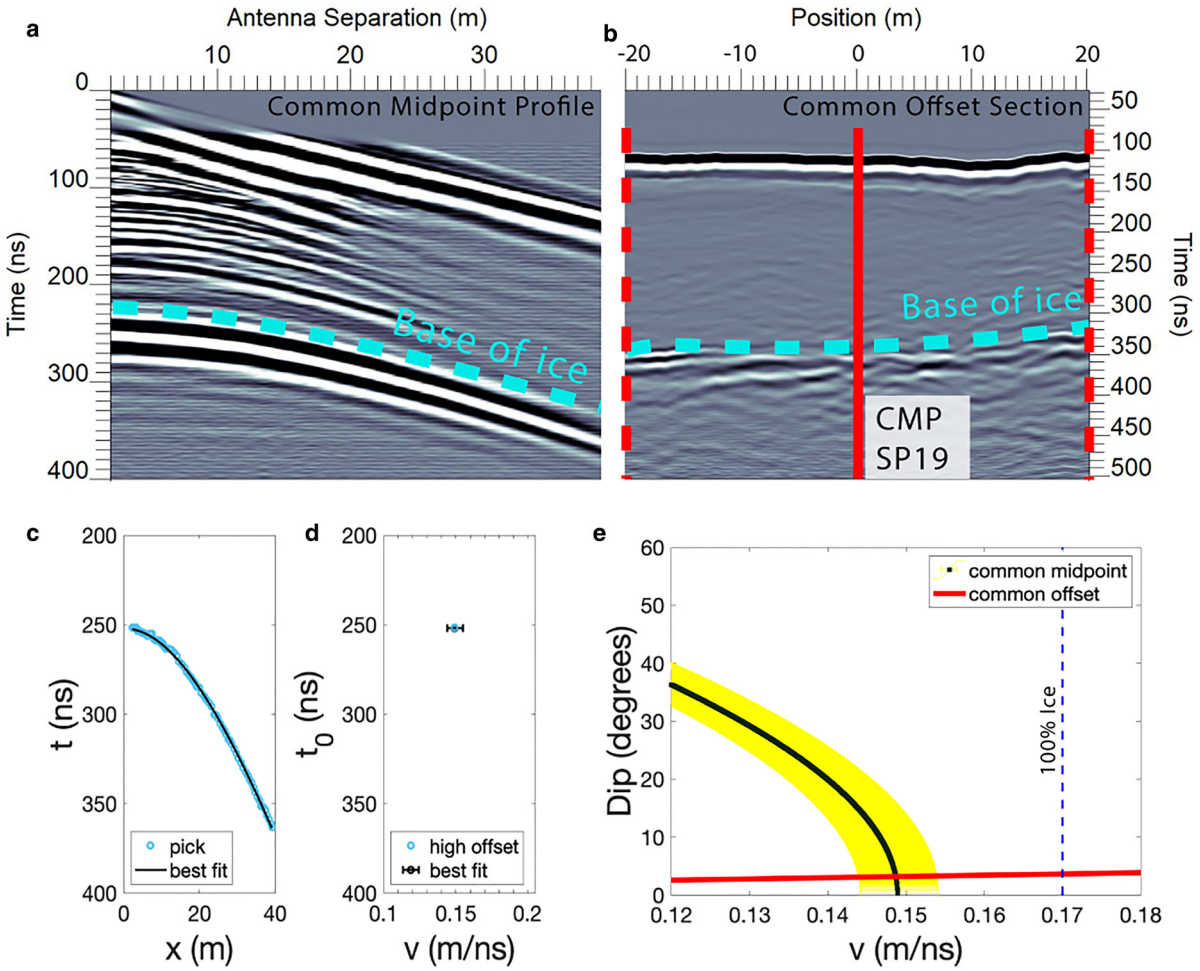

Fig. 5. Example workflow of the least squares fit and dipping reflector analysis using 50 MHz GPR data from Sourdough, Alaska. (a) Common midpoint radargram showing increase in travel time with increasing antenna offset. (b) Common offset profile showing the travel time recorded along a surface transect, revealing a cross section of the subsurface. The blue dashed line shows the reflector used for the analysis. The solid red line in (b) represents the common midpoint location, the dashed red lines indicate maximum antenna separation for the CMP surveys (40 m) and the *x*-axis represents the distance northwest of the common midpoint location. (c) The interpretation (blue circles) and least squares fit to Eqn (1) (black line). The corresponding parameters for best fit zero-offset travel time and wave speed are plotted in (d) with the std dev. of the travel time residuals propagated to wave speed uncertainty. The common midpoint and common offset data combine to solve for wave speed and dip angle in (e) at the intersection of Eqns (1) and (2). The 1σ uncertainty region is shaded yellow and the assumed wave speed of 0.17 m ns^{-1} for pure ice is plotted as a blue dashed line. In this example, the best fit wave speed is interpreted to be 0.149 m ns^{-1} with a reflector dip angle of ~3°.

The surveys were acquired in two distinct zones of the rock glacier: the mid-glacier trunk and the upper cirque. Four CMP surveys were acquired in the glacier trunk, centered on two midpoints. The first pair (Figs 8 and 9) was collected at location GC2020a and were oriented approximately perpendicular to one another in order to test the effect of the survey orientation on the measured wave speed. Both surveys initially yielded wave speeds greater than our assumed physical upper limit in ice (0.17 m

Table 2. Wave speed and ice fraction results by study site and CMP location

	Latitude (°N)	Longitude (°W)	CMP elevation (m a.s.l.)	Wave speed (m ns^{-1})	Ice fraction[a]
Gilpin Peak, CO	37.991	107.788	3770	0.139 (GP19)	[0.53 **0.64** 0.74]
			–	–	–
				0.143 (D+03)	[0.61 **0.69** 0.76]
Sourdough, AK	61.385	142.747	555	0.149 (SP19)	[0.69 **0.75** 0.81]
			790	0.143 (SP21)	[0.62 **0.69** 0.75]
Galena Creek, WY	44.642	109.791	2940	0.168 (GC20)	[0.86 **0.95** ~1]
			–	–	–
			3030	0.165 (GC19)	[0.86 **0.93** ~1]
			–	–	–
			3070	0.160 (GC16)	[0.78 **0.86** 0.94]
Sulphur Creek, WY	44.615	109.760	2875	0.147 (SC20b)	[0.62 **0.73** 0.84]
			–	–	–
			3140	0.170 (SC20a)	[0.89 **0.97** ~1]

[a]Reported set of values indicates 1 std dev. in the residuals of the least squares wave speed fit propagated to the ice fraction, where the bolded value represents the best fit corresponding to CMP wave speed.

https://doi.org/10.1017/jog.2022.90 Published online by Cambridge University Press

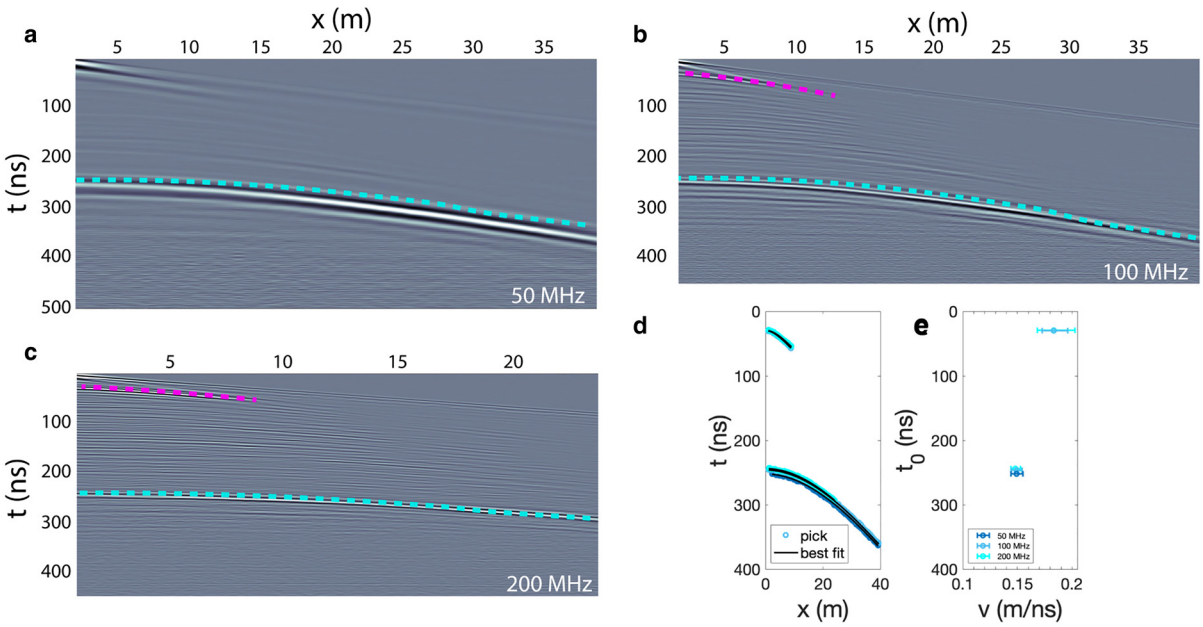

Fig. 6. Collection of best fit wave speed measurements collected for (a) 50, (b) 100 and (c) 200 MHz at Sourdough, AK (common midpoint SP19). (d) The superimposed interpretations from all three frequencies and (e) the corresponding wave speed fits. While the interpreted bulk wave speed is 0.149 m ns^{-1}, we observe that the shallow reflector in the 100 and 200 MHz profiles produces a greater wave speed (~0.18 m ns^{-1}) than the assumed value for pure ice. This shallow reflector is drawn as a magenta dashed line in (b) and (c).

ns^{-1}) before a reflector dip correction, but the common-offset surveys show that the reflector is dipping relative to the surface in both orientations. After applying a dip correction for each orientation, both surveys return a wave speed of 0.167 m ns^{-1} and apparent reflector dips of ~12° and 25°.

Figure 8 shows the results for the longitudinal orientation, while Figure 9 shows the results for the transverse survey at this location. This equivalent corrected wave speed for the same sample location at different CMP orientations supports the hypothesis that reflector dip influences the apparent radio wave speed using CMP surveys. This analysis suggests that the dip of the reflector should be considered when conducting a rock glacier CMP survey, especially when the dip of the reflector exceeds ~10° relative to the surface.

A second pair of CMP surveys (Figs S2 and S3) was collected at GC20b, ~15 m west of GC20a, in order to test the lateral change

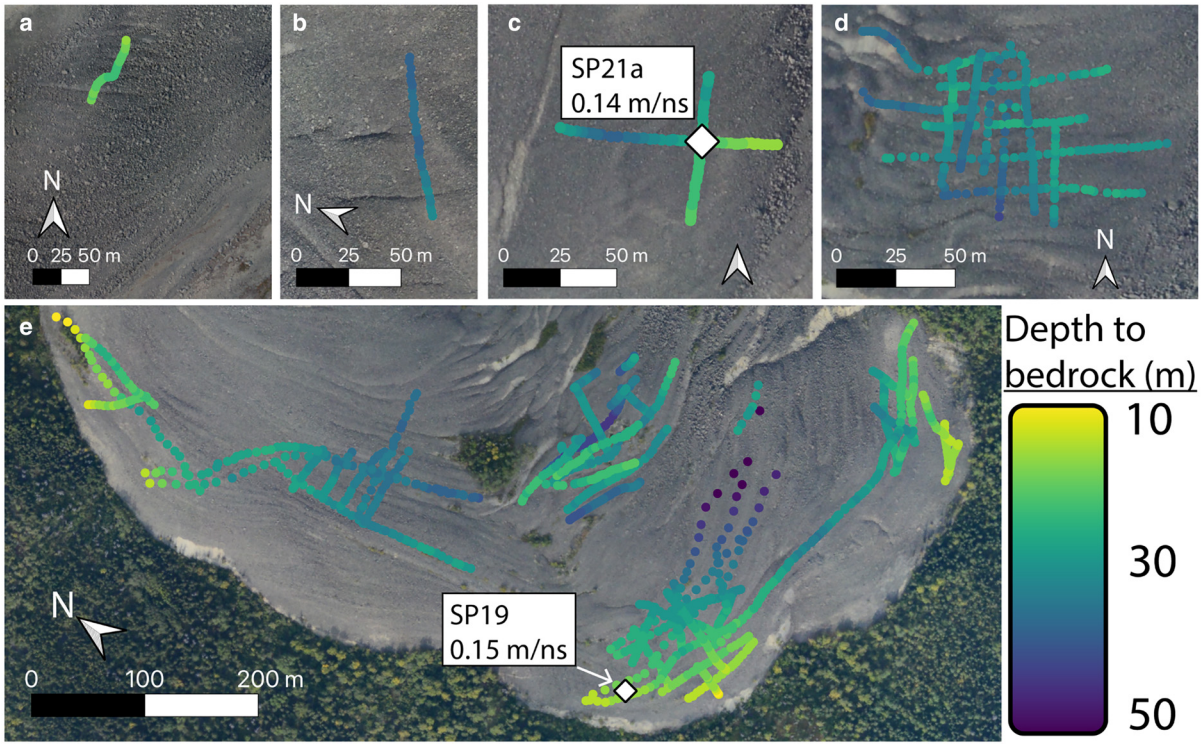

Fig. 7. Bulk Sourdough Rock Glacier thickness estimated from 2016, 2018, 2019 and 2021 GPR survey data. The location of each map panel is shown in Figure 1. The diamonds show the locations of wave speed measurements SP19 and SP21a, detailed in Figures 5, 6 and S4–S6. Map projection: WGS84/UTM 7N.

https://doi.org/10.1017/jog.2022.90 Published online by Cambridge University Press

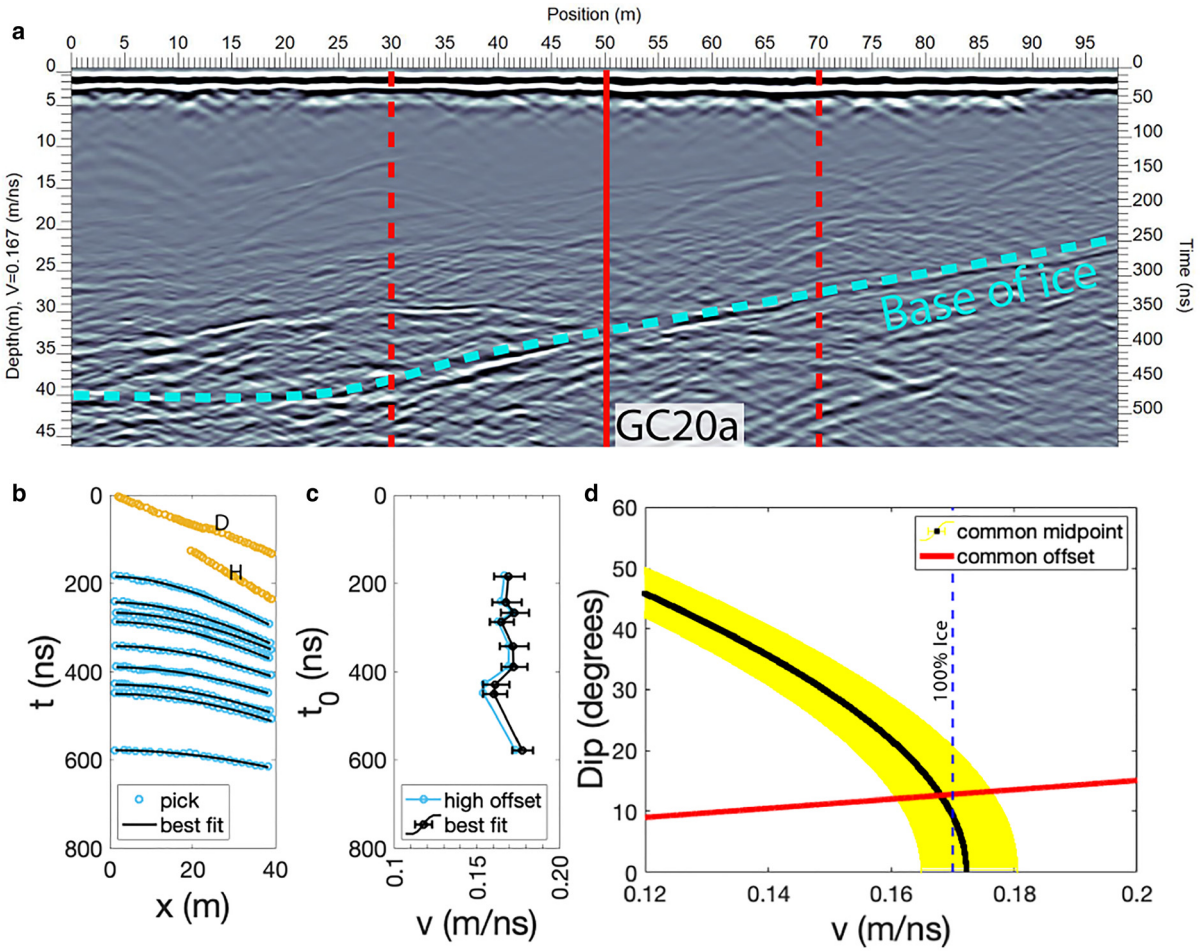

Fig. 8. 50 MHz longitudinal transect and CMP wave speed analysis results along the trunk of Galena Creek, Wyoming at CMP location GC20a. The gold segments in (b) indicate interpreted direct and headwave arrivals in the data, labeled 'D' and 'H', respectively. The wave speed here is estimated to be 0.168 m ns^{-1} (d).

in rock glacier composition and geometry. One survey was collected at 50 MHz and the other was collected at 200 MHz, and they shared the same transverse orientation. Both of these surveys indicate a wave speed of 0.167 m ns^{-1} and a 10° subsurface dip from a reflector that has a low-offset travel time of ~250 ns. Since all four of these adjacent measurements center around the value of 0.167 m ns^{-1} with an uncertainty of ~0.01 m ns^{-1}, this wave speed is assumed for all of the depth corrections of the common-offset radargrams collected at the glacier trunk. These surveys are nearest to the recovered ice core described by Clark and others (1996) and Steig and others (1998), and this proximity is consistent with the high ice fraction at depth inferred from the wave speed. The 200 MHz survey at GC20b also resolved a near surface reflector interpreted to be the debris/ice interface corresponding to a wave speed of ~0.11 m ns^{-1}, and these results are discussed in comparison with other debris wave speed measurements below.

In addition to the CMP experiments conducted at the mid-glacier trunk, another CMP was collected with a longitudinal profile where the slope breaks at the exit to the upper cirque (GC19; Fig. 10). The least squares fit and reflector dip correction returned a wave speed of 0.165 m ns^{-1} with a reflector dip of ~7°, consistent with very high ice content at this location on the glacier. We use this result of 0.165 m ns^{-1} as the bulk velocity for depth corrections of common offset GPR profiles collected near CMP GC19 at the cirque outlet. The locations and wave speed results for the Galena Creek CMP surveys are mapped in Figure 11, along with the corresponding bulk rock glacier thickness estimates. The rock glacier ranges in thickness from ~5 to 60 m, demonstrating the presence of a narrow but thick ice deposit in the center of the valley surrounded by remnant moraines.

3.3. Sulphur Creek, Wyoming

Our campaign produced the first known GPR datasets at Sulphur Creek. We acquired common offset and common midpoint surveys on the upper (SC20a) and lower (SC20b) portions of the rock glacier system. After least squares analysis and comparison with diffraction hyperbolas in the common offset data, this rock glacier displays two zones with distinct radio wave speeds: the upper rock glacier has a wave speed near that of pure ice (~0.17 m ns^{-1}, Fig. 12), while the lower rock glacier shows a significantly lower wave speed of ~0.147 m ns^{-1} after correcting for a 30° reflector dip (Fig. 13), indicating a dielectric constant consistent with a volumetric ice fraction of ~⅔. This decrease in ice content supports the interpretation of a transition from a debris-covered cirque glacier to an ice-cored rock glacier along the longitudinal profile of the valley (Petersen and others, 2019b).

Although the 1σ uncertainties of these wave speeds are both ~0.01 m ns^{-1}, we consider 0.17 m ns^{-1} to be the physical upper bound for pure glacial ice and assume this value for the depth corrections of ice thickness on the upper rock glacier (Fig. 14a–c). The wave speed of 0.147 m ns^{-1} is assumed for depth corrections on the lower rock glacier (Fig. 14d), and the uncertainty envelope here allows for an ice fraction ranging from 62 to 84% (Table 2). After applying the two wave speed measurements to the upper and lower parts of the rock glacier, the upper ice-cored zone exhibits a thickness ranging from ~2 to 20 m of pure ice, while the

https://doi.org/10.1017/jog.2022.90 Published online by Cambridge University Press

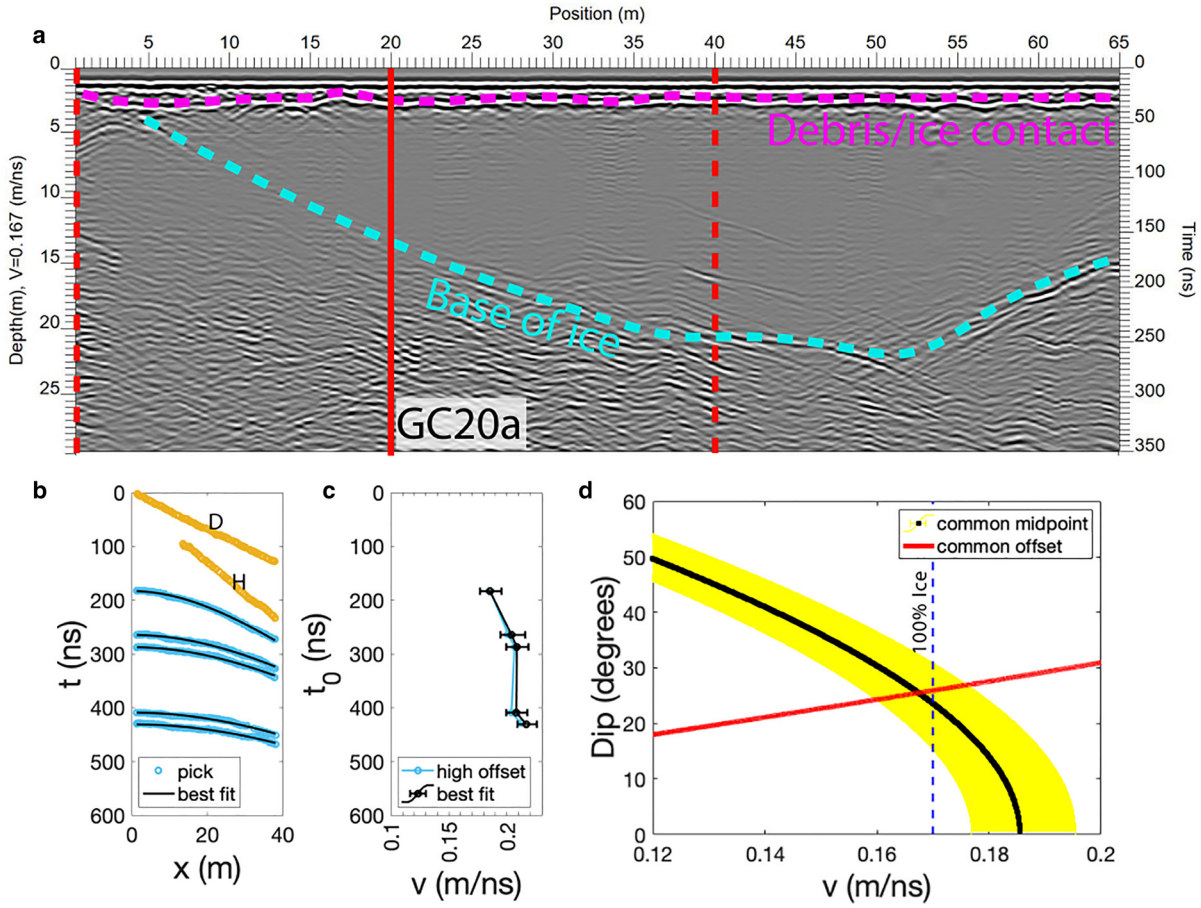

Fig. 9. (a) 200 MHz transverse transect showing location of the CMP at location GC20a and perpendicular to that in Figure 8. The blue dashed line represents the interpreted reflector at the base of the ice, used for the dipping reflector analysis. The magenta dashed line shows the flat near-surface debris/ice interface. The gold segments in (b) indicate interpreted direct and headwave arrivals in the data, labeled 'D' and 'H', respectively. After correcting for dipping reflectors (d), the wave speed is estimated to be 0.167 m ns^{-1}.

lower section indicated ice-cemented debris occupying a trough almost 40 m deep.

3.4. Gilpin Peak, Colorado

We acquired CMP data, debris thickness measurements and images of rock glacier structure at 50, 100 and 200 MHz. The 50 MHz CMP was located over complex dipping reflectors, which led to a value of 0.17 m ns^{-1} for the initial bulk wave speed fit when assuming a flat reflector (Fig. 15). However, previous results and the thick debris layer on the lower portion of the rock glacier suggest the wave speed should be lower than that of pure ice. Applying the travel time slope of 10 ns m^{-1} derived from subsurface reflectors in the common offset image can explain the unexpectedly high best fit apparent wave speed. This travel time slope corresponds to a reflector dipping ~35° below a medium of 0.14 m ns^{-1} (~65% ice), which is greater than the 0.12 m ns^{-1} wave speed interpreted from the Degenhardt and others (2003) survey. The difference in these wave speed measurements could have a significant effect on regional estimates of ice storage, both through calculated rock glacier volume and ice fraction, and we discuss the discrepancy between measured wave speed values below. Using the updated value of 0.14 m ns^{-1}, we find that Gilpin Peak Rock Glacier approaches a thickness of 45 m of ice-cemented debris (Fig. 16a). The thickness of the debris ranges from 1.1 to 2.4 m (Fig. 16b) and the properties of this supraglacial debris layer are discussed in the context of all of our field sites in the following section.

3.5. Properties of the supraglacial debris

After estimating the bulk rock glacier radio wave speed through CMP analysis and dip correction, estimating the wave speed of the supraglacial debris layer further constrains the dielectric properties of the rock glacier and provides more robust GPR measurements of debris thickness. The relatively thin debris layer (~2 m) at each of our field sites prohibits shallow CMP wave speed measurements with 50 and 100 MHz surveys because their wavelengths are comparable to the thickness of the debris which leads to the direct and refracted headwave arrivals obscuring the debris/ice reflection, especially at larger offsets. However, we collected 200 MHz CMP surveys at Galena Creek and Sourdough that both resolved a shallow reflection consistent with the low-offset travel times of the interpreted debris–ice contact.

At Sulphur Creek, the upper cirque contained relatively thin debris (<1 m), which provided an opportunity to directly observe the debris/ice contact. We acquired a 200 MHz GPR profile where a shallow reflection interpreted as the debris/ice interface is detected, so we excavated through the debris layer at this location to directly measure wave speed by dividing the measured depth by one-way travel time. Our observations at this excavation location are illustrated in Figure 17 and mapped in comparison with other manual and GPR-derived debris thickness measurements at Sulphur Creek in Figure 18. We found grain sorting within the debris at this excavation along with the pits dug in thinner debris: grain size consistently decreases with depth in the debris layer. The relative roles of water infiltration and debris motion with glacier flow in the sorting of debris clasts remain unknown, but the

https://doi.org/10.1017/jog.2022.90 Published online by Cambridge University Press

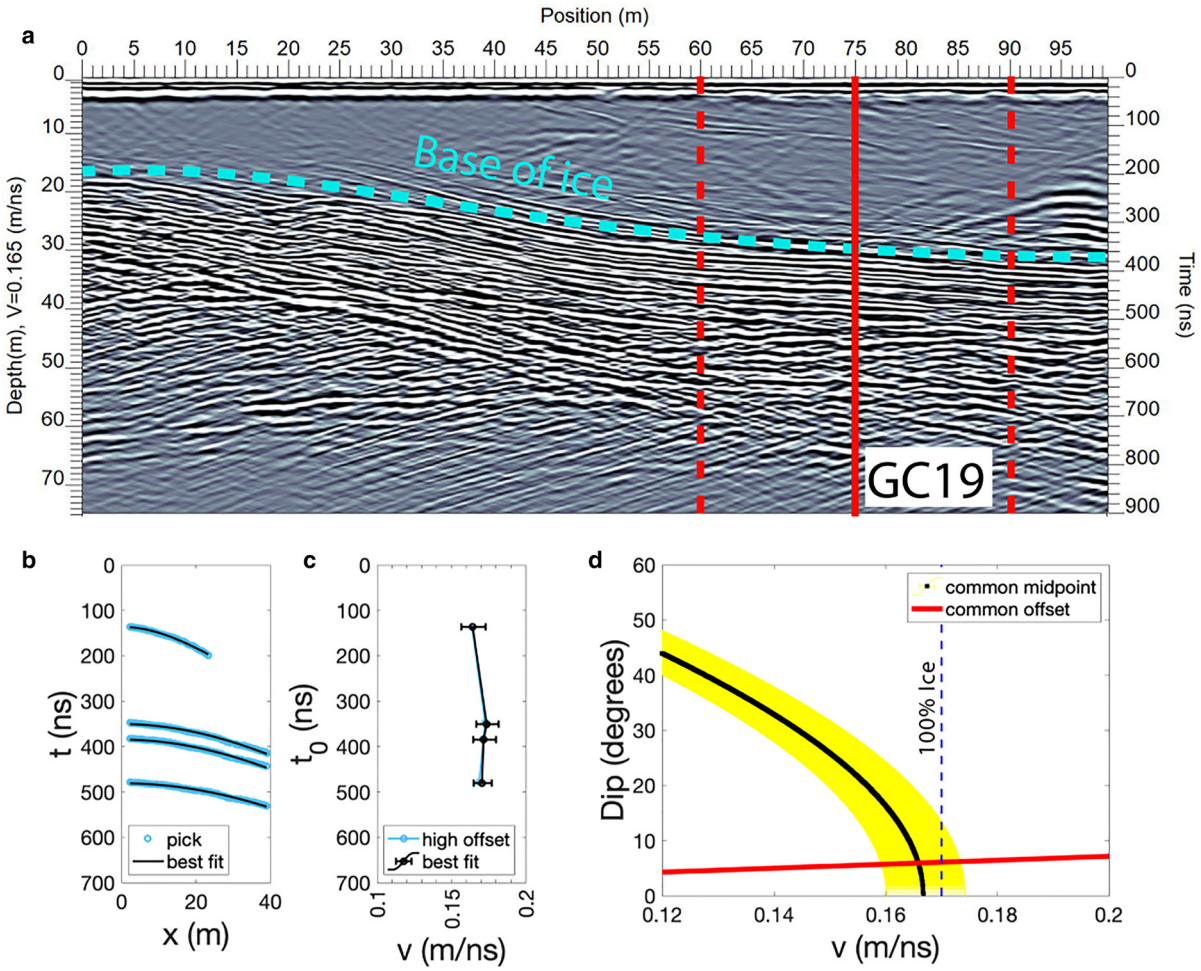

Fig. 10. 50 MHz longitudinal profile at the cirque outlet of Galena Creek, Wyoming (CMP location GC19) shown with the results of the wave speed and dipping reflector analysis, indicating a wave speed of ~0.165 m ns^{-1}.

excavation revealed a significant amount of pore water under a pressure gradient that continuously filled the bottom of excavation. Additionally, we observed an impermeable layer of refrozen, ice-cemented debris overlying clean ice assumed to be of glacial origin, further suggesting a significant role of meltwater in the evolution of terrestrial rock glaciers. Future work may consider three-phase dielectric mixing models in order to include the contributions of liquid water or pore space.

Since there is a thin transition zone of ice-cemented debris in the observed debris profile and only one discernible shallow reflection in the GPR profile, it is possible that we are detecting the return from the top of the ice-cemented debris and associated water film at 70 cm, we may be detecting the interface between the ice-cemented debris and glacial ice at 90 cm or the return could be the superposition of reflections from both interfaces since the ice-cemented layer is thinner than the GPR vertical resolution. With

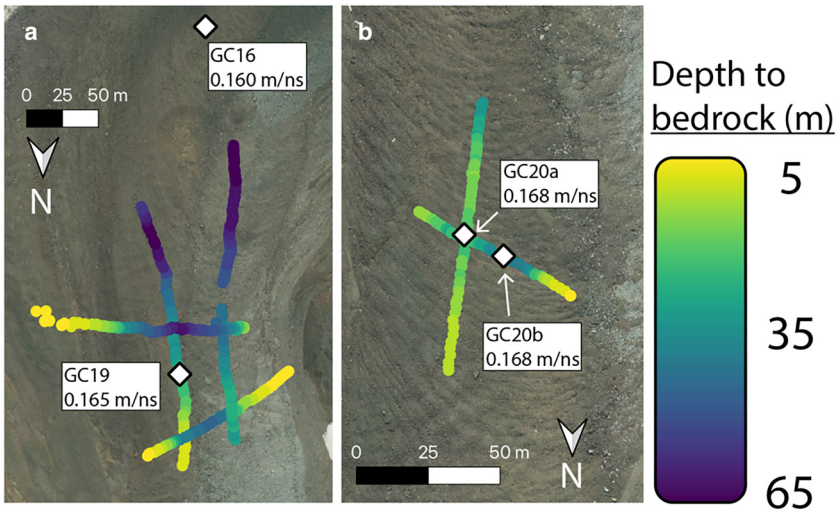

Fig. 11. Bulk rock glacier thickness at Galena Creek, Wyoming, estimated from 2016, 2019 and 2020 GPR survey data. The location of each map panel is shown on the left side of Figure 2. The diamonds show the locations of the CMP wave speed measurements for these thickness estimates. Map projection: WGS84/UTM 12N.

https://doi.org/10.1017/jog.2022.90 Published online by Cambridge University Press

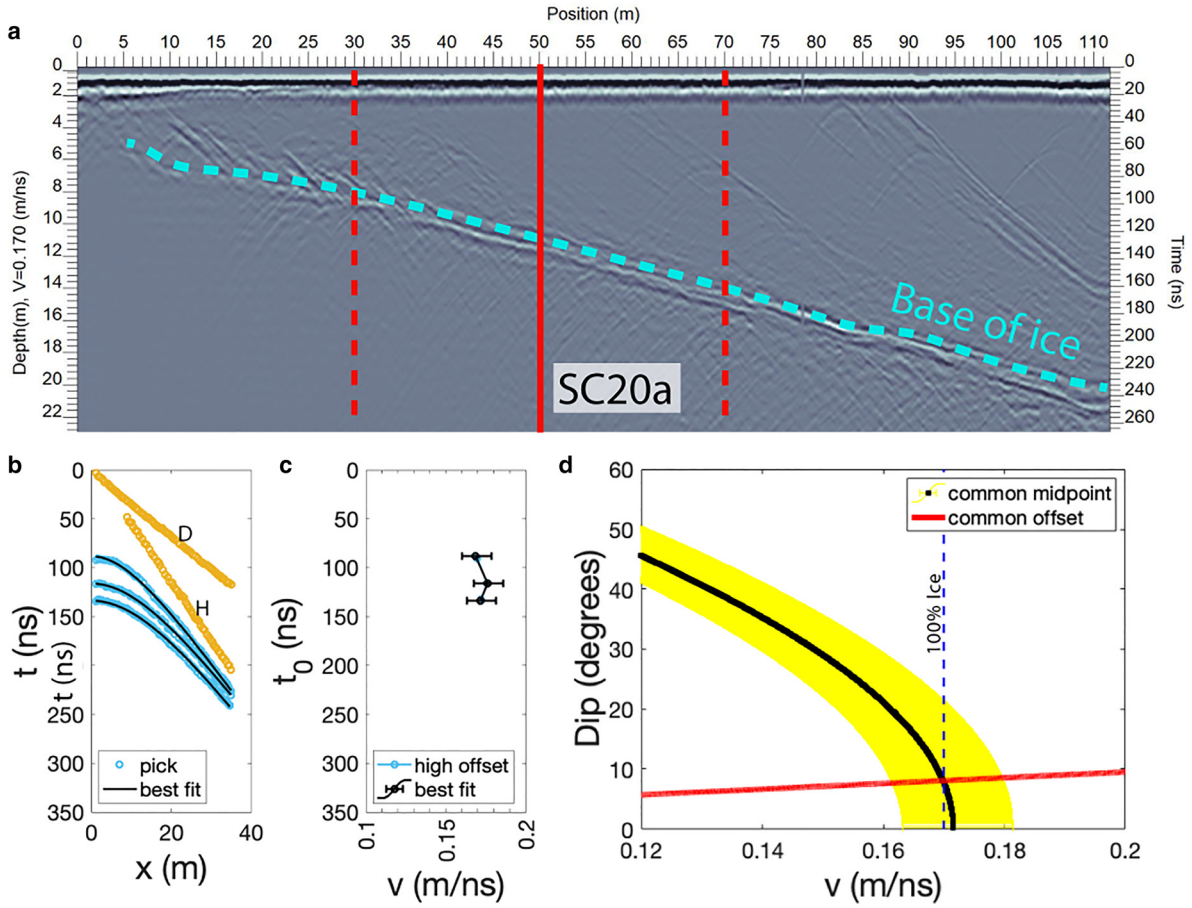

Fig. 12. 100 MHz profile collected at upper Sulphur Creek, Wyoming (SC20a). The wave speed and dipping reflector results are consistent with nearly pure glacial ice. The gold segments in (b) indicate interpreted direct and headwave arrivals in the data, labeled 'D' and 'H', respectively. Here, the wave speed is interpreted as 0.17 m ns^{-1} (d).

an interpreted 17 ns TWTT to the first break of the reflection, the 90 cm interface implies a wave speed of 0.105 m ns^{-1} in the debris layer ($\varepsilon \approx 8$), while a reflection from the 70 cm interface is consistent with a wave speed of 0.08 m ns^{-1} ($\varepsilon \approx 13$). Since the excavated debris section appeared to be located at a point of runoff convergence on the rock glacier and the observed water content was high, we consider that this location may have the slower wave speed and higher dielectric constant, but this is likely a lower bound for generalized debris wave speed, as other locations could have drier debris.

Our 200 MHz CMP survey at Galena Creek and the survey conducted by Petersen and others (2019a) both indicate shallow wave speeds which are lower than that of the deeper measurements of the bulk section, with the lower bounds approaching 0.11 m ns^{-1}. Since these shallow reflectors are not detectable at offsets much greater than their depth, the uncertainty is higher for the shallow CMP-derived wave speeds. If there is an ice-cemented debris layer separating the unconsolidated debris from the glacier ice, such as the layer observed at upper Sulphur Creek, the radar wave may be sampling this sub-wavelength scale layer at the largest detectable offsets, accounting for the slight increase in CMP debris wave speed compared to the direct measurement. For this reason, we take the mid-range value of 0.1 m ns^{-1} ($\varepsilon_{\text{debris}} = 9$) for all of our debris thickness estimates at Gilpin Peak, Galena Creek, Sulphur Creek and Sourdough, assuming a homogeneous dielectric constant for the surface debris layers and englacial lithic inclusions in the bulk dielectric mixing models (Figs 16, 18–20). However, the 100 and 200 MHz CMP winter surveys at Sourdough, AK returned shallow reflections with best fit wave speeds that clearly exceeded the deeper bulk wave speed by more than 1 std dev. (Fig. 6): the shallow reflection's best fit was 0.18 m ns^{-1} with an uncertainty of ~0.015 m ns^{-1}, while the bulk wave speed was measured to be 0.149 m ns^{-1} with an uncertainty of ~0.005 m ns^{-1}, a factor of 3 less than the shallow uncertainty.

The snow depth during GPR data acquisition at Sourdough was less than the lower limit for detection (~1 m) at the GPR frequencies used. Furthermore, the winter temperatures make it likely that the liquid water content of the debris at this time was negligible. Both winter and summer results at the same location on the rock glacier (SP19) indicate a bulk wave speed of ~0.15 m ns^{-1}, with a shallow reflector interpreted to be the debris layer producing an increased wave speed measurement and higher uncertainty relative to those of the basal reflection (Figs 6 and S4). CMP measurements acquired at other locations on the rock glacier in summer 2021 show a similar pattern (Figs S5 and S6), indicating no significant seasonal influence on the wave speed measurement. The apparent increase in wave speed for the Sourdough debris layer may be caused, in part, by the shallow depth of the debris/ice interface relative to the antenna offset needed to measure the change in travel time, leading to imprecise wave speed measurements. Wave speed inflation may also arise from small-scale variations in debris thickness, leading to sloped interfaces with respect to the CMP orientation.

Additionally, the increased debris layer wave speed measurements at Sourdough may also be an artifact from the shallow

https://doi.org/10.1017/jog.2022.90 Published online by Cambridge University Press

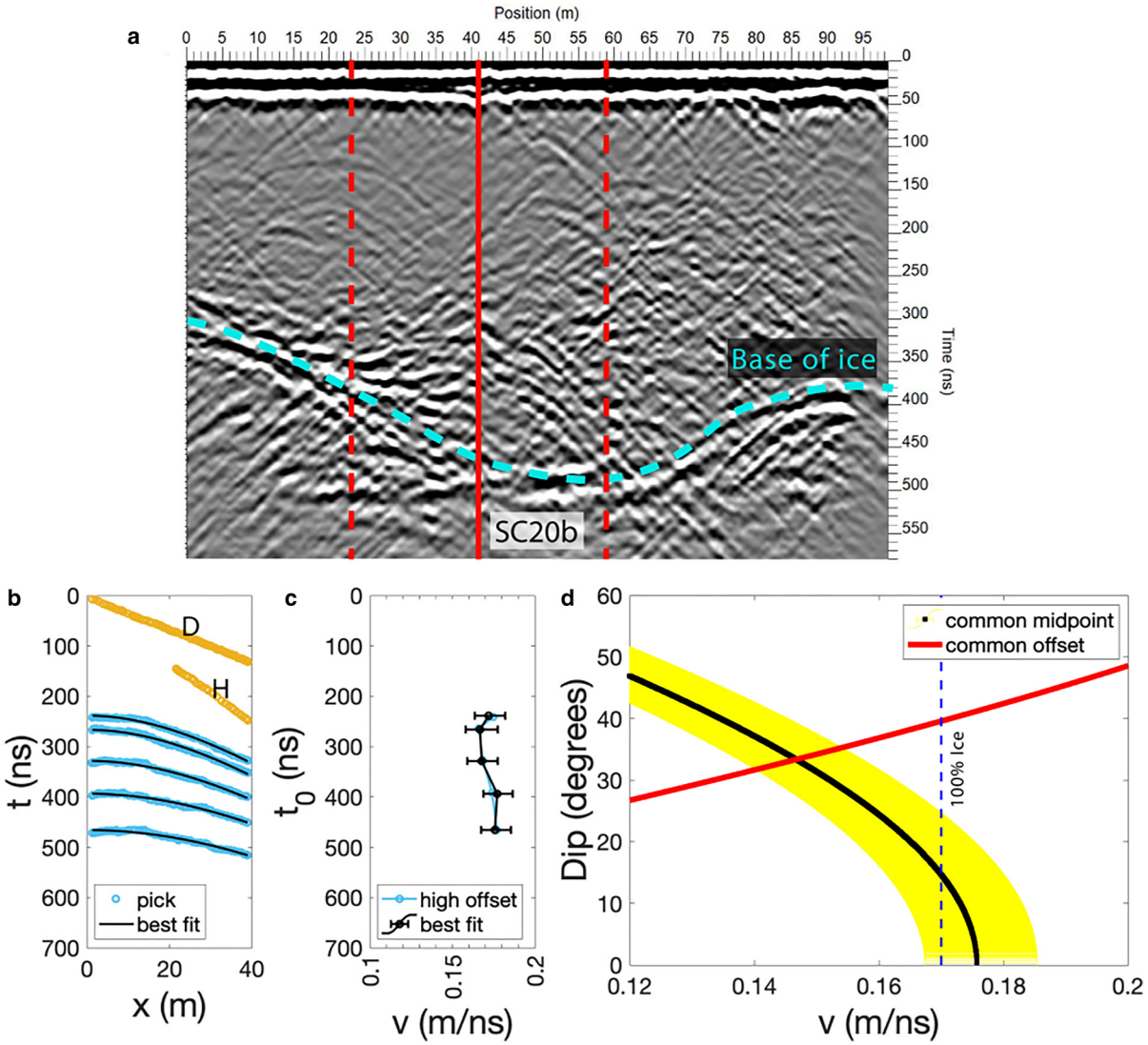

Fig. 13. 50 MHz profile and wave speed analysis results at lower Sulphur Creek, Wyoming (SC20b). After dipping reflector correction, the wave speed value is ~0.147 m ns^{-1}, consistent with that of ice-cemented rock glaciers. The gold segments in (b) indicate interpreted direct and headwave arrivals in the data, labeled 'D' and 'H', respectively. After dipping reflector correction (d), the wave speed is interpreted as 0.147 m ns^{-1}.

reflector interacting with a refracted headwave arrival. Assuming this near-surface arrival is a headwave, which is linear in travel time vs offset and is generated when an underlying medium has a faster wave speed than the overburden layer, the underlying layer's wave speed is ~0.144 m ns^{-1} (Telford and others, 1990). This value is consistent with the bulk rock glacier measurement and the observation of a headwave implies a supraglacial debris layer with a slower wave speed. Due to these ambiguous features in the shallow CMP data, we take all debris layer wave speeds to be 0.1 m ns^{-1}, directly measured by tying the debris excavation thickness with GPR travel time at Sulphur Creek, Wyoming (Fig. 17). This wave speed corresponds to a dielectric constant of 9. We note that the heterogeneity of dielectric properties in the debris layer remains a primary source of uncertainty in GPR estimations of local debris layer wave speed, thickness and bulk ice fraction. Surveys on Ngozumpa Glacier, Nepal, measured debris wave speeds exceeding 0.15 m ns^{-1} using a depth/travel time tie (Nicholson and others, 2018). CMP measurements of the debris wave speed on Lirung Glacier, Nepal, ranged from 0.106 to 0.129 m ns^{-1}, with the lowest values appearing to correlate with the flattest reflectors (McCarthy and others, 2017). For simplicity, we assume a constant value of 0.1 m ns^{-1} for the debris layer at all of our study sites based on our excavation/GPR tie point at upper Sulphur Creek. Further characterization of the variability of dielectric properties of supraglacial debris could help refine these estimations.

Our assumption of 0.1 m ns^{-1} for the debris wave speed produces GPR-derived thickness measurements which reveal trends among our study sites. In general, the debris thickness is greater for the ice-cemented zones and lower portions of the rock glaciers (>2 m for Sourdough, Gilpin Peak and lower Sulphur Creek, where the maximum ice fraction is <75%) than the ice-cored regions (0.2–1 m for Galena Creek and upper Sulphur Creek, where ice fraction is >0.8). Additionally, both the ice-cemented and ice-cored zones show undulations in debris thickness correlating with the spatial scale of the furrow and ridge morphology (Figs 16, 18–20). This is consistent with observations of compressive buckle folding in the debris layer (Frehner and others, 2015). Some very thick debris measurements may be related to the intersection of internal debris layers with the surface, such as upper Galena Creek (Fig. 19a). These thickness variability observations will constrain thermal effects of the debris layer on the subsurface ice while informing models of debris layer processes and their relationships with rock glacier dynamics and internal structure.

https://doi.org/10.1017/jog.2022.90 Published online by Cambridge University Press

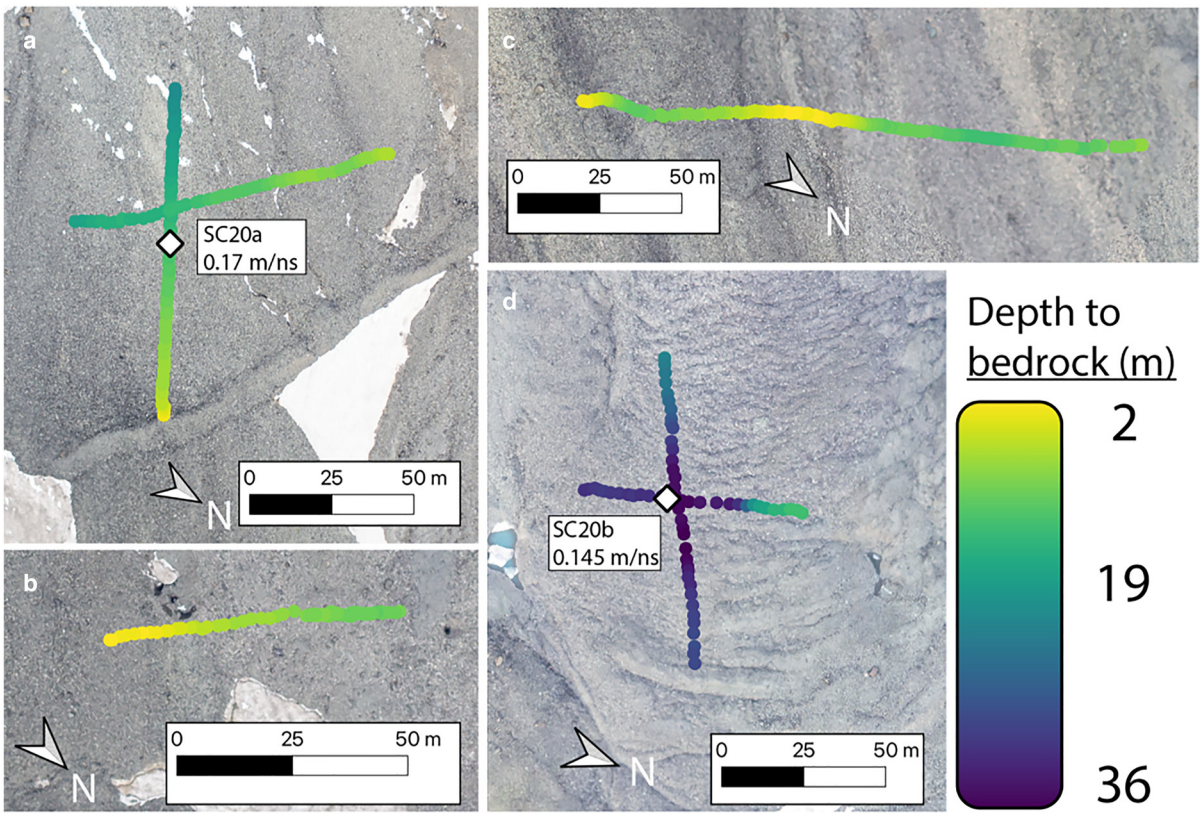

Fig. 14. Bulk rock glacier thickness at Sulphur Creek, Wyoming, estimated from 2019 and 2020 GPR survey data. The location of each map panel is shown on the right side of Figure 2. The diamonds show the locations of the CMP wave speed measurements for these thickness estimates. Map projection: WGS84/UTM 12N.

4. Discussion

4.1. Comparison with previous Gilpin Peak results

In addition to the data we collected at our field sites from 2018 to 2021, we used our least squares analysis method to process a digital interpretation of a 25 MHz CMP survey acquired in a previous study at Gilpin Peak, Colorado (Degenhardt and others, 2003; labeled D+03 in Fig. 21). We find that the bulk wave speed above a near-surface reflector where $t_0 = 127$ ns agrees with the 2003 interpreted wave speed of 0.12 m ns^{-1} with a detectable signal up to ~15 m offset. In the 2003 automated wave speed analysis, the shallow high-likelihood region is centered at ~0.12 m ns^{-1} down to 100 ns. We suggest that this value corresponds to our shallow 0.12 m ns^{-1} result, and this region is the source of the interpretation for best-fit bulk wave speed presented by Degenhardt and others (2003). However, deeper hyperbolas are evident in the D+03 data; we picked three additional horizons with t_0 values of 176, 300 and 364 ns in the 25 MHz plot. All of these horizons fit wave speeds of 0.14 m ns^{-1} with uncertainties of ⩽0.01 m ns^{-1}. Since each CMP horizon contains information about the wave speed of the overlying bulk material, the average wave speed of the sounding column will be associated with the deepest reflector, not the strongest. The 0.14 m ns^{-1} result is consistent with a weaker but consistent band of increased likelihood in the D+03 wave speed plot ranging from ~150 to 400 ns (Fig. 21c) that was ignored in the original interpretation of bulk wave speed; the width of this 0.14 m ns^{-1} band is also comparable with the derived uncertainty value near 0.01 m ns^{-1}. The deeper reflectors may appear to have lower amplitudes in the automated analysis due to the algorithm's reliance on iterative stacking and constructive interference. We postulate that the automated method amplifies the stronger shallow reflections disproportionally to the relatively attenuated reflections at depth, and this bias toward a shallow signal led to the interpretation of a bulk wave speed of 0.12 m ns^{-1} in the previous study.

We argue that our manual interpretation and fitting method, which considers wave speed solely as a function of CMP geometry with no dependence on received power, provides a more robust wave speed upper bound of 0.14 m ns^{-1} rather than the previously reported 0.12 m ns^{-1}. The 0.14 m ns^{-1} wave speed is also consistent with the dip-corrected results of our GP19 survey analysis. The 2003 common offset radargram indicated nearly horizontal reflectors close to the 2003 CMP location (Degenhardt and others, 2003), so we assume that there was negligible error due to the representation of dipping reflectors in their data. A ~15% increase in estimated bulk wave speed may seem relatively insignificant, but it leads to an increase of up to ~7 m in bulk rock glacier thickness from the interpreted 2003 data (Fig. 21a). However, if we assume relative dielectric permittivities of 3 for pure ice and 9 for lithics, this 0.02 m ns^{-1} increase in wave speed corresponds to an increase in local ice volume fraction from ~30 to ~60% in the two-phase mixing models (see Section 4.2). These results could significantly impact estimates of integrated rock glacier ice storage in the San Juan Mountains, and it demonstrates the sensitivity of rock glacier ice fraction estimations to the accuracy of the wave speed measurement. In consideration of the sensitivity of dielectric constant on bulk wave speed, we will discuss why an accurate and precise wave speed measurement is essential for estimating ice fraction.

4.2. Wave speed and composition

Our analyses for all sites returned GPR wave speeds consistent with ice fractions >50%, when assuming a dielectric constant of 3 for ice and 9 for rock (Table 2 and Fig. S7). The two Wyoming sites displayed evidence of clean, glacially derived ice

https://doi.org/10.1017/jog.2022.90 Published online by Cambridge University Press

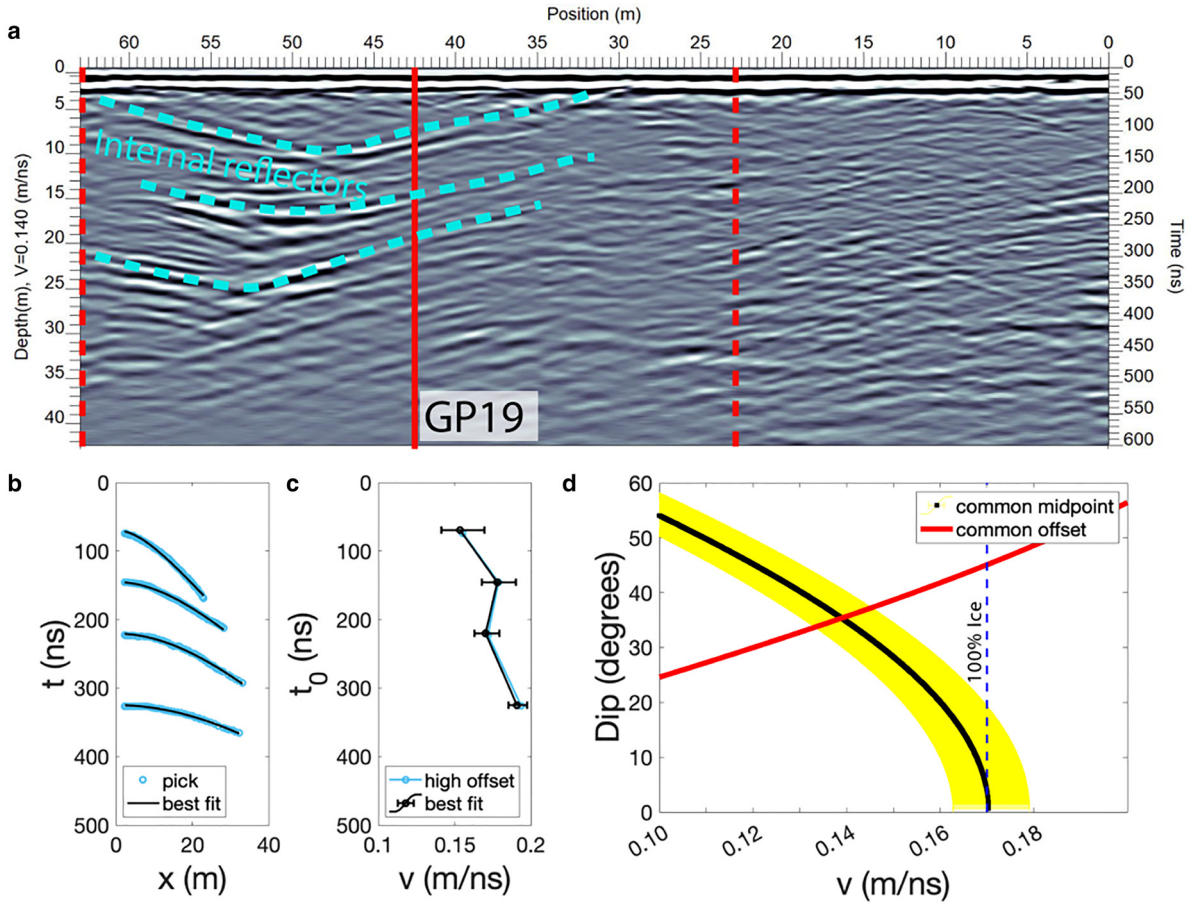

Fig. 15. 50 MHz survey at Gilpin Peak, CO with interpreted horizons (blue) and CMP section location (GP19). The steep reflectors explain the unexpectedly high apparent wave speeds, and after reflector dip correction (d) the wave speed is estimated to be ~0.14 m ns^{-1}.

units buried by debris on the upper portions of each rock glacier, with generally decreasing ice content toward the glacier toe. The dielectric constant of the debris inclusions is a source of uncertainty for these estimates: lower permittivities for lithics would lead to lower volumetric ice fractions for a given bulk wave speed, so these estimates should be considered an upper bound on ice content. Other uncertainty sources in our wave speed estimates include errors associated with manual interpretation and assumptions of geometric simplicity (smooth, continuous and linear interfaces relative to radar wavelength). Investigation into the effects of rough or nonhomogeneous reflectors could further account for wave speed uncertainties.

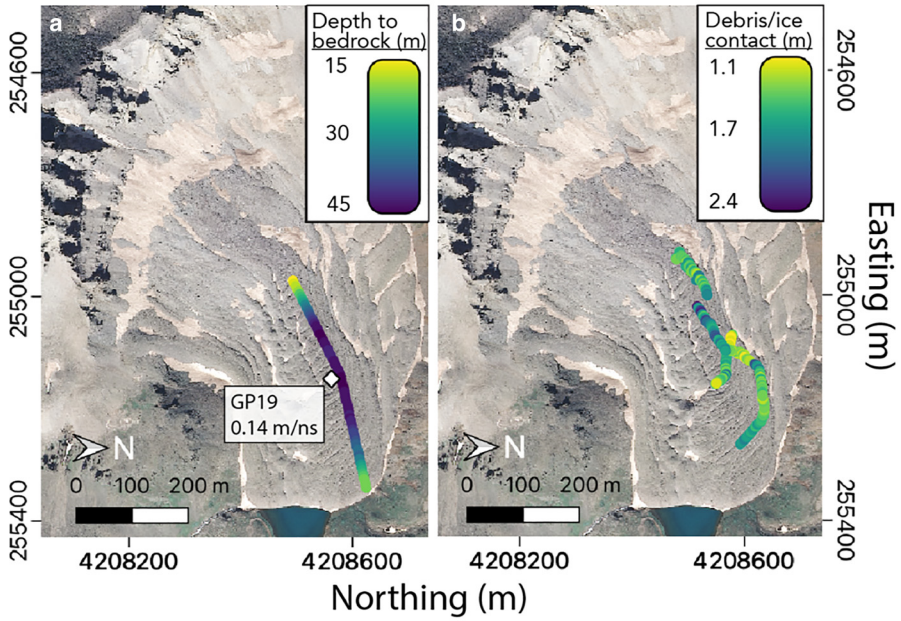

Fig. 16. Gilpin Peak, Colorado: (a) map of rock glacier thickness derived from the 25 MHz GPR travel times of Degenhardt and others (2003), using an updated bulk wave speed of 0.14 m ns^{-1}. The diamond shows the location of the 2019 CMP wave speed measurement (50 MHz; see Fig. 15), which is within ~100 m of the 2003 CMP and agrees with the reprocessed results. (b) Debris thickness map using the 100 and 200 MHz 2019 GPR data assuming a debris wave speed of 0.1 m ns^{-1} (see Section 3.5). Map projection: WGS84/UTM 13N.

https://doi.org/10.1017/jog.2022.90 Published online by Cambridge University Press

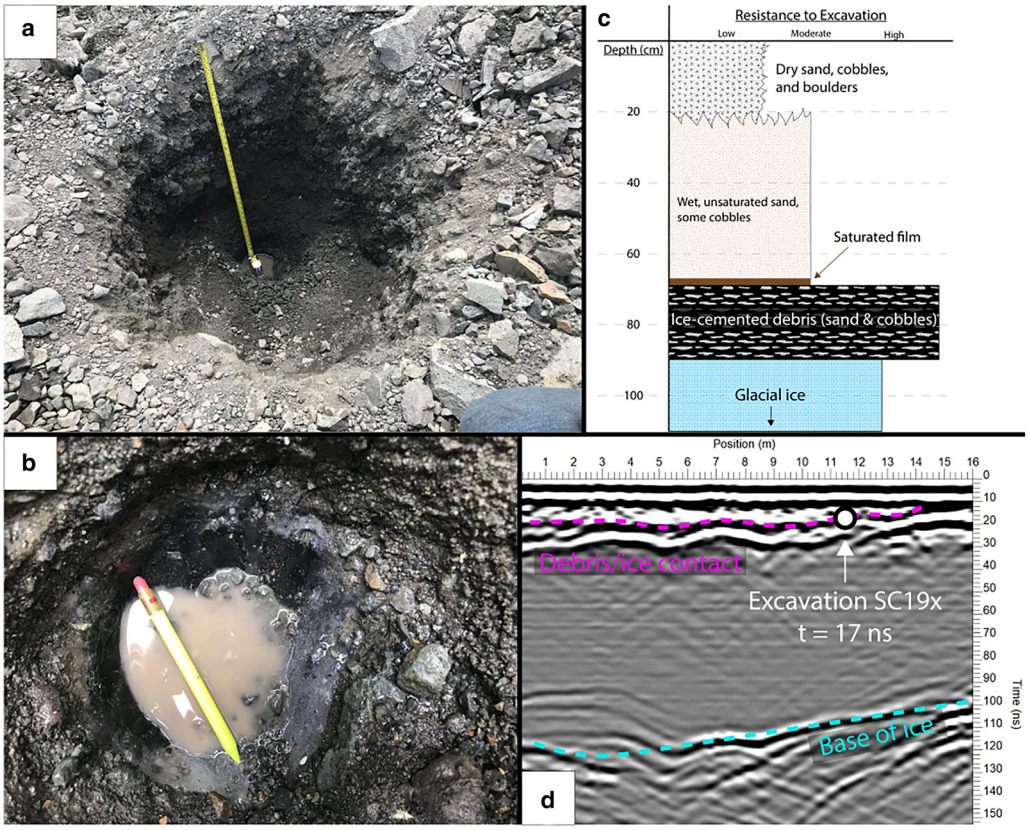

Fig. 17. Observations for surface debris wave speed experiment. (a) Context view of full ~1 m excavation in the debris. (b) Close-up of the debris–ice contact at the base of the excavation. Note the accumulation of water seeping from the thin saturated film at the top of the ice. (c) Stratigraphic observations of the debris layer and debris–ice contact overlying clean ice interpreted to be of glacial origin. (d) 200 MHz GPR profile and interpretation at the location of the excavation (white circle, corresponding with excavation location in Fig. 18).

An important result of our analysis is the demonstration that dipping subsurface reflectors may lead to overestimates of bulk wave speeds with the CMP method, which has consequences for depth corrections and compositional models. Since the wave speed in rock glaciers is very sensitive to volumetric ice fraction, and several rock glacier surveys have revealed the presence of subsurface dipping reflectors, we argue that it is essential to consider the dip angle of the reflector when estimating the wave speed, especially when the dip exceeds ~10° relative to the surface. Above this 10° threshold, the deviation from the true wave speed begins to exceed the uncertainty in the measurements, so we suggest that all future rock glacier surveys correct for reflector dip when using CMP wave speed analysis. Indeed, any geologic target with dipping subsurface structures should use the techniques employed in this paper for accurate CMP wave speed analysis. Dipping reflectors influenced the apparent wave speed at Galena Creek, Sulphur Creek and Gilpin Peak. Accounting for dipping reflectors ensures that wave speeds remain physically possible (not exceeding 0.17 m ns^{-1}, such as measurements at upper Galena and Sulphur Creek), and it can also help to prevent overestimates in ice content where the rock glacier contains less ice (e.g. Gilpin Peak and lower Sulphur Creek).

The CMP survey at Sourdough, Alaska had no steeply dipping reflectors influencing the wave speed measurement and returned a value of 0.149 m ns^{-1} for each frequency at this location. This wave speed is consistent with an ice fraction of ~75%, but it does not conclusively delineate whether the ice is glacigenic or periglacial in origin. Since this value is on the lower end of our wave speed results and no exposures of high-purity glacial ice were observed at this location, it may lend support to the periglacial interpretation. However, this measurement was acquired near the lowest elevation on the rock glacier where the bulk glacier thickness is relatively low and the debris layer is relatively thick, so it is possible that ice fraction increases with increasing elevation at Sourdough. Additional CMP measurements toward the head of the rock glacier would help elucidate this possibility. In general, our results of >50% bulk ice fraction, debris layer thicknesses of a few meters and a maximum rock glacier thickness >50 m are comparable with previous observations at nearby Fireweed Rock Glacier, which is ~20 km away (Elconin and LaChapelle, 1997; Bucki and others, 2004). Additional GPR surveys at Sourdough could reveal spatial trends in ice fraction along the profile of the rock glacier while improving the thickness measurements mapped in Figure 7, which would provide more information about the relationship between its internal structure and formation processes.

At Galena Creek, Wyoming, one question arises from the results: what causes the slight increase in measured bulk wave speed and ice fractions at CMP locations moving down-glacier from the cirque to the trunk? This is counterintuitive when considering the tendency of ice accumulation to increase with elevation. Perhaps the highest surveys near the cirque head, which measured an average wave speed of ~0.16 m ns^{-1} (Fig. S8) and detected several closely spaced internal reflectors (Petersen and others, 2019a; labeled GC16 in Fig. 11), sampled a location with a higher debris content due to its proximity to the headwall/glacier margin and the resulting process of debris-facilitated ice accumulation. The lower surveys may have been conducted over a thicker portion of the preserved glacial ice unit, leading to a higher bulk ice content and a measured wave speed of ~0.168

https://doi.org/10.1017/jog.2022.90 Published online by Cambridge University Press

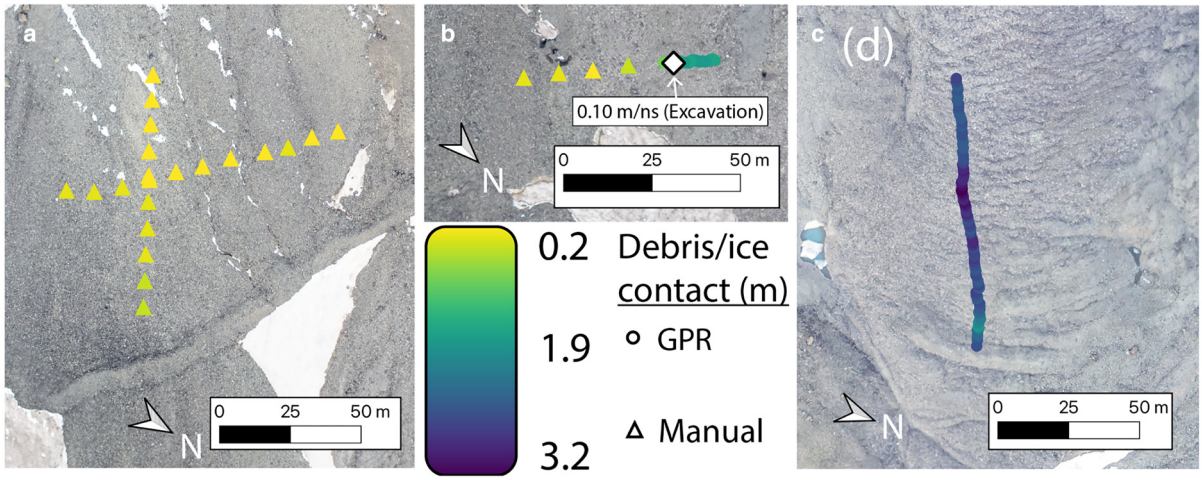

Fig. 18. Debris thickness at Sulphur Creek, Wyoming, measured directly through debris pits (⩽90 cm depth, marked as triangles) and GPR interpretation (⩾90 cm depth, marked as points). The white diamond shows the location where a manual thickness measurement was tied to a GPR reflector at 90 cm depth, resulting in the wave speed used for all rock glacier debris thickness measurements in this study (see Fig. 17). Panel locations are shown in the Sulphur Creek map in Figure 2 (note: debris thickness was not measured in panel 'c' in the Sulphur Creek context map, therefore panel 'c' in this figure corresponds with the region labeled 'd' on the Sulphur Creek map in Fig. 2). Map projection: WGS84/UTM 12N.

m ns^{-1}. However, the magnitudes of the uncertainties of these measurements still allow for this disparity to be smaller than the best fit values suggest, and it is likely that there is significant compositional heterogeneity within each rock glacier.

Other observations of the GPR data from Galena and Sulphur Creek support a high-purity ice core of glacial origin buried beneath the supraglacial debris at higher elevations for both sites. First, several diffraction hyperbolas are observed in the common offset profiles. These hyperbolas fit to wave speeds ranging from ~0.1 to 0.17 m ns^{-1} and often appear asymmetric, which is consistent with the presence of pure ice and small-scale compositional heterogeneity in the rock glaciers. The few dielectric constant measurements exceeding 10 may correspond to zones of meltwater-saturated debris near the surface. There appears to be a general trend of decreasing diffraction wave speeds (thus increasing dielectric constant, Fig. S9) moving down-glacier for both Galena and Sulphur Creek, further supporting the hypothesis of a high bulk ice fraction in their upper cirques which transitions to lower ice concentrations at lower elevations.

In addition to diffraction hyperbolas in the common offset sections, there is a distinct headwave arrival in the CMP data for some common midpoints on both Galena and Sulphur Creek (labeled 'H' in Figs 8, 9, 12 and 13; example data in Fig. S10). This is interpreted as the arrival that is generated from the refraction of the radio wave as it transmits from the lower-velocity debris to the higher-velocity ice-rich medium. Since this wavefront is linear in time and offset, the slope of the headwave arrival is the reciprocal of the wave speed of the higher-velocity medium (Telford and others, 1990). The headwaves observed in our data fit wave speeds of ~0.17 m ns^{-1}, further supporting the existence of a nearly pure ice core buried beneath the debris at these locations. Uncertainty analyses were not performed for the common offset hyperbolas or CMP headwave arrivals, but their overall trends support the results of the CMP wave speed analysis, indicating a high-elevation ice core and a decrease in ice content moving down glacier at Galena and Sulphur Creek, Wyoming. This may signify a transition from an ice core of glacial origin to a periglacial ice-cemented rock glacier with decreasing elevation at both of these sites. The correlation of the GPR wave speeds, surficial ice exposure observations and borehole data (Clark and others, 1996; Potter and others, 1998; Steig and others, 1998) at Galena and Sulphur Creek support the interpretation that rock glaciers with a dip-corrected wave speed between

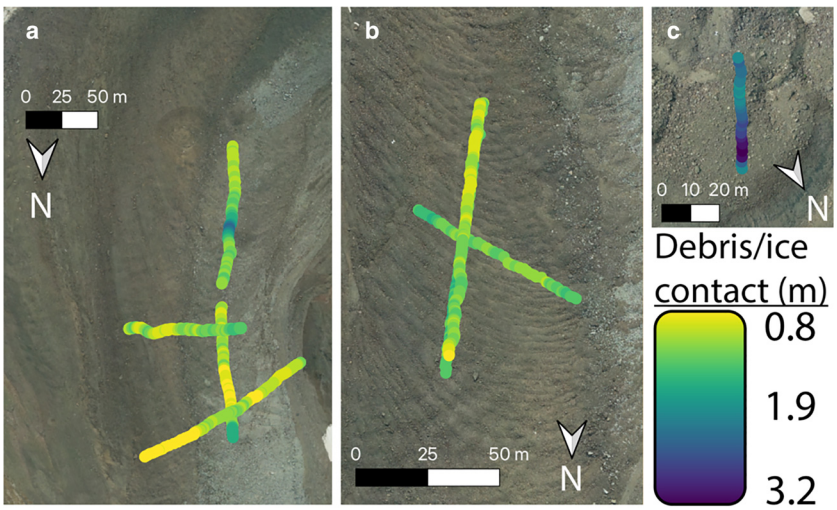

Fig. 19. Debris thickness measurements at Galena Creek, Wyoming, using a constant wave speed of 0.1 m ns^{-1}. Panel locations are shown in Galena Creek map in Figure 2. Map projection: WGS84/UTM 12N.

https://doi.org/10.1017/jog.2022.90 Published online by Cambridge University Press

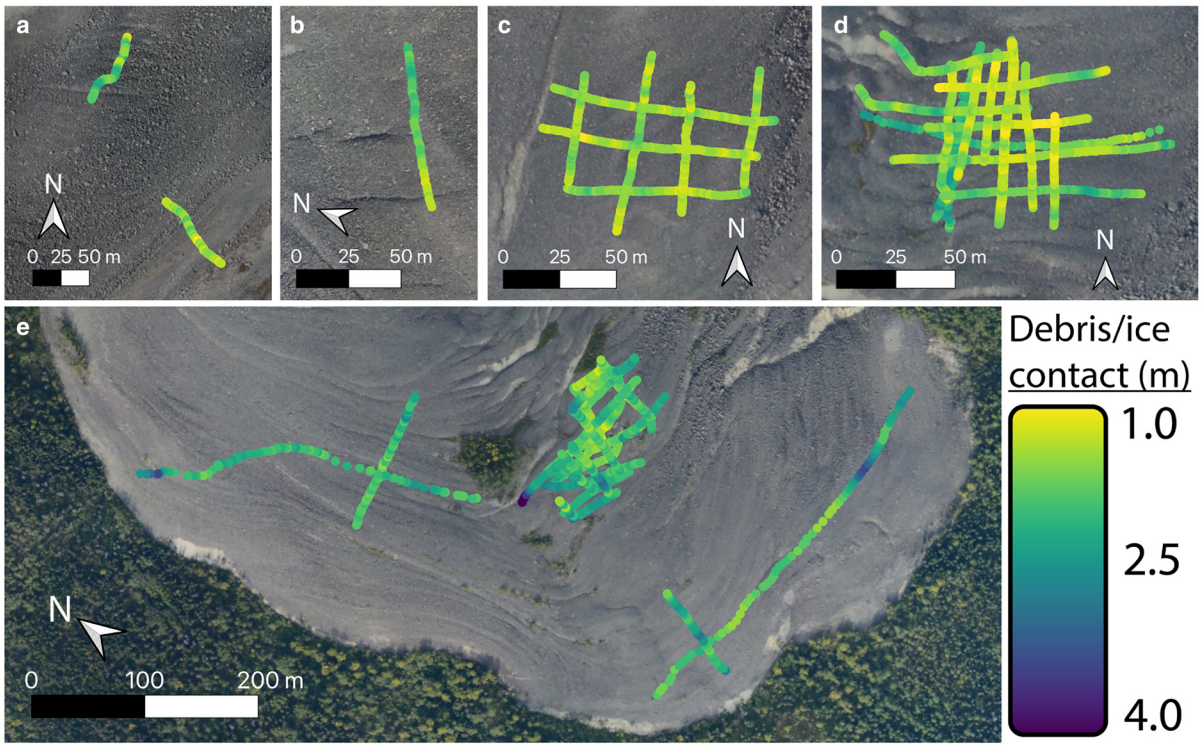

Fig. 20. Depth to the debris/ice contact from 100 and 200 MHz GPR surveys on Sourdough Rock Glacier, assuming a debris layer wave speed of 0.1 m ns^{-1}. The location of each panel is shown in Figure 1. Map projection: WGS84/UTM 7N.

0.16 and 0.17 m ns^{-1} likely have a high-purity ice core of glacial origin.

This study and many previous authors have demonstrated the heterogeneity in GPR reflector geometry and wave speed structure of rock glaciers around the Earth (Table 1). When dipping reflectors are present, a significant challenge in accounting for apparent wave speed inflation is the uncertainty in the orientation of the CMP survey in relation to the common-offset profile, since the error in wave speed is related to the apparent dip of the subsurface reflector observed from the CMP orientation with respect to the true strike and dip of the reflector. Relatively few of the publications referenced in Table 1 provide

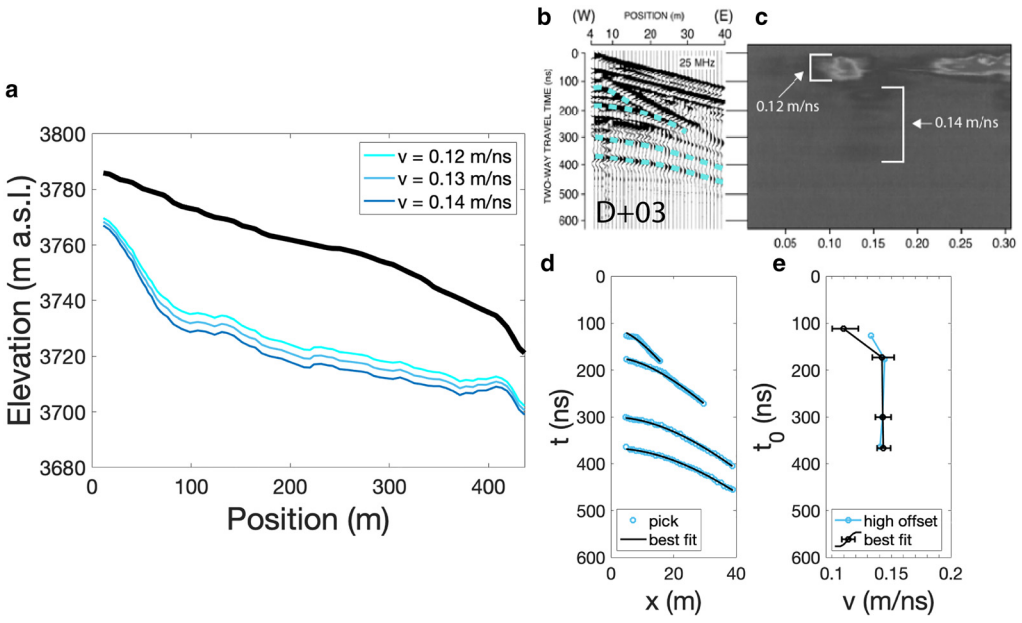

Fig. 21. Re-analysis of 25 MHz survey collected by Degenhardt and others showing that the bulk radio wave speed through the rock glacier has a best fit of ~0.14 m ns^{-1}. (a) Rock glacier thickness and basal elevation depth corrected from Degenhardt and others (2003), using wave speeds of 0.12, 0.13 and 0.14 m ns^{-1}. (b) 2003 CMP data (Degenhardt and other, 2003) annotated with our manual interpretations as blue dashed lines. (c) Semblance plot, modified from Figure 4a of Degenhardt and others (2003) to depict the digital interpretations in the CMP section and the interpreted wave speed values in the semblance plot. Degenhardt and others (2003) noted the 0.12 m ns^{-1} signal in their analysis, but neglected the deeper, less obvious signal centered ~0.14 m ns^{-1} that is more representative of the bulk interior of the rock glacier. (d) Best fit hyperbola for each interpreted horizon. (e) Best fit wave speeds with their uncertainties, showing a trend with depth that is similar to that observed in the semblance plot in (b).

https://doi.org/10.1017/jog.2022.90 Published online by Cambridge University Press

survey orientations, data, analysis details or assumptions for their wave speed estimates.

Our experiment examining the effects of dipping reflectors on estimated wave speed shows the importance in accounting for internal structure and reflector geometry in rock glacier GPR wave speed estimations. Otherwise, it could result in inaccuracies propagated to assessments of individual rock glacier geometry and sums of local to global ice volumes preserved beneath debris. For example, Jones and others (2018a) estimated an ice mass of 83.72 ± 16.74 Gt stored in the global rock glacier population using an assumed range of 40–60% volumetric ice fraction, but this global ice mass could be greater if a significant percentage of rock glaciers contain glacial ice cores with bulk ice fractions much >60%. Precise compositional measurements over a range of sites could further reduce the uncertainty of the global estimate, while also elucidating the relative importance of rock glaciers, debris-covered glaciers and bare ice glaciers in different hydrological systems (e.g. Himalayan vs Andean glacier populations; Jones and others, 2018b).

We reiterate that our assumption of a dielectric constant of 9 for the lithic inclusions remains a primary source of uncertainty in calculating the ice fraction with dielectric mixing models using bulk wave speed. Better characterization of the intra- and inter-site variability in the dielectric properties of the debris could further refine estimates of both debris thickness and bulk ice fraction. More work is needed to understand the effects of local lithology and mineralogy on the dielectric properties and thermal insulation of the debris layer and the broader effects on rock glacier dynamics. For future surveys measuring radio wave speed on rock glaciers using the CMP method, we recommend a standard method of collecting common-offset transects to associate with each CMP orientation and assess the reflector geometry for the wave speed estimate. This replicable method will improve the precision of compositional and geometric measurements for rock glaciers, and these measurements can be applied to dynamic viscoelastic flow models for comparison with photogrammetrically derived surface displacements to better understand rock glacier formation and evolution.

5. Conclusion

When using GPR in a common midpoint configuration to measure the structure and composition of any geophysical target with subsurface reflectors dipping ~10° relative to the surface, it is important to collect co-located and coeval common offset profiles to determine the influence of reflector geometry on estimated wave speed. This is especially true if the target deforms over the course of a multi-year field campaign where it may be impractical or impossible to replicate the position and acquisition parameters of a previous year's measurement. Increased reflector dip and complexity generally increases the uncertainty of the measurements, so future surveys that target continuous, flat reflectors while considering the small-scale compositional heterogeneity throughout each site may best characterize the dielectric properties of rock glaciers and their overlying debris. The accuracy and precision of wave speed measurements directly impact compositional estimates through dielectric mixing models while also affecting depth corrections of GPR travel time data. We have shown an example of this procedure used to characterize rock glacier composition and geometry. These compositional estimates of individual rock glaciers will have a significant impact when extrapolated to total ice volume of regional or global rock glacier populations, which subsequently affects our understanding of alpine hydrological systems.

We used our method of geometrically corrected wave speed measurement to estimate the bulk composition on four rock glaciers over a range of latitudes, elevations and geographic settings. Our results included the detection of nearly pure ice cores at upper Galena and Sulphur Creek, Wyoming, consistent with previous results at Galena Creek (Potter and others, 1998; Petersen and others, 2019a). We also measured lower volumetric ice fractions of ~60–70% at Gilpin Peak, Colorado, and Sourdough, Alaska. These compositional results may be affected by the uncertainty in the dielectric permittivity of the lithic inclusions within each rock glacier, but our analysis shows that the ice fraction at the Gilpin Peak site could be twice as much as previous estimates of 30%. Understanding the compositional trends of ice-cored and ice-cemented rock glaciers will help the cryospheric community decipher the formation mechanisms and ice origins at different sites, which will further improve our generalized models for rock glacier evolution.

We also examined the wave speed within the surface debris layer. Our best determination for the dielectric constant of the debris layer is ~9, although these shallow measurements have a relatively high uncertainty throughout all of the field sites. Further constraints on the dielectric properties of the debris will improve estimates of bulk rock glacier composition through dielectric mixing models. Our measured bulk and debris layer wave speeds were used to convert GPR travel time measurements into depth to bedrock and debris layer thickness estimates. These compositional and geometric observations will inform future models of rock glacier flow and ice/rock dynamics in terrestrial and planetary settings.

Supplementary material. The supplementary material for this article can be found at https://doi.org/10.1017/jog.2022.90

Data. All data and associated Supplementary materials reported in this paper are openly available online at https://doi.org/10.25422/azu.data.19495178.

Acknowledgements. This study was funded by NASA Solar System Workings grant 80NSSC19K0561. We thank Michael Christoffersen, Brandon Tober, Stefano Nerozzi, Tyler Kuehn, Victor Devaux-Chupin, Cassie Stuurman, Ben Cardenas and Joe Levy for their assistance and advice with field data acquisition. We thank two anonymous reviewers for their constructive comments that improved the manuscript. Additionally, Eric Yould and Kurt Smith provided essential logistical support for rock glacier access in Alaska. Chris Larsen acquired the aerial imagery for the Sourdough base map, Chris Boyer acquired the aerial imagery for the Galena Creek and Sulphur Creek base maps and the Gilpin Peak base map was downloaded from the public USGS aerial imagery database.

Author contributions. TM collected the GPR data, developed the CMP analysis code, performed the wave speed/dipping reflector analysis, calculated the composition of each rock glacier and wrote the manuscript. EP collected the GPR data, performed the diffraction hyperbola analysis, provided interpretations for the results and contributed to the revision of the manuscript. JH acquired funding, provided logistical support for data collection, supervised the data analysis and contributed to the revision of the manuscript.

References

Anderson RS, Anderson LS, Armstrong WH, Rossi MW and Crump SE (2018) Glaciation of alpine valleys: the glacier–debris-covered glacier–rock glacier continuum. *Geomorphology* **311**, 127–142. doi: 10.1016/j.geomorph.2018.03.015

Anderson LS, Armstrong WH, Anderson RS, Scherler D and Petersen EI (2021) The causes of debris-covered glacier thinning: evidence for the importance of ice dynamics from Kennicott Glacier, Alaska. *Frontiers in Earth Science* **9**, 680995. doi: 10.3389/feart.2021.680995

Baker DMH and Carter LM (2019) Probing supraglacial debris on Mars 1: sources, thickness, and stratigraphy. *Icarus* **319**, 745–769. doi: 10.1016/j.icarus.2018.09.001

Barsch D (1987) The problem of the ice-cored rock glacier. In Giardino JR Shroder Jr. JE and Vitek JD eds. *Rock Glaciers*. Boston, MA: Allen & Unwin, 45–53.

Berthling I, Etzelmüller B, Isaksen K and Sollid JL (2000) Rock glaciers on Prins Karls Forland. II: GPR soundings and the development of internal structures. *Permafrost and Periglacial Processes* **11**, 357–369. doi: 10.1002/1099-1530(200012)11:4<357::AID-PPP366>3.0.CO;2-6

Bucki AK, Echelmeyer KA and MacInnes S (2004) The thickness and internal structure of Fireweed Rock Glacier, Alaska, U.S.A., as determined by geophysical methods. *Journal of Glaciology* **50**(168), 67–75. doi: 10.3189/172756504781830196

Campbell MJ and Ulrichs J (1969) Electrical properties of rocks and their significance for lunar radar observations. *Journal of Geophysical Research* **74**, 5867–5881. doi: 10.1029/JB074i025p05867

Clark DH and 5 others (1996) Old ice in rock glaciers may provide long-term climate records. *Eos, Transactions American Geophysical Union* **77**, 217–222. doi: 10.1029/96EO00149

Cuffey KM and Paterson WSB (2010) *The Physics of Glaciers*, 4th Edn. Oxford: Butterworth-Heinemann.

Degenhardt JJ and Giardino JR (2003) Subsurface investigation of a rock glacier using ground-penetrating radar: implications for locating stored water on Mars. *Journal of Geophysical Research: Planets* **108**(E4), 8036. doi: 10.1029/2002JE001888.

Degenhardt JJ, Giardino JR and Junck MB (2003) GPR survey of a lobate rock glacier in Yankee Boy Basin, Colorado, USA. *Geological Society, London, Special Publications* **211**, 167–179. doi: 10.1144/GSL.SP.2001.211.01.14

Elconin RF and LaChapelle ER (1997) Flow and internal structure of a rock glacier. *Journal of Glaciology* **43**(144), 238–244. doi: 10.3189/S002214300000318X

Florentine C, Skidmore M, Speece M, Link C and Shaw CA (2014) Geophysical analysis of transverse ridges and internal structure at Lone Peak Rock Glacier, Big Sky, Montana, USA. *Journal of Glaciology* **60** (221), 453–462. doi: 10.3189/2014JoG13J160

Frehner M, Ling AHM and Gärtner-Roer I (2015) Furrow-and-ridge morphology on rockglaciers explained by gravity-driven buckle folding: a case study from the Murtèl Rockglacier (Switzerland). *Permafrost and Periglacial Processes* **26**(1), 57–66. doi: 10.1002/ppp.1831

Fukui K and 5 others (2008) Dynamics and GPR stratigraphy of a polar rock glacier on James Ross Island, Antarctic Peninsula. *Journal of Glaciology* **54** (186), 445–451.

Giardino JR and Vitek JD (1988) Interpreting the internal fabric of a rock glacier. *Geografiska Annaler. Series A, Physical Geography* **70**, 15–25.

Isaksen K, Ødegård RS, Eiken T and Sollid JL (2000) Composition, flow and development of two tongue-shaped rock glaciers in the permafrost of Svalbard. *Permafrost and Periglacial Processes* **11**, 241–257.

Jones DB and 5 others (2018b) The distribution and hydrological significance of rock glaciers in the Nepalese Himalaya. *Global and Planetary Change* **160**, 123–142. doi: 10.1016/j.gloplacha.2017.11.005

Jones DB, Harrison S, Anderson K and Betts RA (2018a) Mountain rock glaciers contain globally significant water stores. *Scientific Reports* **8**(1), 2834. doi: 10.1038/s41598-018-21244-w.

Jorgensen WR (2007) *A Validation of Ground Penetrating Radar for Reconstructing the Internal Structure of a Rock Glacier*. Mount Mestas, Colorado, USA (M.S.): Texas A&M University.

Knight R and Endres A (1990) A new concept in modeling the dielectric response of sandstones: defining a wetted rock and bulk water system. *Geophysics* **55**(5), 586–594. doi: 10.1190/1.1442870

Lehmann F and Green AG (2000) Topographic migration of georadar data: implications for acquisition and processing. *Geophysics* **65**, 836–848. doi: 10.1190/1.1444781

Leonard EM (1984) Late Pleistocene equilibrium-line altitudes and modern snow accumulation patterns, San Juan Mountains, Colorado, U.S.A. *Arctic and Alpine Research* **16**(1), 65–76. doi: 10.2307/1551173

Levy JS and 11 others (2021) Surface boulder banding indicates Martian debris-covered glaciers formed over multiple glaciations. *Proceedings of the National Academy of Sciences of the United States of America* **118**, e2015971118. doi: 10.1073/pnas.2015971118

Levy JS, Fassett CI, Head JW, Schwartz C and Watters JL (2014) Sequestered glacial ice contribution to the global Martian water budget: geometric constraints on the volume of remnant, midlatitude debris-covered glaciers: buried Martian glaciers. *Journal of Geophysical Research: Planet* **119**, 2188–2196. doi: 10.1002/2014JE004685

Mackay SL and Marchant DR (2017) Obliquity-paced climate change recorded in Antarctic debris-covered glaciers. *Nature Communications* **8**, 14194. doi: 10.1038/ncomms14194

Mackay SL, Marchant DR, Lamp JL and Head JW (2014) Cold-based debris-covered glaciers: evaluating their potential as climate archives through studies of ground-penetrating radar and surface morphology: cold-based debris-covered glaciers. *Journal of Geophysical Research: Earth Surface* **119**, 2505–2540. doi: 10.1002/2014JF003178

MacKevett EM (1978) Geologic map of the McCarthy Quadrangle, Alaska: U.S. Geological Survey Miscellaneous Investigations Series Map 1032, 1 sheet, scale 1:250,000. doi: 10.3133/i1032

Matsuoka T, Fujita S and Mae S (1997) Dielectric properties of ice containing ionic impurities at microwave frequencies. *Journal of Physical Chemistry B* **101**, 6219–6222. doi: 10.1021/jp9631590

Maurer H and Hauck C (2007) Geophysical imaging of alpine rock glaciers. *Journal of Glaciology* **53**(180), 110–120. doi: 10.3189/172756507781833893

McCarthy M, Pritchard H, Willis I and King E (2017) Ground-penetrating radar measurements of debris thickness on Lirung Glacier, Nepal. *Journal of Glaciology* **63**(239), 543–555. doi: 10.1017/jog.2017.18

Monnier S, Camerlynck C and Rejiba F (2008) Ground penetrating radar survey and stratigraphic interpretation of the Plan du Lac rock glaciers, Vanoise Massif, northern French Alps. *Permafrost and Periglacial Processes* **19**, 19–30. doi: 10.1002/ppp.610

Monnier S and Kinnard C (2013) Internal structure and composition of a rock glacier in the Andes (upper Choapa Valley, Chile) using borehole information and ground-penetrating radar. *Annals of Glaciology* **54**(64), 61–72. doi: 10.3189/2013AoG64A107

Nicholson LI, McCarthy M, Pritchard HD and Willis I (2018) Supraglacial debris thickness variability: impact on ablation and relation to terrain properties. *The Cryosphere* **12**(12), 3719–3734. doi: 10.5194/tc-12-3719-2018

Petersen EI, Holt JW and Levy JS (2018) High ice purity of Martian lobate debris aprons at the regional scale: evidence from an orbital radar sounding survey in Deuteronilus and Protonilus Mensae. *Geophysical Research Letters* **45**, 11595–11604. doi: 10.1029/2018GL079759

Petersen EI, Levy JS, Holt JW and Stuurman CM (2019a) New insights into ice accumulation at Galena Creek Rock Glacier from radar imaging of its internal structure. *Journal of Glaciology* **66**(255), 1–10. doi: 10.1017/jog.2019.67

Petersen EI and 7 others (2019b) The transition from Alpine Glacier to Rock Glacier at Sulphur Creek, Wyoming. Abstract C41E–1506, 2019 *Fall Meeting: American Geophysical Union*.

Potter N (1972) Ice-cored rock glacier, Galena Creek, northern Absaroka Mountains, Wyoming. *Geological Society of America Bulletin* **83**, 3025–3058.

Potter N and 5 others (1998) Galena Creek Rock Glacier revisited – new observations on an old controversy. *Geografiska Annaler: Series A, Physical Geography* **80**, 251–265.

Shean DE and Marchant DR (2010) Seismic and GPR surveys of Mullins Glacier, McMurdo Dry Valleys, Antarctica: ice thickness, internal structure and implications for surface ridge formation. *Journal of Glaciology* **56**(195), 48–64. doi: 10.3189/002214310791190901

Sihvola A (2008) *Electromagnetic Mixing Formulas and Applications*, 2nd edn, London: The Institution of Engineering and Technology.

Steig EJ, Fitzpatrick JJ, Potter N and Clark DH (1998) The geochemical record in rock glaciers. *Geografiska Annaler: Series A, Physical Geography* **80**, 277–286. doi: 10.1111/j.0435-3676.1998.00043.x

Telford W, Geldart L and Sheriff R (1990) *Applied Geophysics*, 2nd Edn. Cambridge: Cambridge University Press. doi: 10.1017/CBO9781139167932.

Wahrhaftig C and Cox A (1959) Rock glaciers in the Alaska range. *Geological Society of America Bulletin* **70**, 383–436.

Yilmaz O (1987) *Seismic Data Processing*. Tulsa: Society of Exploration Geophysicists.

https://doi.org/10.1017/jog.2022.90 Published online by Cambridge University Press

remote sensing

MDPI

Article

Photogrammetric Monitoring of Rock Glacier Motion Using High-Resolution Cross-Platform Datasets: Formation Age Estimation and Modern Thinning Rates

Tyler M. Meng [1,*], Roberto Aguilar [1], Michael S. Christoffersen [2], Eric I. Petersen [2], Christopher F. Larsen [2], Joseph S. Levy [3] and John W. Holt [1,4]

[1] Lunar and Planetary Laboratory, University of Arizona, Tucson, AZ 85721, USA
[2] Geophysical Institute, University of Alaska Fairbanks, Fairbanks, AK 99775, USA
[3] Department of Earth and Environmental Geosciences, Colgate University, Hamilton, NY 13346, USA
[4] Department of Geosciences, University of Arizona, Tucson, AZ 85721, USA
* Correspondence: tmeng@arizona.edu

Abstract: The availability of remote sensing imagery at high spatiotemporal resolutions presents the opportunity to monitor the surface motion of rock glaciers, a key constraint for characterizing the dynamics of their evolution. In this paper, we investigate four North American rock glaciers by automatically measuring their horizontal surface displacement using photogrammetric data acquired with crewed and uncrewed aircraft along with orbital spacecraft over monitoring periods of up to eight years. We estimate vertical surface changes on these rock glaciers with photogrammetrically generated digital elevation models (DEM) and digitized topographic maps. Uncertainty analysis shows that the imagery with the highest resolution and most precise positioning have the best performance when used with the automated change detection algorithm. This investigation produces gridded velocity fields over the entire surface area of each study site, from which we estimate the age of rock glacier formation using along-flow velocity integration. Though the age estimates vary, the ice within the modern extent of these landforms began flowing between 3000 and 7000 years before present, postdating the last glacial maximum. Surface elevation change maps indicate present-day thinning at the lower latitude/higher elevation sites in Wyoming, while the higher latitude/lower elevation sites in Alaska exhibit relatively stable surface elevations.

Keywords: photogrammetry; rock glacier; kinematics; UAS; airborne; satellite; flow; ablation; Alaska; Wyoming

Citation: Meng, T.M.; Aguilar, R.; Christoffersen, M.S.; Petersen, E.I.; Larsen, C.F.; Levy, J.S.; Holt, J.W. Photogrammetric Monitoring of Rock Glacier Motion Using High-Resolution Cross-Platform Datasets: Formation Age Estimation and Modern Thinning Rates . *Remote Sens.* **2023**, *15*, 4779. https://doi.org/10.3390/rs15194779

Academic Editor: Giuseppe Casula

Received: 2 July 2023
Revised: 9 September 2023
Accepted: 22 September 2023
Published: 30 September 2023

1. Introduction

1.1. Surface Motion of Rock Glaciers

Mountainous terrains with moderate precipitation and mean annual air temperatures less than or equal to 0 °C often develop ice and lithic-rich landforms known as rock glaciers. The ice units originate under a continuum of surface processes, including the burial of glacial ice by rockfall and ablation lag [1,2], preservation of overlapping debris and snow avalanche deposits [3], and the infiltration/refreezing of liquid water in rocky talus [4,5]. These ice/debris mixtures creep downslope under gravitational driving stresses to form discernible lobate morphologies, often superimposed by ridges, furrows, and flow bands [6]. In general, rock glaciers flow with an average surface displacement on the order of tens of centimeters to meters per year [1,7].

Previous measurements of active rock glacier flow have included both in situ and remote sensing methods. Before the availability of remote sensing data with temporal and spatial resolutions sufficient to track surface movement at the scales of rock glacier creep, surface-based displacement measurements were collected at benchmark positions at various locations along rock glacier surfaces [1,4,8–13]. Early displacement measurements

were made by repeatedly calculating the position of surface features in a local coordinate system referenced to stable bedrock points, marking the end of a "movement line". High accuracy and high precision global navigation satellite system (GNSS) positioning has recently allowed for displacement measurements through the monitoring of surface features' absolute positions over known time intervals. These point measurements are only possible at surface locations that are safely accessible and stable for repeated measurement, which limits this form of surface motion data both temporally and spatially.

Recent developments in remote sensing technology have created the opportunity to observe rock glacier flow with higher spatiotemporal resolution. Photogrammetric techniques using data collected via uncrewed aerial systems (UAS), piloted overflights, or optical satellite imagery provide a solution to the spatial limitations of surface-based point measurements of rock glacier surface features, as a photogrammetric orthomosaic encompasses a larger percentage of a rock glacier's surface than a set of ground-based point measurements. In addition to optical imagery, interferometric synthetic aperture radar (InSAR) has been used to measure rock glacier surface displacement with high precision [14–16]; however, such surveys are limited by the orbital geometry of the instrument and the flow direction of each target, as the displacement is measured along the line of sight of the InSAR system. Overall, remote monitoring provides a method to produce regularly repeated measurements of features in rugged and isolated terrain, which benefits time series analysis through the availability of a longer record length and higher sampling frequency. The ability to consistently track rock glacier surface motion has led to significant advances in the understanding of rock glacier kinematics and its relationship with glacier and permafrost dynamics [7,17–24]. New information regarding the extents and magnitudes of rock glacier flow fields addresses Tasks 1, 2, and 3 of the International Permafrost Association Action Group for Rock Glacier Inventories and Kinematics (RGIK) by contributing to a database of rock glacier attributes, including locations, surface areas, and flow velocities [6,25].

With the objective of monitoring rock glacier activity, inferring their flow history, and characterizing their kinematics and dynamics, we present new surface motion measurements on four North American rock glaciers, two in Wyoming and two in Alaska. We use an existing image correlation algorithm to detect feature displacement over time intervals of up to eight years in an analysis using optical imagery collected with UAS, airborne, and satellite platforms. Using the gridded velocity fields of the entire surface area of each rock glacier, we estimate the age of each landform by integrating head-to-toe velocity profiles, then we discuss their relationship with documented glacial advances in the region of each study site. We use the elevation data produced by the photogrammetric processing to estimate surface elevation change and modern rock glacier thinning rates. Our study aims to examine the local heterogeneities in rock glacier evolution by comparing the surface motion and elevation change of two rock glaciers in each geographic region. We achieve these objectives using a combination of UAS, airborne, and satellite imagery with photogrammetric processing and surface change analysis. High-resolution data capturing the three-dimensional change of rock glacier surfaces can provide a foundation for future monitoring campaigns and further investigation of rock glacier dynamics. Our study adds new surface change datasets for four rock glaciers to the existing inventory of rock glacier activity. In addition, it presents novel techniques for evaluating the uncertainty of surface change results and interpreting these results in the context of Quaternary geology.

1.2. Study Areas

1.2.1. Absaroka Mountains, Wyoming

Due to their central location in the contiguous United States and their relative accessibility by road, the small population of rock glaciers in the Absaroka Mountains of northwest Wyoming have been the subject of the longest-lived and most comprehensive studies of any rock glaciers or debris-covered glaciers in North America. Galena Creek Rock Glacier (Figure 1a, henceforth referred to as "Galena Creek") has been the partic-

ular focus of heated debate over the origins of ice in rock glaciers. The discussion has centered on whether to classify these features as ice-cored (glaciogenic) or ice-cemented (periglacial) rock glaciers [1,26–28]. Surface boulder displacement monitoring began at Galena Creek in the 1960s [1]. Based on geomorphic and geophysical data, along with observed ice exposures, it was concluded that the upper section of Galena Creek is an active ice-cored rock glacier consisting of glacier ice buried beneath an unconsolidated layer of debris. The debate has continued, as skeptics have attempted to refute the evidence of the glacial ice core [26], although this debate was largely settled in the 1990s when a drilling campaign at Galena Creek retrieved an ice core nearly 10 m long indicating the present-day existence of a debris-covered glacier [29]. This drill core contained a unit of bubbly ice with thin layers of gravel and sand, and the isotopic composition of this ice indicated that it originated as a glacier rather than as frozen interstitial meltwater [30]. Further exploration using ground-penetrating radar (GPR) revealed dipping debris bands in the cirque of Galena Creek, suggesting an ongoing ice accumulation process facilitated by the deposition of debris on the surface of the glacier [3]. On this upper portion of the rock glacier where there is a glacial ice unit, the debris is approximately 0.8–1.5 m thick [31]. With these observations in mind, we interpret the upper two-thirds of Galena Creek to be a debris-covered glacier. In comparison, the lower third of Galena Creek has slower surface velocities, a debris mantle thicker than 2 m, and a lower ice concentration, resembling an older ice-cemented rock glacier modified by periglacial processes and possible interactions with the advancing debris-covered glacier, similar to processes that have been documented at other rock glaciers. [12,31–34].

Sulphur Creek Rock Glacier (Figure 1b, henceforth referred to as "Sulphur Creek") lies approximately 3 km southeast of Galena Creek. Despite this proximity to Galena Creek, Sulphur Creek has received relatively less geological research attention due to its larger surface area, higher topographic relief, and more difficult access. Historical photos acquired in 1893 during a surveying expedition led by Thomas A. Jaggar, Jr., showed a clean ice glacier in the cirque of the Sulphur Creek basin, with a thin supraglacial debris layer developing a few hundred meters downslope of the location of the terminus of the present-day debris-free snow and ice [35]. Recent GPR measurements indicate a transition from an alpine debris-covered glacieret to a relatively ice-poor rock glacier as elevation decreases along the length of Sulphur Creek [31]. The same measurements showed that the debris on the glacieret ranges from 0.1–1 m thick, while the debris on the lower glacier is greater than 2 m thick. Both Galena Creek and Sulphur Creek follow the Östrem curve [36], showing evidence of sub-debris ice melt where the debris is thin; at the surface of both sites, streams can be heard flowing at the debris–ice interface. These two rock glaciers provide unique examples of the effect of debris supply and valley geometry on ice units transitioning between glaciers, debris-covered glaciers, and rock glaciers [37].

1.2.2. Wrangell Mountains, Alaska

Sourdough Peak is a mountain in Wrangell–St. Elias National Park that hosts two large lobate rock glaciers. The rock glacier flowing down the peak's southern flank is named Sourdough Rock Glacier (Figure 1d, henceforth referred to as "Sourdough" for simplicity), and the rock glacier flowing down its northwest slope is McCarthy Creek Rock Glacier (Figure 1e, henceforth referred to as "McCarthy Creek"). Sourdough has been surveyed with GPR; these surveys detect a landform thickness of up to 50 m, and the dielectric mixing model indicates volumetric ice concentrations greater than 50 percent based on the radar wave speed within the rock glacier [31]. The ice-free debris thickness measurements at Sourdough are generally greater than 2 m, although runoff can be observed through the sound of localized sub-debris streams despite the thickness of the overburden. The McCarthy Creek site has not been studied with in situ geophysical methods. A surface motion survey at Fireweed Rock Glacier, which is a nearby rock glacier in the Wrangell Mountains, measured velocities exceeding 3.5 $\frac{\mathrm{m}}{\mathrm{yr}}$ [13]. The oversteepened terminus of this rock glacier experiences periodic slope failure events when heavy precipitation swells its

proglacial stream, a process that may impact the dynamics of the rock glacier and the characteristics of its velocity field in comparison with Sourdough and McCarthy Creek.

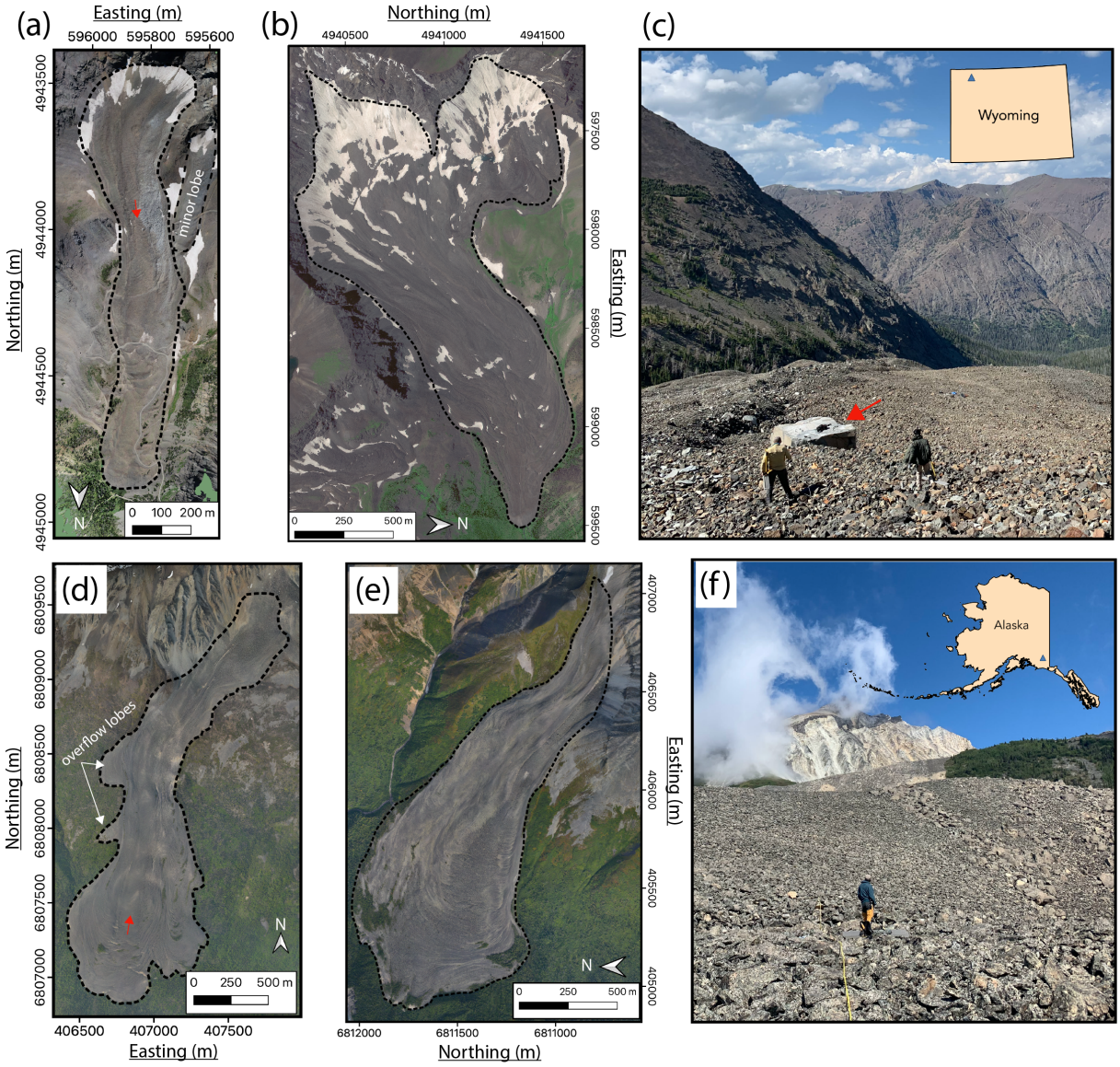

Figure 1. Projected orthomosaics and surface photos showing the rock glaciers targeted in this study. (**a**) Galena Creek Rock Glacier, Wyoming (Galena Creek), UAS image acquired in August 2022 and projected to WGS 84/ UTM Zone 12N. The red arrow shows the location and viewing direction of the photo in panel (**c**). (**b**) Sulphur Creek Rock Glacier, Wyoming (Sulphur Creek), satellite imaged acquired in August 2022 and projected to WGS 84/ UTM Zone 12N. (**c**) Field photo at Galena Creek, showing debris clast size distribution and topographic relief. The red arrow identifies the boulder used for the example in Figure 2. (**d**) Sourdough Rock Glacier, Alaska (Sourdough), airborne image acquired in May 2014 and projected to WGS 84/UTM Zone 7N. The red arrow shows the location and viewing direction of the photo in panel (**f**). (**e**) McCarthy Creek Rock Glacier, Alaska (McCarthy Creek), airborne image acquired in in August 2014 and projected to WGS 84/UTM Zone 7N. (**f**) Field photo at Sourdough. The images have been rotated to make the direction of flow point roughly towards the bottom of the page. All rock glacier outlines presented are the extended delineations [6], including the input talus slopes and front and lateral margins. All subsequent maps use the same projections as those shown here.

2. Materials and Methods

2.1. Photogrammetric Data Acquisition and Processing

For this investigation, our objective was to measure feature displacement with remote imagery over multiple time intervals and compile the longest possible time series of surface displacement for each study site. To detect surface velocities less than 1 $\frac{\text{m}}{\text{yr}}$ at seasonal intervals, it is necessary to use decimeter-resolution imagery to resolve the details of the surface features as well as to detect displacements on the order of decimeters. The imagery for our two Wyoming sites was collected via UAS, crewed aircraft, and satellite platforms between 2020 and 2022. The Alaska sites were targeted by a crewed airborne photogrammetry campaign between 2014 and 2022. Supplementary Figure S1 details the methodological workflow for measuring the surface displacement and elevation change with these combined data sources. Below, we discuss the advantages and disadvantages of these methods at each site and compare our remote sensing results with surface-based boulder displacement measurements at Galena Creek.

2.1.1. Wyoming

In August 2020 and August 2022, we acquired photogrammetry data covering Galena Creek using a DJI Phantom 4 RTK UAS. We used the DJI GS RTK flight planning software in 2D Photogrammetry mode with terrain awareness. In 2022, eight ground control points (GCP) were deployed and surveyed. For both years, the GCP locations were measured using real-time kinematic positioning (RTK) with Emlid Reach RS2 GNSS receivers. The coordinates of the base station were postprocessed with precise point positioning using the Canadian Spatial Reference System Precise Point Positioning tool. We used Emlid Studio software version 1.3 to apply the postprocessing kinematics to the UAS images.

The photogrammetric processing workflow was carried out using Agisoft Metashape Professional software version 1.7.5 build 13229. After the photos were aligned and the dense clouds were created, digital elevation models (DEM) and orthomosaics were generated for further analysis. The detailed parameters used in the workflow for each flight are provided in the processing reports included with the supplementary materials, and the workflow diagram is shown in Supplementary Figure S1. These orthomosaics have a spatial resolution of 7.9 $\frac{\text{cm}}{\text{pixel}}$ for 2020 and 5.4 $\frac{\text{cm}}{\text{pixel}}$ for 2022 (Table 1), and the DEMs have a pixel width double that of their corresponding orthomosaics. In 2022, four points were used as control at Galena Creek, with a root mean square (RMS) error of 0.012 m, and the remaining four points were check point (CP), with an RMS error of 0.068 m. To supplement the two UAS datasets, we purchased satellite imagery from the SkyMap50 system through Soar.Earth, a commercial organization that distributes orbital imagery data. We obtained one complete 41.1 $\frac{\text{cm}}{\text{pixel}}$ SkyMap50 scene of Galena Creek without clouds, acquired on 10 July 2021.

We compared independent motion measurements at Galena Creek using surface-based and remote sensing methods. Large debris clasts on the Galena Creek surface were marked with paint in the 1960s to measure rock glacier surface motion, and the set of marked clasts was expanded and updated with new paint and bolts in the 1990s [1,29]. The paint markings and identifying symbols on the clasts remain legible. We collected positioning data for 22 identifiable marked boulders using the Emlid Reach RTK system in August 2022 and compared these locations to measurements collected in 1997, 1998, 1999, and 2015 [12,29,38]. Because the measurements from the 1990s and 2015 were acquired with a total station, we converted the local coordinate system used for these earlier datasets to the WGS84 / UTM Zone 12N projected coordinate system using a USGS benchmark and stationary points on stable bedrock for direct comparison with the 2022 RTK measurements.

Table 1. List of acquisition details for the imagery used for the change detection analysis at each field site (GC = Galena Creek; SC = Sulphur Creek; SRG = Sourdough; MC = McCarthy Creek). Each date is provided in YYYYMMDD format.

Region	Site	Date	# of Images	Avg. Camera Error (cm)	Resolution ($\frac{cm}{pixel}$)	# of GCP/CP	GCP/CP RMSE (cm)
Wyoming	GC	20200823 [U]	1076	0.3	7.9	0/0	n/a
	SC	20200825 [A]	269	n/a	10.8	10/3	0.44/28.3
	GC	20210710 [S]	1	n/a	40.1	0/0	n/a
	SC	20210710 [S]	1	n/a	41.0	0/0	n/a
	SC	20220807 [S]	1	n/a	41.3	0/0	n/a
	GC	20220808 [U]	941	0.8	5.4	4/4	0.97/7.59
Alaska	SRG, MC	20140525 [A]	433	16.2	20.0	0/0	n/a
	SRG, MC	20140823 [A]	345	17.2	19.8	0/0	n/a
	SRG, MC	20150523 [A]	546	15.2	20.6	0/0	n/a
	SRG, MC	20150829 [A]	561	18.8	19.3	0/0	n/a
	SRG, MC	20160601 [A]	614	14.5	25.3	0/0	n/a
	SRG	20160817 [A]	494	21.9	24.2	0/0	n/a
	SRG, MC	20190905 [A]	628	65.3	12.1	0/0	n/a
	SRG	20200517 [A]	215	9.7	12.4	0/0	n/a
	SRG, MC	20201018 [A]	520	80.5	12.4	0/0	n/a
	SRG, MC	20210622 [A]	340	11.7	14.8	0/0	n/a
	SRG	20220708 [A]	357	26.2	18.5	0/0	n/a

[U] UAS image; [A] Piloted airborne image; [S] SkyMap50 satellite image.

At Sulphur Creek, airborne imagery was collected on 25 August 2020 by Kestrel Aerial Services using a Canon EOS 5D Mark III DSLR with a Canon EF 50 mm 1.2 lens. The positioning information was recorded by a Garmin Aera 796 synchronized with the camera clock mounted in the panel of the aircraft. For this acquisition, we used ten GCPs to optimize the positioning of the imagery. The individual images and their positions were delivered as georeferenced TIFF files, and these data were processed in Agisoft Metashape to generate an orthomosaic and DEM. The ten points used as control had an RMS error of 0.0004 m, and three points used as check points had an RMS error of 0.283 m. In addition to the 2020 airborne image, we obtained one partial image and one complete image of a cloudless Sulphur Creek available in the SkyMap50 collection. The image from 7 August 2022, contains the full rock glacier, while the lowest 500 m section of Sulphur Creek is cut off at the eastern edge of the 10 July 2021 scene.

2.1.2. Alaska

The photogrammetry data for Sourdough and McCarthy Creek were acquired during eleven piloted overflights between May 2014 and July 2022 (Table 1). The flights were planned with the objective that more than nine overlapping images would cover the target surfaces. The 2014–2016 images were collected with a Nikon D800 DSLR and the 2019–2022 images were collected with a Nikon D850 DSLR, both with a Zeiss Distagon 25 mm lens. Each raw image was collected in NEF format and postprocessed to maximize contrast before conversion to JPG format. Aircraft positions were measured with a Trimble R7 GNSS receiver recording at 5 Hz. Following [39], an intervalometer was used to trigger event markers in the GNSS data associated with each camera flash. These coordinates were transformed from the GNSS antenna to the camera image plane using a triple coordinate rotation of the measured lever arm for the aircraft's antenna/camera configuration.

By interpolating the camera positions from the 5 Hz GNSS data with the event markers, each image was tagged with a position to approximately 10 cm accuracy [39]. From these tags, a camera position file associating each JPG image name and position was generated and used as a reference for the photogrammetric processing steps. We followed the same Agisoft Metashape workflow described in Section 2.1.1. The individual processing reports

for each flight are provided in the supplementary information. Due to logistical limitations in the field, no GCPs were used in the photogrammetric processing for the Alaska sites, and there were no surface boulder measurements or GCPs to provide direct in situ validation for these sites. Sourdough was imaged with all eleven flights, while McCarthy Creek was only imaged on eight of the eleven flights due to variable weather conditions in the narrower McCarthy Creek Valley. The acquisition dates and original resolutions of all rock glacier imagery analyzed in this study are provided in Table 1.

2.2. Change Detection Analysis

To automatically measure the horizontal rock glacier surface displacement between image pairs, we used the free correlation image analysis software CIAS [7,40]. This algorithm, available as a compiled IDL program, requires grayscale images with identical extents and resolutions in a Cartesian coordinate system. We preprocessed the images using the Geospatial Data Abstraction Library (GDAL) within the QGIS user interface. Both of these software packages are open source. To preprocess the images, we used the GDAL *Warp* tool to project the raster data to their appropriate Cartesian coordinate systems from the WGS84 geographic coordinates (UTM zone 7N for the Alaska sites and zone 12N for the Wyoming sites). *Warp* was used to clip the images to an appropriate extent and to resample the images to the resolution of the coarsest image in the pair with the cubic spline resampling method. Finally, the grayscale images used for the change detection input were extracted from the RGB data using the GDAL *Translate* tool.

After preprocessing the images, each image pair in the set was analyzed to derive the surface displacement vectors over the time interval between acquisitions. All of the image pairs at each field site were analyzed using a common set of grid points specified by a file containing the Cartesian coordinates of each grid point. The Galena Creek datasets were analyzed on a 5 m $\times$ 5 m grid, while the more extensive Sulphur Creek and Alaskan sites were analyzed on a 10 m $\times$ 10 m grid. All of the image pairs were analyzed using normalized cross-correlation and the normal pyramid matching speed. Our experiments with CIAS determined that a reference block of 45 pixels $\times$ 45 pixels and a search window of 100 pixels $\times$ 100 pixels at each grid point was optimal for correlating surface features and detecting realistic displacements for all of the image resolutions and time periods analyzed (Figure 2). Due to the forest cover surrounding the Alaska sites, which obscured the stable terrain, co-registration was not performed for individual image pairs. Instead, we used the minimum uncertainty in surface displacement as the averaged CIAS-derived displacement value for stable, off-glacier terrain within each scene. We verified these displacement values through manual inspection of stable surface features wherever possible. This added the benefit of decreasing the processing time and avoiding the application of inconsistent uncertainties due to an extra transformation step unique to the processing workflow of each image pair. To convert the displacement results into the surface velocity in $\frac{\mathrm{m}}{\mathrm{yr}}$, we found the precise number of years between images by dividing the number of days between each image pair by 365.25 days per year, then divided the displacement in meters by the time interval in years.

In image pairs for which one or both of the images is a SkyMap50 image targeting Galena Creek or Sulphur Creek, there is a static offset in the images due to limitations in image precision using the positioning of a space-borne camera. To solve this issue of imprecise image co-registration, we first ran the change detection algorithm on the images with their initial positioning information. We selected a subset of displacement vectors over a portion of the images interpreted to be stable bedrock. The mean of this subset of displacement vectors was subtracted from the projected coordinates of the corners of the later image in the image pair to shift the geolocated image using the "-a_ullr" flag in the GDAL *Translate* function to correct for the initial static shift. The largest magnitude of the shifts that were used was 1.56 m for the Galena Creek July 2021 SkyMap50 image; the parameters for each shift are shown in Table 2.

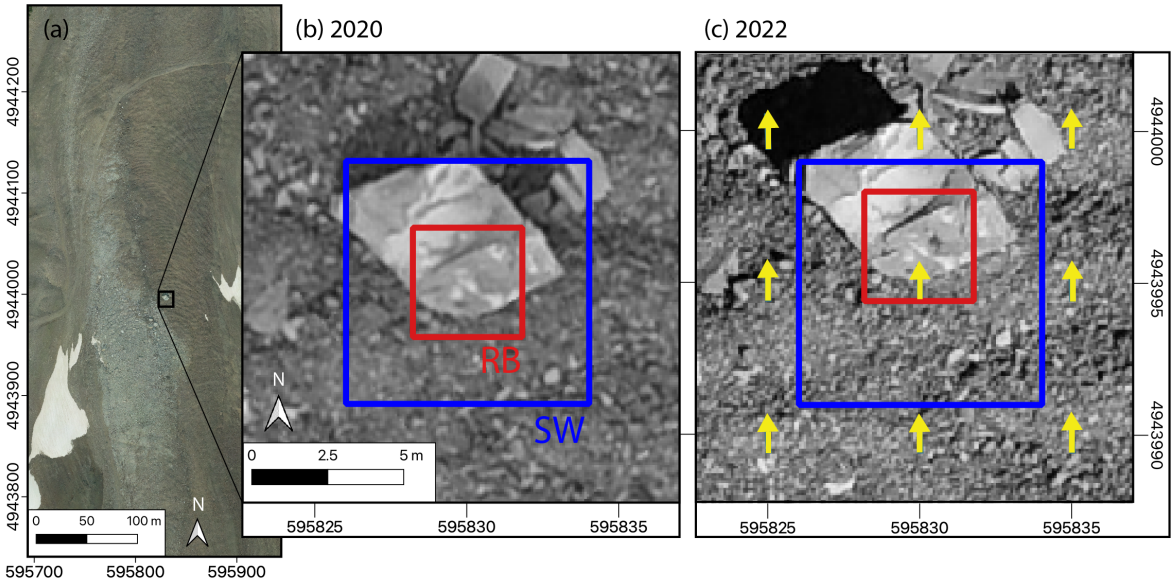

Figure 2. Schematic of the change detection procedure applied to a boulder identified at a central location in the August 2020/August 2022 image pair at Galena Creek (**a**), where the red box labeled RB represents the 45 × 45 pixel reference block and the blue box labeled SW represents the 100 × 100 pixel search window. The movement of RB between 2020 (**b**) and 2022 (**c**) shows the displacement measured as the location of the peak normalized correlation coefficient within the search window. The yellow arrows represent the two-year displacement vectors measured by CIAS; this boulder moved approximately 1.2 m at an azimuth of 358°.

The change detection process was then performed again, this time using the shifted SkyMap50 image with its corresponding unshifted image partner. Its results were verified by manually examining off-glacier stationary features in both the unshifted and shifted images for each pair containing a SkyMap50 scene. The new change detection results were compared with the initial results of the unshifted images after subtracting the mean displacement of the stationary subset for further verification and uncertainty analysis. The added step of translating the second image of the pair, along with the relatively lower resolution of the SkyMap50 imagery (42 $\frac{cm}{pixel}$) compared with the drone imagery (<10 $\frac{cm}{pixel}$), leads to a higher uncertainty in those surface displacements estimated with pairs containing a shifted satellite image.

Table 2. Static shift applied to the SkyMap50 images to minimize the measured displacement of stationary terrain in each image pair.

Rock Glacier	Image 1	Image 2	Δx (m E)	Δy (m N)
Galena Creek	10 July 2021 ^{S*}	8 August 2022 ^{U}	−0.99	−1.20
Sulphur Creek	10 July 2021 ^{S}	7 August 2022 ^{S*}	0.84	−1.25
Sulphur Creek	25 August 2020 ^{A}	7 August 2022 ^{S*}	0.81	0.68

^{U} UAS image; ^{A} Piloted airborne image; ^{S} SkyMap50 satellite image; * Denotes that the image was shifted relative to the other image in the pair.

2.3. Surface Elevation Change

For the UAS and airborne datasets, the photogrammetric processing workflow produces DEMs with pixel widths twice those of their corresponding orthomosaics (Supplementary Figure S1); thus, the DEMs used in this study range from approximately 10–50 $\frac{cm}{pixel}$. Using these elevation maps, we calculated the surface elevation changes for Galena Creek, Sourdough, and McCarthy Creek over the time intervals between the earliest and latest photogrammetric acquisitions in order to observe any detectable signatures of horizontal flow or vertical thinning. For Galena Creek, the elevation change was calculated over the

August 2020/August 2022 interval; for Sourdough, the May 2014/July 2022 interval was used; and for McCarthy Creek, the May 2020/June 2021 interval was used. All of these elevation differences were calculated by subtracting the earlier DEM from the later DEM in each pair using the *Raster Calculator* tool in QGIS with the coarsest-resolution DEM as the reference.

To examine the surface change at Sulphur Creek, we calculated the difference between the DEM produced by the August 2020 airborne photogrammetry flight and the $\frac{1}{3}$ arcsecond resolution (approximately 10 m) DEM tile from the USGS 3D Elevation Program (3DEP) [41]. The spatial metadata for this tile indicate that the 3DEP data at Sulphur Creek was sourced from topographic information measured in 1985. Because this location in the 3DEP dataset is mostly barren land, the error of this $\frac{1}{3}$ arcsecond DEM is estimated to have a mean bias of -0.85 m with a standard deviation of 2.42 m [42]. We consider this bias in the data when interpreting the elevation change results discussed below.

3. Results

3.1. Wyoming

3.1.1. Galena Creek

At Galena Creek, the August 2020/August 2022 image pair resampled to 8.0 $\frac{\text{cm}}{\text{pixel}}$ resolution provided the best change detection signal in the set of image pairs. Surface displacement is detectable along the main trunk of the rock glacier, in contrast to the adjacent stationary terrain (Figure 3b). The displacements have a strong correlation with the surface slope, indicating a direct relationship between driving stress and flow velocity. The change detection algorithm cannot measure displacements on surface regions when there is snow in one or both of the images due to the low contrast and lack of pixel correlation within the reference block. These regions cause "noisy" results, which are identifiable in the mapped displacement vectors as regions with random displacement vector magnitude and direction that are associated with the snow patches when the displacement vectors are mapped over the base images. The effect of these noisy regions on the analysis of the data is mitigated by ignoring the displacement vectors greater than a noise threshold, which is determined by visually evaluating the flow field to find the maximum displacement with a direction that agrees with the local topography. For the case of Galena Creek, this threshold is approximately 1.6 $\frac{\text{m}}{\text{yr}}$. The noise may be further filtered by ignoring vectors where the displacement direction differs from the slope azimuth by more than 45°. The minimum displacement error for each image pair is taken to be the greater value of either the minimum displacement over a region interpreted to be stationary or the pixel size of the images. Using these metrics, a pair of low-altitude UAS images acquired with the same camera and positioning system for both surveys returned the best displacement measurements out of all the datasets presented here.

The photogrammetry data collected at Galena Creek allowed us an opportunity to directly compare the efficacy of the change detection method using imagery from homogeneous and heterogeneous platforms. We performed a hybrid change detection experiment using the 42 $\frac{\text{cm}}{\text{pixel}}$ SkyMap50 satellite image from July 2021 and the August 2022 UAS image resampled to 42 $\frac{\text{cm}}{\text{pixel}}$ with the cubic spline method. The displacement patterns in the upper two-thirds of the rock glacier are similar between the homogeneous change detection results and the hybrid results. The magnitude of the displacement is directly correlated with the surface slope (Figure 3c); however, the coarser resolution of the satellite image in the lower third of the rock glacier means that the proportion of mismatches and undetected movements increases due to the increased difference in pixel size between the original UAS and satellite images [43].

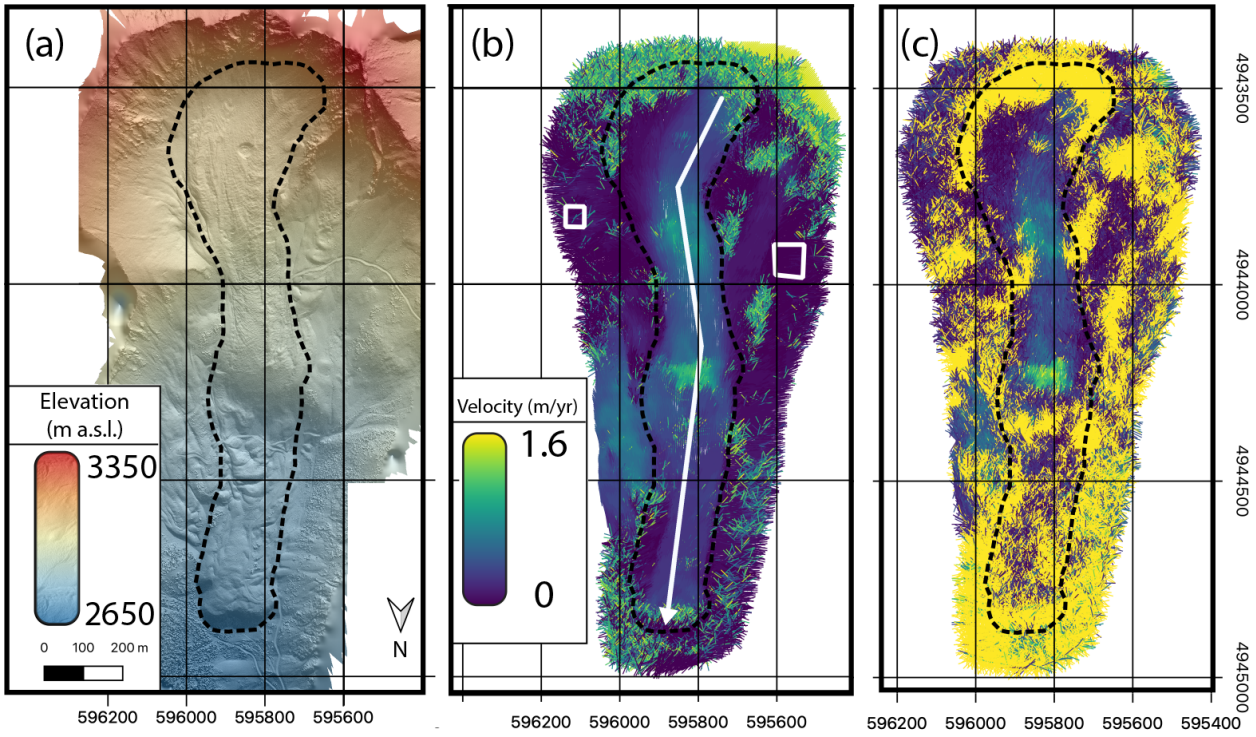

Figure 3. Galena Creek photogrammetry results: (**a**) DEM and hillshade produced from the August 2022 UAS flight; (**b**) surface velocity field derived from change detection between the August 2020 and August 2022 UAS-derived orthomosaics; (**c**) surface velocity field derived from change detection between the shifted July 2021 satellite image and the August 2022 orthomosaic. For reference, the extended rock glacier outline is delineated as a dashed line in each panel, the white line in (**b**) marks the profile that was sampled for the age analysis discussed below, and the white boxes in (**b**) indicate the stable points used in the uncertainty analysis.

3.1.2. Sulphur Creek

We detected a flow signal on the Sulphur Creek surface (Figure 4) using the August 2020 airborne imagery combined with the August 2022 SkyMap50 image, which was linearly shifted to account for the co-registration error between the two images (Table 2). Although the displacement values on the stable surfaces of the rock glacier surface indicate a relatively high baseline uncertainty, there is a signal of increased flow velocity on the lowest lobe of the rock glacier. In contrast, there does not appear to be substantial downslope movement in the middle portion of the rock glacier, where GPR and geomorphic observations indicate ice thicknesses of less than 10 m and stagnation of the ice [31,37].

These change detection results support the hypothesis of ice stagnation on a deflating debris-covered glacier that is transitioning to dead ice. The directions of the displacement vectors on this central portion of the glacier agree with the slope aspect (approximately 150°), suggesting movement toward the middle line of the glacier. This movement may be an effect of rapid recent thinning by incision of a supraglacial stream and subsequent ice flow from the thicker ice at the glacier margins to the thinned ice in the middle (see the elevation change results in Section 3.3). Alternatively, if the thinning is concentrated along a longitudinal line associated with a stream in the center of the glacier, this could lead to a reduction in the cross-flow buttressing force, allowing the lateral portions of the glacier to cohesively slide along the base towards the central trough. With either mechanism, this downwasting appears to preserve the surface debris structure, as the change detection algorithm successfully tracks features in the region over a spatial scale of a few hundred meters.

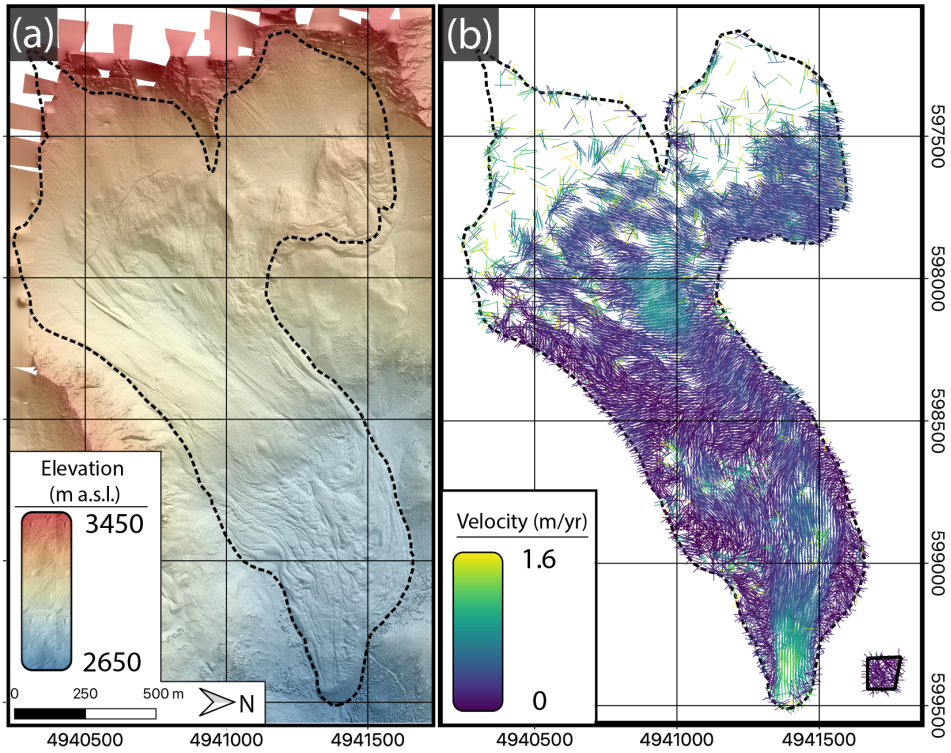

Figure 4. Sulphur Creek photogrammetry results: (**a**) DEM and hillshade produced from the August 2020 piloted overflight and (**b**) surface velocity field derived from change detection between the August 2020 airborne orthomosaic and the shifted August 2022 satellite image. For reference, the extended rock glacier outline is delineated as a dashed line in each panel. The box in the lower right corner of (**b**) indicates the stable area used for the uncertainty analysis.

3.2. Alaska

3.2.1. Sourdough

The data at Sourdough represent the longest monitoring period of the sites presented here, spanning from May 2014 to July 2022 (Figure 5, Table 1). To characterize the temporal variations in the flow field, we calculated surface displacements for image pairs from adjacent years (Figure 6) and the progressive displacement for subsequent images with respect to the May 2014 initial image. All of the annual image pairs show a consistently fast-moving region with distinct shear margins on the lower trunk of the rock glacier flowing at rates greater than 1 $\frac{\mathrm{m}}{\mathrm{yr}}$ (Figure 6), indicating a high level of rock glacier activity. We ignore velocity vectors with magnitudes greater than 1.8 $\frac{\mathrm{m}}{\mathrm{yr}}$, as visual examination indicates that all greater values are qualitative outliers with no directional correlation to the surrounding data points. These spurious velocity vectors are considered noise due to mismatched pixel blocks in the change detection routine. The resulting velocity maps distinguish an active secondary lobe that branches southeast from the main trunk after flowing around a bedrock pinning point. Below this pinning point, the flow of the main trunk and secondary lobe diverges and slows as the slope flattens, creating the characteristic tongue-shaped lobes of the lower rock glacier. Stagnant overflow lobes with low displacements are observed along the west edge of the feature (Figure 1a). While these flow patterns are evident when observing the full set of image pairs with intervals of one year or greater; the results of individual image pairs vary in quality, making it difficult to asses possible seasonal signals in the flow field.

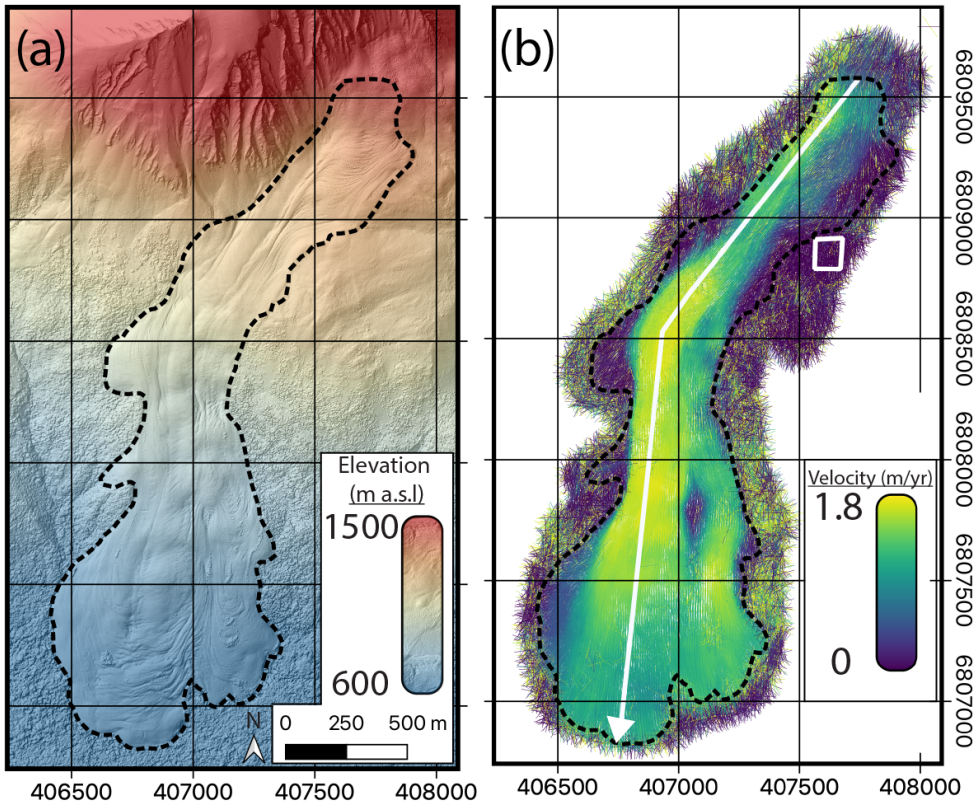

Figure 5. Sourdough photogrammetry results: (**a**) DEM and hillshade produced from the May 2014 piloted overflight and (**b**) surface velocity field derived from change detection between the May 2014 and September 2019 airborne orthomosaics. For reference, the extended rock glacier outline is delineated as a dashed line in each panel, the white line in (**b**) marks the profile that was sampled for the age analysis detailed below, and stable area used for the uncertainty analysis is marked by the white box in (**b**).

The displacement signal is generally stronger in the image pairs with longer time intervals. This indicates that larger displacements are detected more readily and consistently as long as the search window is large enough to contain the range of realistic displacements. The image pair with the greatest amount of noise is the September 2019/October 2020 interval; this noise is largely correlated with the presence of snow on the upper two-thirds of the rock glacier in the October 2020 image. This snow obscures surface features, which leads to inconsistencies in pixel intensity patterns, causing the normalized cross-correlation algorithm to fail. The remaining image pairs with annual time intervals exhibit a consistent pattern of increased surface velocity in the trunk of the rock glacier, although these results have varying degrees of signal and noise. To estimate the total displacement and average velocity of the rock glacier surface over the entire measurement period, we measured the displacement for all of the images as referenced to the May 2014 image (Supplementary Figure S2). This method successfully detects a peak velocity of approximately 1.5 $\frac{\mathrm{m}}{\mathrm{yr}}$ in the central trunk of the rock glacier; however, comparing the results from images acquired at different times of year does not reveal any surges or seasonal signals in the velocity field. Shorter time intervals between acquisitions and imagery with increased spatial resolution paired with permanent GNSS stations on the rock glacier's surface could shed further light on its seasonal flow patterns [44].

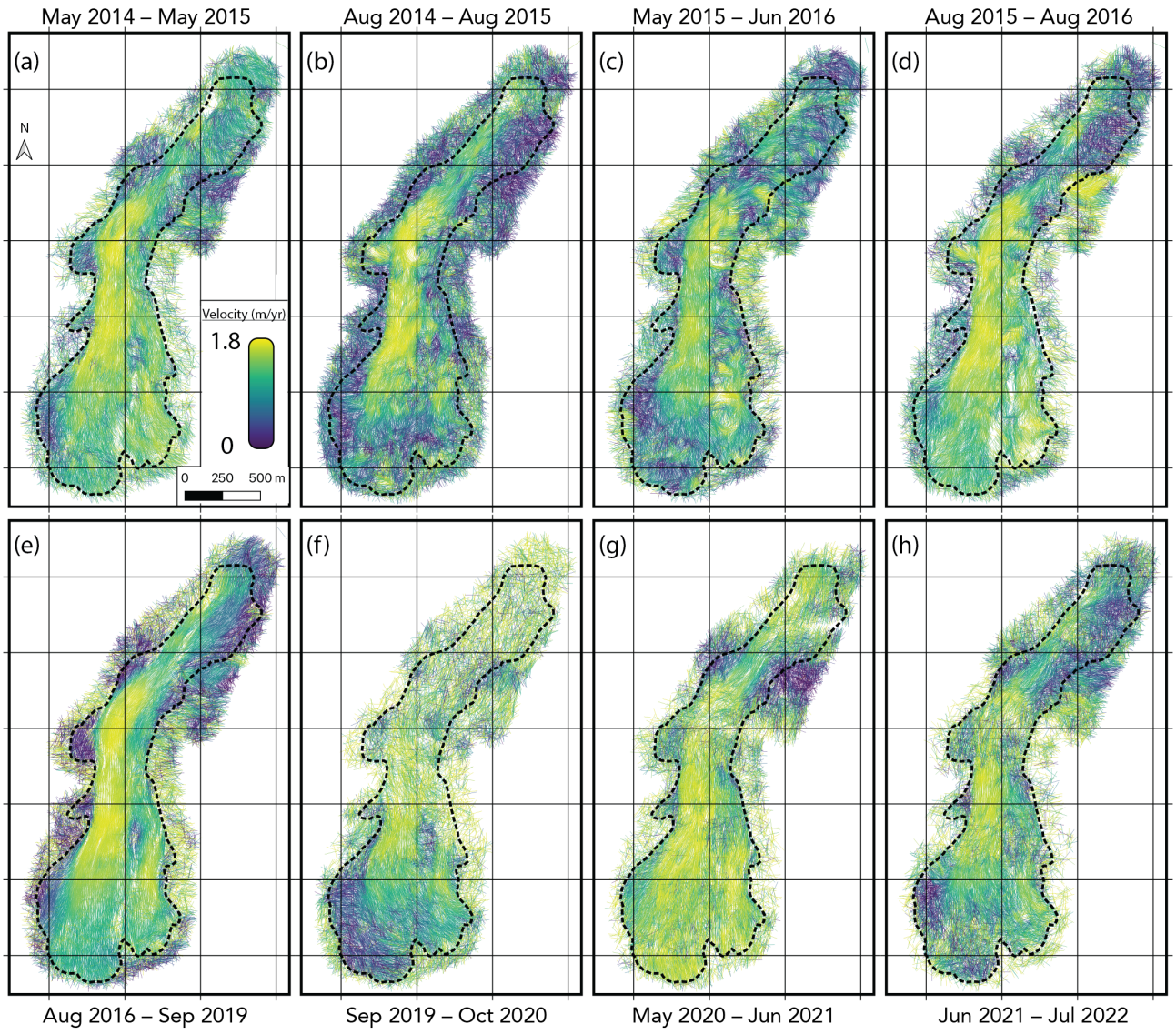

Figure 6. Surface velocity results for Sourdough using image pairs with time intervals of one year or more, demonstrating the range in quality of the change detection results for different image pairs and time intervals. The grid used for these maps is equivalent to the grid used in Figure 5, where the grid lines are drawn at 500 m intervals in the x and y directions in the projected coordinate system. Each panel (**a**–**h**) shows the results from image pairs, progressing in chronological order.

3.2.2. McCarthy Creek

The results at McCarthy Creek are generally noisier than at Sourdough, and the change detection results for the entire measurement period at McCarthy Creek show a flow pattern with a maximum velocity approximately half that of Sourdough (Figure 7). We chose to use the August 2014 image as the base image for the McCarthy Creek analysis because there was lingering snow on the upper portion of the rock glacier in the May 2014 image, meaning that the August 2014 image was able to detect a flow signal at higher reaches of the rock glacier. The fastest section of the rock glacier surface is the southern/upstream portion of its trunk, moving about 50 $\frac{\text{cm}}{\text{yr}}$, before slowing as the flow of the lower lobe diverges. At approximately 1200 m elevation the rock glacier branches into a fast southern lobe and a more stagnant northern lobe.

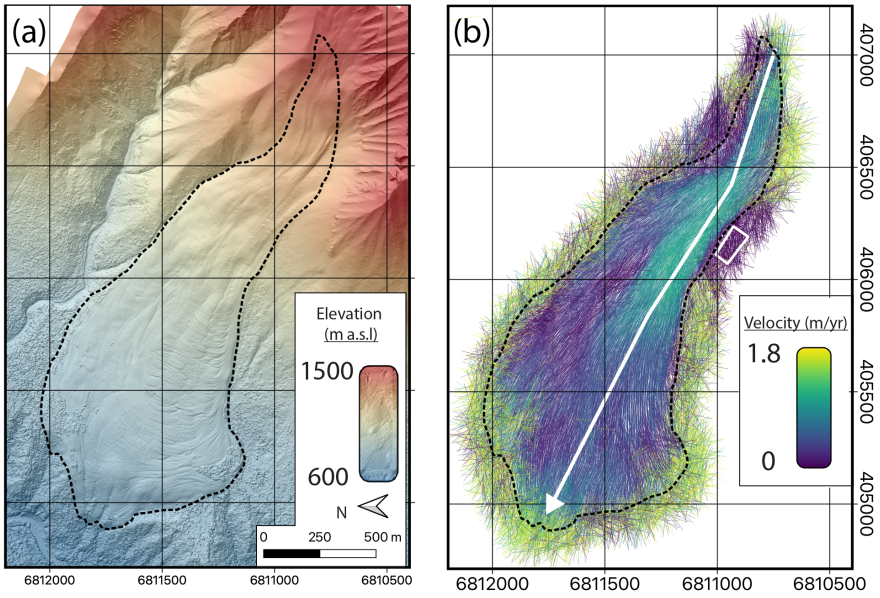

Figure 7. McCarthy Creek photogrammetry results: (**a**) DEM and hillshade produced from the May 2014 piloted overflight and (**b**) surface velocity field derived from change detection between the August 2014 and June 2021 airborne orthomosaics. For reference, the extended rock glacier outline is delineated as a dashed line in each panel, the white line in (**b**) marks the profile that was sampled for the age analysis below, and the stable area used for the uncertainty analysis is marked by the white box in (**b**).

There appears to be an increase in flow speed at the toe of the rock glacier, which could indicate a recent frontal advance or an increase in wasting and potential collapse of the rock glacier toe near the river channel of the McCarthy Creek drainage. However, this apparent signal could alternatively be caused by the combined geometric effects of the photogrammetric data acquisition, the surface slope at this location, and/or uncertainty due to vegetation on the surface. Similar to Sourdough, the change detection at McCarthy Creek performs the best for time intervals greater than one year, and the signal is generally stronger for longer time intervals (Figure 8). In Section 4.2, we discuss the estimation of the baseline uncertainty in these change detection results and how this affects further analysis and interpretation of the data.

3.3. Surface Elevation Change

At Galena Creek, subtracting the earlier DEM from the later DEM reveals indicators of both vertical thinning and surface-parallel motion (Figure 9a). There is an apparent bias of approximately −20 cm between the two DEMs, as shown by differencing the elevations of stable terrain. The elevation difference measured along a longitudinal profile on the rock glacier surface indicates a mean DEM difference of −40 cm with a standard deviation of 19 cm. By comparison, a sample of DEM differences on the stable ground provides a mean value of −18 cm with a standard deviation of 6 cm. A cross-flow profile of the elevation differences supports this observation as well (Supplementary Figure S3). This suggests that the rock glacier surface has lowered by 22 ± 13 cm over the two-year time interval. This 10 $\frac{\text{cm}}{\text{yr}}$ thinning rate for the upper two-thirds of the rock glacier agrees with previous estimates [12,38]. This thinning rate measurement further agrees with a thermal conduction model using air temperature data from the *Evening Star* Snowpack Telemetry (SNOTEL) meteorological station located <1 km east of Galena Creek at a similar elevation as the rock glacier's terminus (station ID = 472). This model uses an observed supraglacial debris thickness of 1.5 m [31], and the measured thinning rate fits a plausible range of thermal conductivities for the debris (Appendix A). The ice in the cirque of Galena Creek has a

GPR-measured thickness of >50 m; thus, assuming that this interpreted thinning rate of 10 $\frac{\text{cm}}{\text{yr}}$ remains constant, the glacial ice will be preserved here past the year 2500.

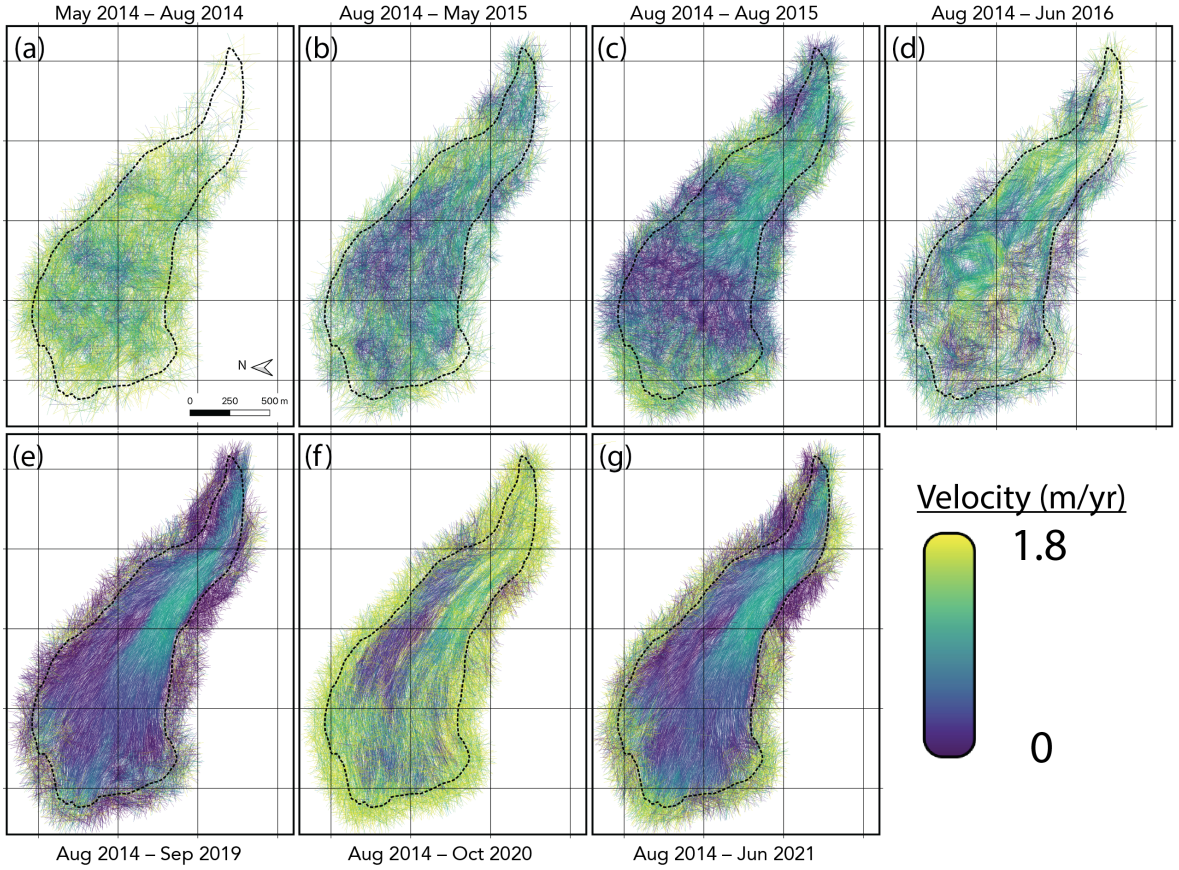

Figure 8. Surface velocity results for McCarthy Creek using image pairs, where each labeled panel was derived in reference to the August 2014 base image, demonstrating the general increase in quality of the change detection results at McCarthy Creek with increasing surface displacement while showing the impact of snow in the October 2020 image. The grid used for these maps is equivalent to the grid used in Figure 7, where the grid lines are drawn at 500 m intervals in the x and y directions in the projected coordinate system. Each panel (**a**–**g**) shows the results where images are chronologically compared to the August 2014 base image.

In addition to the overall thinning of the upper two-thirds of the rock glacier, flow-parallel oscillations in the DEM difference rasters are indicative of the translational motion of surface ridges/furrows, creating a positive value where a ridge has occupied previously void space and a negative value where a furrow has replaced a ridge. The distances between these troughs and crests in the oscillations of the DEM difference data are comparable with the surface displacement measured over the same period. Furthermore, strong negative values within the rock glacier boundaries appear to correlate with a sub-debris supraglacial creek that has been observed to expose ice to the surface. This observation suggests that ablation is concentrated in regions where ice has been exposed to the atmosphere due to the mass wasting of debris by supraglacial melt. These results exemplify the utility of high-resolution photogrammetry data in resolving cm-scale elevation changes on rock glacier surfaces from year to year.

To estimate the surface elevation change at Sulphur Creek, we calculated the difference between the $\frac{1}{3}$ arcsecond resolution (about 10 m/pixel) USGS 3DEP DEM surveyed in 1985 [41] and the 2020 airborne-derived DEM. The surface elevation change appears to be biased towards surface lowering, with a 0.315 km^2 section interpreted to be stable ground showing a mean difference of -4.9 ± 3.5 m, with the error here represented as one standard

deviation. However, three regions in the Sulphur Creek image display surface lowering that exceeds the bias in the difference calculated between the 1985 and 2020 DEMs. The first region (labeled "1" in Figure 9b) has a surface area of 0.072 km^2 and displays a mean surface elevation change of −18.3 ± 4.1 m. Region 1 in this map corresponds with the region exhibiting inward flow in the change detection results, and the combination of these observations suggests rapid stagnation and collapse of the middle section of Sulphur Creek, supporting the interpretation of [37]. Region 2 has a surface area of 0.085 km^2 with −23.9 ± 3.5 m of surface change, while Region 3 has a surface area of 0.141 km^2 with −27.9 ± 5.9 m of surface change.

Regions 2 and 3 correspond with the two small cirque glaciers occupying the two forks of the upper Sulphur Creek basin. Accounting for the bias in elevation change estimated from the off-glacier terrain, Regions 1, 2, and 3 of Sulphur Creek have experienced mean thinning rates of 38 ± 12 $\frac{cm}{yr}$, 54 ± 10 $\frac{cm}{yr}$, and 66 ± 17 $\frac{cm}{yr}$, respectively, over the 35-year DEM interval. These thinning rates indicate significant recent negative mass balance for the higher-elevation components of the Sulphur Creek system. We applied our simple thermal model here using a debris thickness of 0.5 along with SNOTEL data spanning the years 1990–2020; this model supports the result that Sulphur Creek has lost upwards of 20 m of ice to cumulative melt under a reasonable range of thermal conductivities for the debris (Appendix A). At these melt rates, the Sulphur Creek basin may lose the entirety of its glacial ice before 2100, and the only remaining subsurface ice in this basin will be preserved in an ice-cemented rock glacier. Future Wyoming fieldwork should aim to collect a UAS-derived DEM at Sulphur Creek to measure surface elevation change after the acquisition of the 2020 dataset and compare the results with the 1985–2020 surface elevation change rates as well as with the results from the neighboring Galena Creek.

In contrast to the Wyoming sites, the surface change between the earliest and latest datasets for the Alaska sites does not suggest broad patterns of elevation increase or decrease across the entirety of each rock glacier. Stationary regions near the rock glacier margins show a mean systematic bias of about +40 cm for the May 2014/July 2022 DEM pair for Sourdough (Figure 9c) and about +30 cm for the May 2014/June 2021 DEM pair for McCarthy Creek (Figure 9d). The mean systematic biases have corresponding standard deviations of about 50 cm for both rock glaciers. This estimate is complicated by the dense vegetation surrounding much of the rock glaciers' perimeters, meaning that stable bedrock estimations must be taken from locations with steep slopes, where the DEM error is likely the highest. There is not a clear change in the mean surface elevation change on either rock glacier surface compared to the surrounding stable terrain in the photogrammetric DEMs when compared with one another or when compared with the corresponding USGS 3DEP product. However, these elevation change results are similar to the Galena Creek results in that the variability of the surface change increases on the surface of the rock glaciers as opposed to off-glacier locations. This variability appears to be an effect of the translational motion of surface ridges and furrows, as the topographic oscillations are oriented perpendicular to flow while their wavelengths and velocities are generally out of phase with the timing of the data acquisition.

The translational motion of ridges can be observed by plotting elevation profiles from multiple flights. These profiles show that any thickness changes of the rock glacier are less than the vertical uncertainty in the elevation data, which is on the order of a few decimeters (Supplementary Figures S4 and S5). At Sourdough, there is a region of apparent thinning in its uppermost reaches corresponding with debris and avalanche cones, as well as a broad region of negative elevation change about 200 m wide on the lower lobe. The elevation change variability in the trunks of the Alaskan sites may include localized thinning that falls within the uncertainty of the elevation data; however, neither of the Alaskan sites indicate broadly consistent thinning across the surface. This result is supported by the thermal conduction model described in Appendix A. Localized elevation gain is observed near the toe of Sourdough as a result of its terminus advancing, which is corroborated by field observations of "bulldozed" trees.

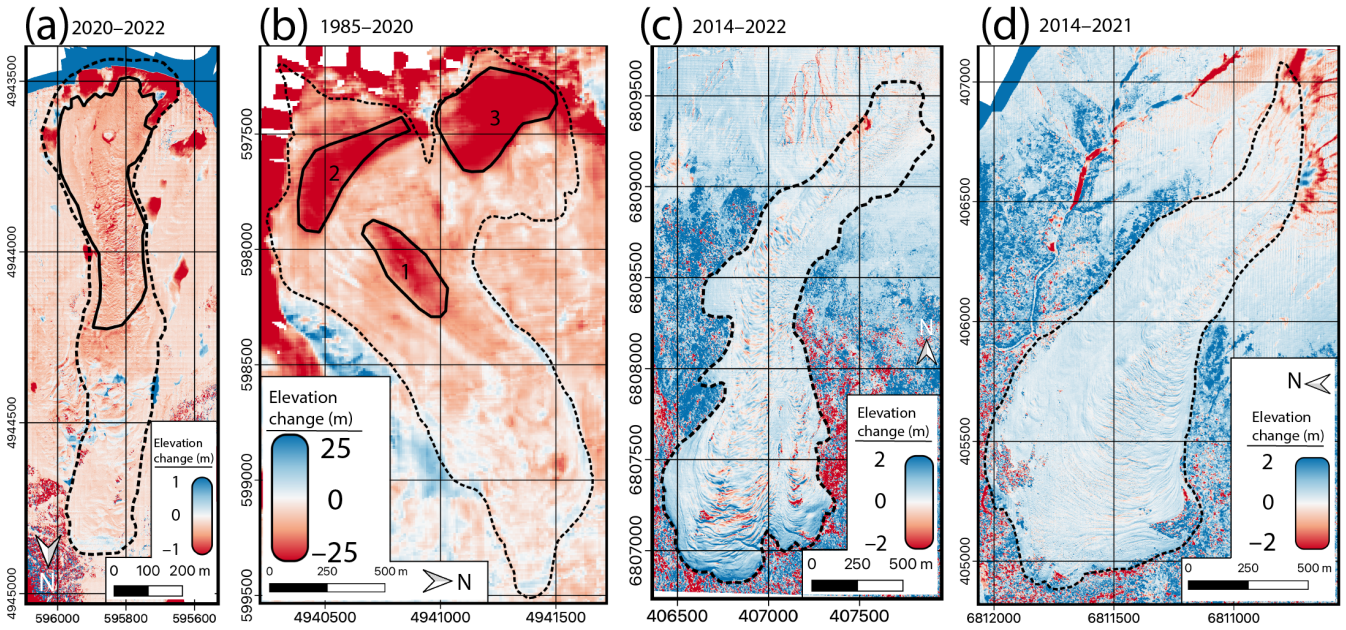

Figure 9. Surface elevation change results: (**a**) the August 2020/August 2022 UAS DEM pair for Galena Creek, with the region of increased ablation outlined in the solid black line; (**b**) the 1985 DEM from USGS 3DEP paired with the August 2020 airborne DEM for Sulphur Creek, where the regions labeled 1, 2, and 3 indicate areas of high thinning rates; (**c**) the May 2014/July 2022 airborne DEM pair for Sourdough; (**d**) the May 2014/June 2021 airborne DEM pair for McCarthy Creek.

In general, all of our rock glacier surface change maps exhibit indicators of longitudinal flow in agreement with the optical change detection results. Further, the Wyoming sites demonstrate clear signals of vertical thinning due to ice melt, with Sulphur Creek experiencing the fastest melt rate. The Alaska sites do not exhibit the same thinning signals. These trends are consistent with a thermal conduction model (Appendix A) using GPR-derived debris thickness measurements that show the debris to be thinnest at the upper part of Sulphur Creek and thickest at Sourdough [31]. Assuming similar mean annual air temperatures and constant thermal conductivities for the debris at all four sites, it is expected that the thinner debris at Sulphur Creek would lead to the highest melt rate, while the thick debris at the Alaska sites would inhibit melt to a greater degree. In the following section, we discuss the implications of these surface change results for the accumulation and evolution of each of these field sites; in addition, we further consider the sources of uncertainty in these results by defining criteria for assessing the accuracy of the horizontal and vertical surface change products.

4. Discussion

4.1. Validation and Uncertainty Analysis

The image pair collected with the UAS in both August 2020 and August 2022 shows a baseline velocity uncertainty of 6.8 $\frac{\text{cm}}{\text{yr}}$ (Table 3). This is the average value of the displacements returned from a subset of the CIAS results consisting of 320 points where bedrock is assumed to be motionless (Figure 3b). Examining the means of the vector components and their standard deviations provides information about the sources of uncertainty [45]. The mean x and y components of the UAS-derived velocity measurements at Galena Creek show that the systematic error is less than 1 cm. The standard deviations indicate that the random error is uniform in both directions and is comparable to the pixel size of the image. These values are similar to the results of photogrammetric change detection surveys in the Swiss Alps [46]. In comparison, the image pair using the coarser satellite image returned much higher uncertainty values due to the increase in mismatches leading to more noise in the results. Using repeated surface-based position measurements of marked

boulders at Galena Creek, we validate our change detection results with independent velocity measurements in consideration of the uncertainty of our remote sensing results. We compare the velocities measured from boulder positions in 2015 and 2022 with the four nearest UAS-derived velocity values over the 2020 to 2022 interval [38].

Table 3. List of image pairs used for velocity measurements and the associated velocity uncertainties measured using regions of stable terrain at each field site. All means and standard deviations reported here are provided in units of $\frac{\text{m}}{\text{yr}}$.

Site	Stable Terrain Area (m^2)	# of Points	Image Pair	Mean ($\lvert v \rvert$)	Mean (v_x)	Mean (v_y)	$\sigma(v_x)$	$\sigma(v_y)$
Galena Creek	8400	320	August 20 August 22	0.068	0.009	−0.006	0.109	0.103
	8400	320	July 21 August 22	5.65	−0.290	0.018	6.43	7.11
Sulphur Creek	11,550	111	August 20 August 22	0.104	0.010	−0.010	0.112	0.086
Sourdough	13,600	141	May 14 August 14	1.11	0.948	−0.011	0.877	0.519
	13,600	141	May 14 May 15	0.246	−0.147	0.029	0.229	0.106
	13,600	141	May 14 August 15	0.288	0.163	0.017	0.336	0.349
	13,600	141	May 14 June 16	0.208	−0.171	0.070	0.118	0.059
	13,600	141	May 14 August 16	0.466	−0.345	−0.250	0.114	0.198
	13,600	141	May 14 September 19	0.057	0.014	0.003	0.063	0.134
	13,600	141	May 14 May 20	0.105	−0.034	0.001	0.234	0.235
	13,600	141	May 14 October 20	0.259	−0.091	−0.112	0.356	0.373
	13,600	141	May 14 June 21	0.042	−0.004	−0.038	0.014	0.019
	13,600	141	May 14 July 22	0.091	−0.014	−0.051	0.135	0.154
McCarthy Creek	11,030	111	May 14 August 14	6.64	2.02	0.293	8.30	6.17
	11,030	111	August 14 May 15	0.470	0.006	0.018	0.612	0.721
	11,030	111	August 14 August 15	0.403	0.046	0.067	0.407	0.327
	11,030	111	August 14 June 16	1.31	−0.231	0.201	1.41	1.21
	11,030	111	August 14 September 19	0.086	0.033	0.004	0.235	0.155
	11,030	111	August 14 October 20	1.06	−0.043	−0.140	0.952	0.855
	11,030	111	August 14 June 21	0.078	0−0.021	−0.018	0.086	0.146

In the upper section of Galena Creek, the change detection and boulder position results are in good agreement, with a maximum velocity magnitude difference of about 5 $\frac{\text{cm}}{\text{yr}}$, similar to the baseline uncertainty in the August 2020/August 2022 CIAS results (Figure 10). On the lower third of the rock glacier, four measurements show a discrepancy of 10 $\frac{\text{cm}}{\text{yr}}$ or greater between the 2015–2022 boulder measurements and the 2020–2022 change detection measurements. The largest of these discrepancies (0.36 $\frac{\text{m}}{\text{yr}}$) can be explained by noise in the change detection data, where a patch of trees created a zone of mismatched pixel clusters at the location of the surface measurement. The three other points with discrepancies greater than 5 cm exhibit an anisotropic bias, where the change detection measurements are about 10 $\frac{\text{cm}}{\text{yr}}$ faster than the boulder point measurements; most of the variation occurs along the y-axis. This could indicate a rapid acceleration of the lower rock glacier lobe by 10 $\frac{\text{cm}}{\text{yr}}$ between 2015 and 2020, or could be an effect of errors in measurement and the coordinate system transformation of the boulder positions on this lower lobe between the 2015 and 2022 surveys. A coordinate rotation was applied to the 2015 points, and the boulders on the lower lobe are the most distant from the pole of rotation, making them the most susceptible to an error in the rotation angle between coordinate systems. The deviation between boulder displacements and CIAS results generally increases when using boulder position measurements from 1997 to 1999 (Supplementary Figure S6), which may be an effect of either a changing rock glacier surface velocity field or a decreased measurement error with newer global positioning technology.

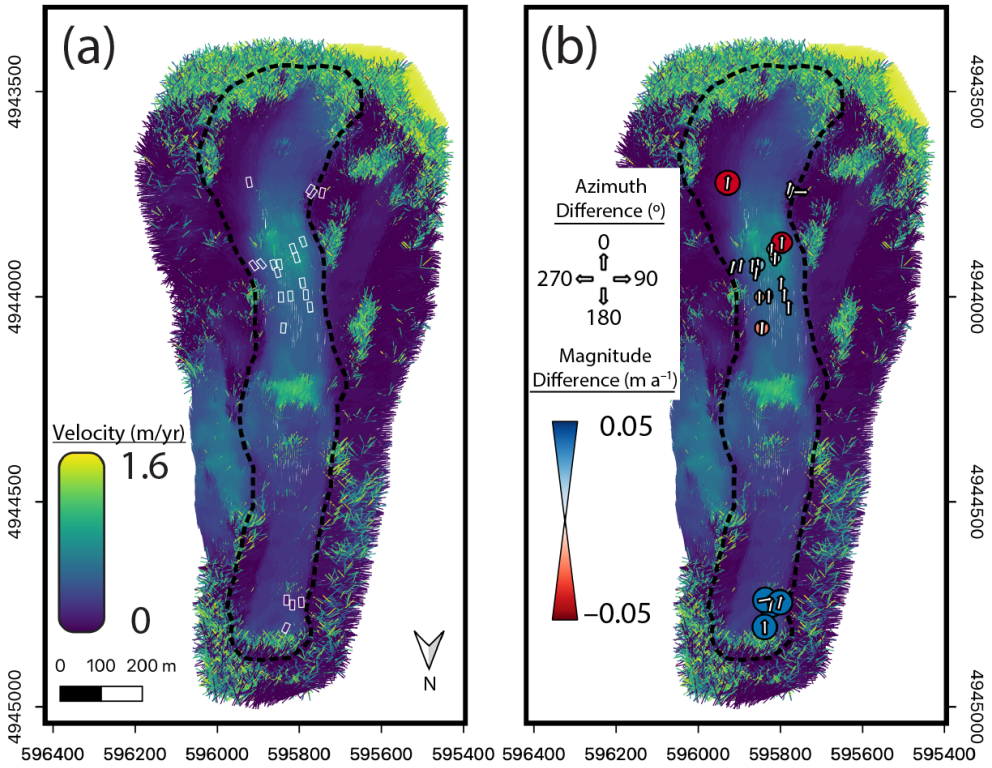

Figure 10. Comparison of photogrammetric change detection results between August 2020 and August 2022 UAS imagery with boulder velocities between August 2015 and August 2022 at Galena Creek. (**a**) The boulder velocity vectors are shown as rectangles with white borders, color-coded according to velocity magnitude and oriented according to the vector's direction; these boulder velocities are plotted over the automated change detection results using the same color scale. (**b**) The difference in magnitude and azimuth between the measured boulder velocities and the four nearest grid points in the change detection measurements. The size and color of each dot in (**b**) corresponds to its magnitude and sign and the direction of the arrow indicates the difference in vector azimuth, meaning that vectors with no change in azimuth display an arrow that faces directly upwards.

Although the airborne photogrammetry at the Alaska sites provides a clear signal of flow on both rock glaciers, uncertainty estimation using stable bedrock points is complicated by forest cover surrounding most of the perimeters of Sourdough and McCarthy Creek. The seasonally changing tree canopy provides poor references for the change detection algorithm, and this leads to mismatched and noisy results immediately surrounding the rock glacier. As we have no repeated surface-based boulder measurements for the Alaska sites, we examine the uncertainty in our change detection measurements here using two metrics: the range of peak velocities across a transverse profile, and the average minimum velocity on stable ground.

The first measure used to characterize the velocity uncertainty for the change detection results is the range in the magnitude of the peak velocities measured along a common transverse profile on the rock glacier surface for all of the time intervals examined. This range is about 0.4 $\frac{\mathrm{m}}{\mathrm{yr}}$, though this variability estimation may contain variations in the rock glacier's true velocity field during the measurement period. The second quantification of the uncertainty in measured velocity for each image pair is calculated by averaging a subset of low-magnitude displacement vectors selected at regions of the image interpreted to be bare stable ground. This value represents the minimum apparent velocity between stationary points in two images; therefore, we take these values as a representation of the uncertainty for the on-glacier velocity.

The averaged minimum velocity magnitudes of stable terrain are variable for the Sourdough image pairs, generally varying around a value of approximately 20 $\frac{\mathrm{cm}}{\mathrm{yr}}$. There

is a trend of decreasing uncertainty with increasing time interval between image, though other factors such as a warped orthomosaic (August 2016) or a snow-covered surface (October 2020) contribute to these uncertainty values. Because the standard deviations of the vector components are generally random random, showing that there is no directional bias to these minimum velocity values, the value of ±20 $\frac{cm}{yr}$ (total range of 40 $\frac{cm}{yr}$) agrees with the range of 40 cm measured from the difference between the velocity peaks along a common profile for all image pairs. Therefore, we assume the random error in the Alaskan airborne datasets to be approximately ±20 $\frac{cm}{yr}$, while the systemic error approaches values less than 5 $\frac{cm}{yr}$, especially for longer time intervals.

Systematic biases likely exist in local regions of the individual image pairs. For example, in the May 2020/June 2021 image pair, the lower lobe of the rock glacier exhibits a velocity magnitude much greater than the magnitudes at the same area in the other image pairs, where the velocity decreases with proximity to the terminus (Figure 6). We suggest that this systematic bias in the May 2020/June 2021 image pair results from effects in the photogrammetric processing step, which could have led to geometric warping of the orthomosaics. The processing reports generated by the Agisoft Metashape software indicate that these two images had the highest percentage of regions on the rock glacier where the image overlap was less than nine (see the supplementary materials for the processing reports), which supports the hypothesis that the systematic error in this image pair is due to artifacts from the photogrammetric processing. Additionally, nonzero means of stable terrain velocity magnitudes combined with unequal standard deviations are indicative of systematic and/or nonuniform uncertainty distributions, such as that of the May 2014/June 2016 image pair at Sourdough (Table 3). Future studies should visually identify regions that may contain warping of the orthomosaic and the associated increase in uncertainty in order to avoid misinterpretation of the physical implications of the velocity field.

To further understand the relative quality of the change detection results for different image pairs, we examined the distributions of output velocities and maximum correlation coefficients for Sourdough and Galena Creek. We used the eight image pairs at Sourdough to examine the characteristics of velocity and correlation coefficient distributions. Qualitatively, one way to compare velocity measurements for different image pairs is to compare the tails of the distribution, where the output velocity is greater than the highest expected real velocity (about 2 $\frac{m}{yr}$ for Sourdough). For example, the August 14/August 2015 results for Sourdough have fewer outlying velocity values than those for May 14/May 15 (Figure 11). In Figure 6, it can be observed that the velocity field for August 2014/August 2015 has a lower baseline uncertainty than for May 14/May 15, leading to the conclusion that the quality of the results can partially be characterized by the number of outlying velocity magnitudes. These observations can be used to weight the velocity vector fields of specific image pairs during future kinematic analyses.

The distributions of the maximum correlation coefficients output by the CIAS algorithm provide another assessment of the reliability of the results for each image pair. These histograms (Figure 12) show a relationship between the width of the distribution of the maximum correlation coefficients and the quality of the change detection results. Two of the highest quality velocity fields as assessed by baseline uncertainty and flow signal continuity are August 2014/August 2015 and August 2016/September 2019. These two image pairs return the narrowest distribution of the maximum correlation coefficients. On the other hand, May 2014/May 2015 and September 2019/October 2020 have relatively low quality results, and broader distributions of the maximum correlation coefficients are observed. This effect is especially apparent for the September 2019/October 2020 pair.

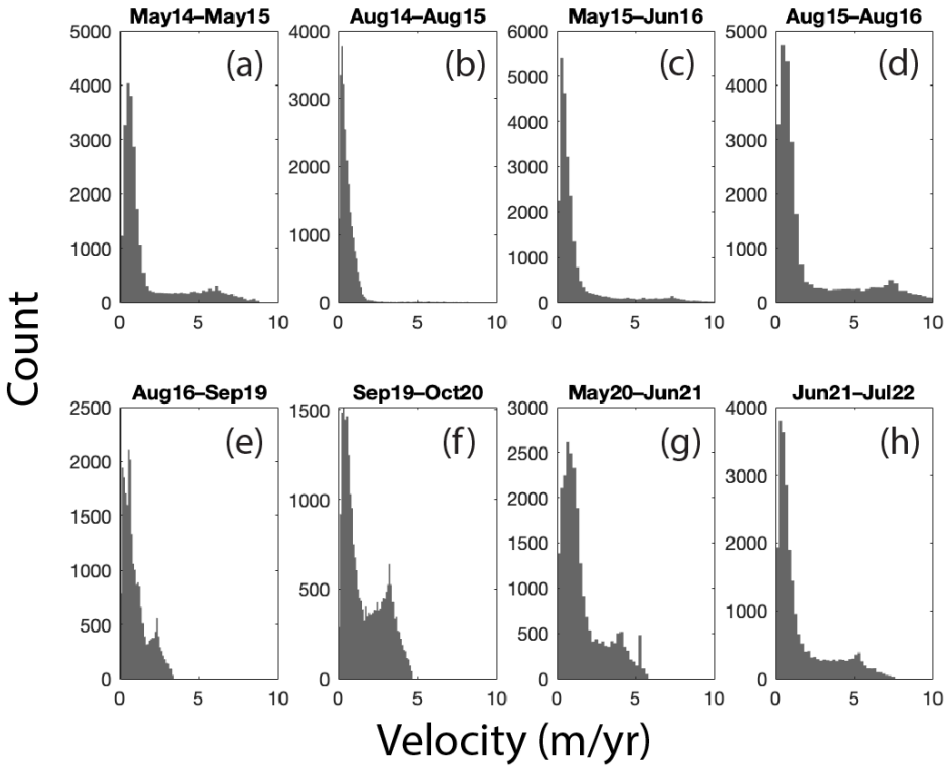

Figure 11. Histograms showing the distribution of velocity magnitudes for each image pair at Sourdough with a time interval of one year or longer. Each panel (**a**–**h**) corresponds with the results presented in the same panel labeled in Figure 6.

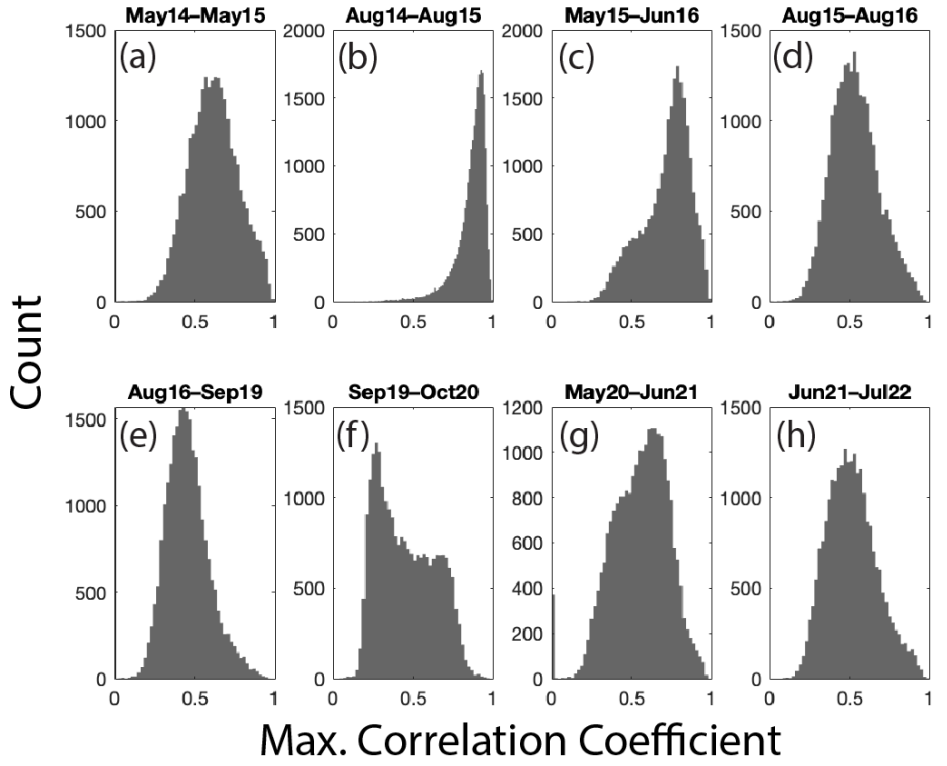

Figure 12. Histograms showing the distribution of the maximum correlation coefficients for each image pair at Sourdough with a time interval of one year or longer. Each panel (**a**–**h**) corresponds with results presented in the same panel labeled in Figure 6.

We tested these hypotheses with regard to the relationships between the number of outlying data points, the maximum correlation coefficient distribution, and the quality of change detection results by plotting the histograms for the August 2020/August 2022 image pair and the July 2021/August 2022 image pair at Galena Creek. Because the both the August 2020 and Augusut 2022 images were acquired using the UAS, the velocity field derived from this image pair has a low baseline uncertainty and a low amount of noisy regions in the velocity field. In comparison, the July 2021 image is a lower resolution and lower precision satellite product, leading to a higher baseline uncertainty and noise value for the July 2021/August 2022 velocity field. The distributions for Galena Creek (Figure 13) support our hypothesis that the velocity field quality can be characterized by both the size of the tail of outlying velocity magnitudes and the width of the distribution of the maximum correlation coefficients. In the case of the higher quality image pair at Galena Creek (August 2020/August 2022), the distributions contain a lower number of velocity magnitudes greater than 2 $\frac{m}{yr}$ and the peak of the maximum correlation coefficient distribution is narrower in comparison with the July 2021/August 2022 pair. Our observations of uncertainty patterns in the change detection results can be used to assess the propagation of error for future analyses using the velocity fields presented here. Evaluating the benefits and limitations of UAS, airborne, and satellite imaging platforms in regard to the measurement of rock glacier surface motion will contribute to the planning requirements of ongoing and future data acquisition campaigns [46,47].

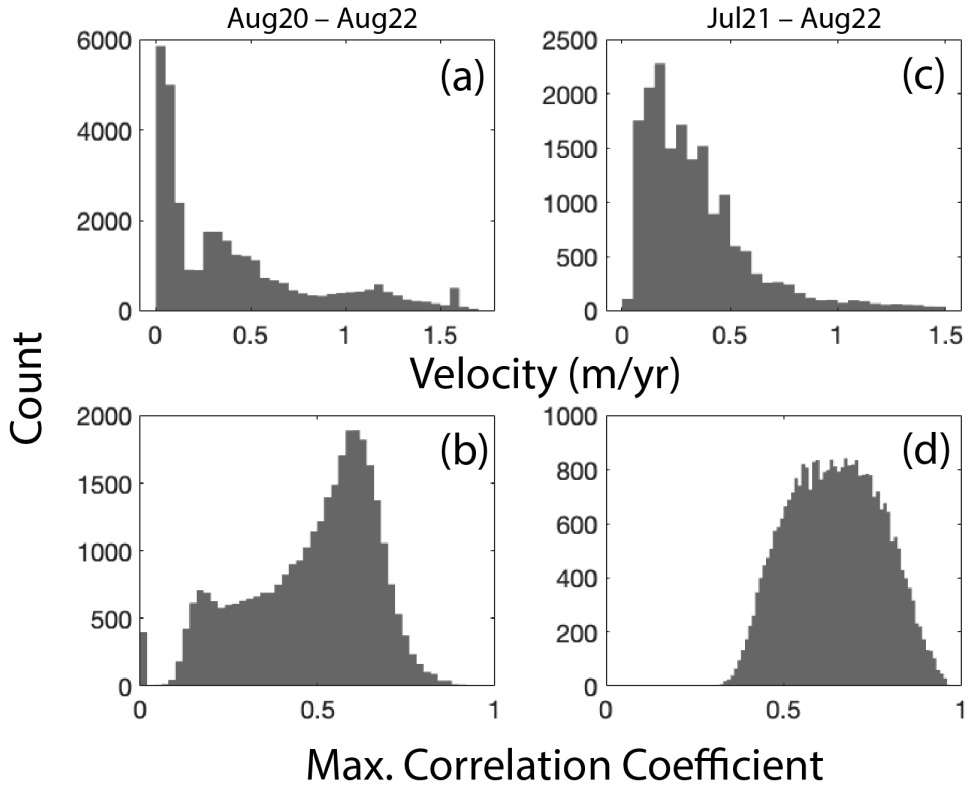

Figure 13. Histograms showing the distributions of velocity magnitude (**a**) and maximum correlation coefficient (**b**) for the August 2020/August 2022 image pair at Galena Creek and the velocity magnitude (**c**) and maximum correlation coefficient (**d**) for the July 2021/August 2022 hybrid image pair at Galena Creek.

4.2. Interpreted Flow History

The timescale required to transport a debris clast from the head of the glacier to the toe can estimated using the measured velocity fields, providing an estimate for the age of initial rock glacier accumulation. To obtain the age A_x at distance x from the rock glacier headwall, we integrate a smoothed profile of the inverse of calculated velocity magnitudes v_x (moving average window width = 5 pixels) along the central flowline for each rock glacier:

$$A_x = \int_0^x v_x^{-1}\, dx. \quad (1)$$

This method assumes a time-invariant velocity field along an interpreted flow path. The velocity field for Galena Creek has likely been dependent upon surface slope throughout its history, as it is today (Figure 14a); if the rock glacier was previously thicker and flowed faster due to higher driving stress, then our assumption of a constant velocity field would provide an upper bound for the age of the ice along the profile. Integrating the surface velocity profile of Galena Creek produces a terminus age of 3070 years (Figure 14a). This age falls between the estimated early neoglacial advance in Wyoming about 4000 years ago and the Audubon advance approximately 2000 to 1000 years ago [28]. Assuming that our age estimate is an upper bound, our results are most consistent with the rock glacier terminus of Galena Creek originating from the Audubon advance, while the debris-covered glacier comprising the upper two-thirds of the Galena Creek system contains ice that accumulated during the Little Ice Age (LIA), which spanned approximately the last half-millennium in the American Cordillera [48]. It is likely that this LIA advance interacted with the pre-existing rock glacier system, similarly to other landforms observed in the Swiss Alps and Chilean Andes [32–34]. This interaction of glacier ice and permafrost resulted in the complex topography and variable ice distribution found at the inflection in topography where they presently meet [31].

Our Galena Creek age profile is consistent with two calibrated radiocarbon measurements in leaf fragments at locations along the center flowline of Galena Creek (Figure 14a) [12]. The radiocarbon age acquired 100 m from the cirque headwall is 0–310 calendar years before present, and our velocity-derived age at this location is 180 years. Similarly, the radiocarbon age 800 m along the flow profile is 1410–1730 years before present, while the velocity-derived age is 1450 years. These independent measurements suggest that our method of age estimation is suitable for Galena Creek, where the low width/thickness ratio has allowed the velocity field to remain relatively consistent throughout the recent history of the rock glacier. Although Sulphur Creek is a close neighbor to Galena Creek, we did not perform a velocity profile analysis here, as the mid-glacier displacement vectors and elevation change since 1985 indicate substantial stagnation and surface subsidence in the past few decades, increasing the width/thickness ratio and likely invalidating the assumption of a time-invariant velocity field over the past few centuries.

We used the velocity profiles for three of the highest quality change detection results for Sourdough (August 2014/August 2015, August 2016/September 2019, and May 2014/July 2022) to better understand the propagation of uncertainty in the change detection results to the rock glacier age estimates (Figure 14b). The three profiles show rock glacier terminus ages ranging between 3,310 and 3,540 years. This range of ages is roughly consistent with the oldest of four late Holocene advances inferred from radiocarbon and tree ring dates [49], and although this indicates that these sites are older than the LIA, this result does not support the hypothesis that the ice in this population of rock glaciers in the Wrangell Mountains is related to the advance of the last glacial maximum (LGM), generally considered to be much more than 10,000 years ago.

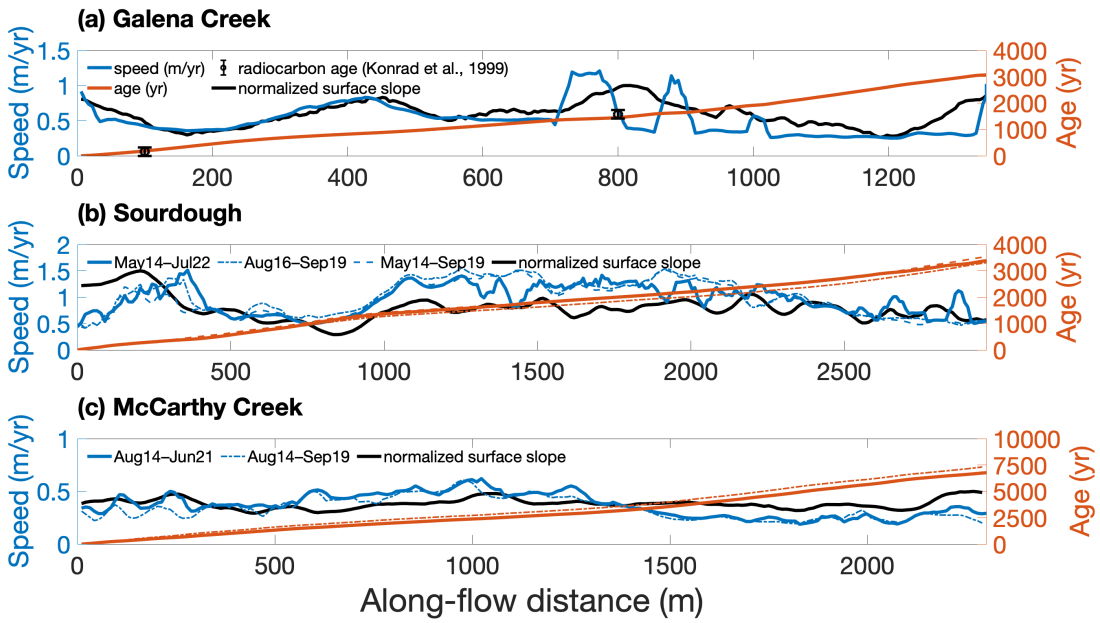

Figure 14. Velocity magnitudes (blue), age profiles (red), and normalized surface slopes (black) for (**a**) Galena Creek, including calibrated radiocarbon ages from [12] along the flow profile, (**b**) Sourdough, and (**c**) McCarthy Creek.

McCarthy Creek, just 2 km north of Sourdough, has a maximum velocity that is a factor of two less than that of Sourdough while covering a relatively similar length (Figure 14c). Using the August 2014/June 2021 velocity results for McCarthy Creek, which is the longest time interval without surface obfuscation due to snow, the estimated terminus age is approximately 6680 years. The August 2014/September 2019 image pair yields another high quality velocity field, and returns an age estimate of 7330 years. This range is about double the estimated age for Sourdough. Although this is an older age range, it is not consistent with an advance related to the LGM. While there is uncertainty in the exact path of a surface particle in comparison with our estimated flowline profiles, we do not expect this potential source of error to be the primary cause of the factor-of-two difference in the age calculations. Instead, this difference in estimated age for the two neighboring rock glaciers suggests the existence of local heterogeneities in rock glacier evolution, even if we assume that they are both related to the documented late Holocene ice advances in the Wrangell Mountains.

Heterogeneities in rock glacier evolution could influence variance in the surface velocity fields over time, refuting this age estimation's assumption of a time-invariant velocity field. Possible sources of differing velocity field evolution between the northward-flowing McCarthy Creek and southward-flowing Sourdough include the effect of slope aspect on accumulation and surface temperature as well as different series of rock glacier surges overriding less active older lobes. For example, if McCarthy Creek is in the process of stagnating while Sourdough's activity remains constant, our method would estimate an older age for McCarthy Creek due to the implication that slower surface velocities take longer to transport surface material along the length of the rock glacier. One possible line of evidence for a velocity field that has changed over time is the morphology and velocity distributions of the different lobes at Sourdough and McCarthy Creek. Sourdough consists of one major active lobe, where the peak velocity occurs within the steep trunk of the rock glacier, and one smaller active lobe to the east, where the velocity appears to be correlated to the surface slope as well. The western flank of Sourdough has two small steep lobes which are presently inactive (Figure 1a). These minor lobes are interpreted to be remnant overflow deposits from a past rock glacier advance when its thickness was greater than at present, indicating that this zone of maximum velocity has likely been correlated with

the steep trunk of the rock glacier throughout its history. Even though the age estimate for Sourdough is taken to be an upper bound, we assume the relative velocities along its longitudinal profile have maintained similar trends in correlation with surface slope.

By contrast, McCarthy Creek consists of a large stagnant lobe to the north of the main active lobe, where the peak velocity is half that of Sourdough and which is found at the upper reaches of the rock glacier as opposed to the mid-glacier trunk, as it is at Sourdough. Sourdough is not substantially steeper than McCarthy Creek. In addition, McCarthy Creek displays no overflow lobes, suggesting that its movement may be more limited by its bedrock geometry and that the velocity field may be more susceptible to decreases in ice accumulation. Because the northern lobe of McCarthy Creek is presently stagnant and the peak velocity appears to have a lower correlation with surface slope (Figure 14c), it may be reasonable to assume that the northern lobe was previously more active and that the peak velocity would have been greater at the high slope regions on the rock glacier when the ice unit was thicker. All of these observations support the inference that McCarthy Creek has slowed over time, implying an overestimate of its total age; however, further work is needed to determine whether these differences in evolution between Sourdough and McCarthy Creek stem from heterogeneities in ice accumulation, debris input, valley geometry, the effects of slope aspect on insolation, or a combination of these processes.

In both Alaska and Wyoming, neighboring rock glaciers exhibit differences in flow rate distribution, suggesting that certain local controls may be influencing each rock glacier's evolution. As discussed above, the Alaskan rock glaciers differ significantly in their maximum flow speed, with Sourdough approaching 1.5 $\frac{\mathrm{m}}{\mathrm{yr}}$ and McCarthy Creek never exceeding 0.6 $\frac{\mathrm{m}}{\mathrm{yr}}$. Additionally, in Wyoming, Galena Creek's flow direction correlates with the down-valley topographical gradient and the flow velocity magnitude correlates with the magnitude of the longitudinal surface slope. Conversely, neighboring Sulphur Creek's velocity magnitude is greatest at the toe, and does not appear to be correlated with the longitudinal surface slope. The middle section of the glacier appears to be flowing perpendicular to the down-valley topography rather than parallel to it. This observation, combined with significant surface subsidence and a measured ice thicknesses of only about 10 m at this same location [31], reveals a recent rapid destabilization of the debris-covered ice in the upper Sulphur Creek basin. Although Galena Creek exhibits surface lowering as well, a comparison of its velocity-derived age with radiocarbon ages suggests no major deviations between its past and present velocity fields.

5. Conclusions

Our analysis demonstrates the capabilities and limitations of using multiple combinations of repeated imagery acquisition methods to perform photogrammetric change detection as a means of measuring rock glacier surface motion. The imagery acquired with the Phantom 4 RTK UAS had the highest success rate for detecting rock glacier surface flow due to this method's high image resolution and positioning accuracy. This effect is most apparent for the August 2020/August 2022 image pair at Galena Creek, Wyoming, where both images were acquired with the UAS. With this image pair, a strong flow signal was detected with a baseline measurement uncertainty of approximately 5 $\frac{\mathrm{cm}}{\mathrm{yr}}$. Airborne photogrammetry successfully detects rock glacier surface motion over annual time intervals, although the slightly diminished resolution and positioning accuracy due to the increased flight speed and altitude can propagate to the change detection results in comparison with the UAS-derived datasets. At each Alaska site (Sourdough and McCarthy Creek), strong flow signals were detected across the rock glacier surface with airborne imagery, especially for imaging intervals of three years or longer. The baseline uncertainty (20 $\frac{\mathrm{cm}}{\mathrm{yr}}$) is higher with the airborne method than that for image pairs where both images were acquired with the UAS.

While high-resolution satellite imagery provides the potential for consistent monitoring of rock glaciers, there is a tradeoff between this logistical convenience and the limitations of resolution and positioning for civilian data acquired from an orbital platform.

All of the orbital imagery used in this study required manual repositioning to improve co-registration with the images they were paired with, and the relatively coarse resolution limited the lower bound of the annual displacement magnitudes detectable by this method in comparison with the UAS and airborne platforms. The satellite imagery for both Wyoming field sites detected flow signals when paired with UAS and airborne data; however, the baseline uncertainty (40 cm) and the number of spurious displacement vectors caused by feature mismatches in the change detection were both the highest for all of the methods used.

A preliminary analysis of the rock glacier velocity fields shows that all of the study sites in Alaska and Wyoming likely originated during the early to middle Holocene, after the LGM and before the LIA. In addition to horizontal change detection, we used a combination of digital elevation models that are publicly available or generated with our photogrammetric processing method to estimate current thinning rates for each site. We found that both Wyoming sites exhibit a thinning signal that is consistent with the meteorological data and measured debris thickness, while neither of the the Alaska sites exhibits surface elevation change consistent with rock glacier thinning.

Due to the slow flow of rock glaciers in comparison with glaciers, all of the imagery applied to change detection experiments must have high-precision positioning information to reduce measurement error and detect a flow signal, especially when the time sampling interval is one year or less. This level of precision is vital for future studies focusing on remote sensing of seasonal patterns in rock glacier flow. With current technological resources, UAS imagery has the best resolution and positioning; however, it is limited to small spatial footprints at locations and times where the target is directly accessible. While airborne imagery provides a broader spatial extent and greater ease of data acquisition at regular time intervals for less accessible sites, it sacrifices resolution and precision. Satellite imagery offers a solution for regularly sampling a wide spatial area multiple times per year; however, the presently available data lack the resolution and precise positioning needed to achieve the lower uncertainty levels of UAS or airborne imagery. Increasing the number of high-resolution satellite imaging constellations for environmental studies would further improve the spatial and temporal capability to measure and monitor rock glaciers. We intend for the results of this study to be analyzed further using established glaciological principles, and our observations relating to the application of multi-platform change detection should be considered when planning campaigns to measure rock glacier surface motion.

Supplementary Materials: The following supporting information can be downloaded at: https://www.mdpi.com/article/10.3390/rs15194779/s1. Figure S1: Workflow diagram showing the methodology for combining UAS, airborne, and satellite data to measure each rock glacier's horizontal displacement and elevation change. Figure S2: Sourdough change detection using May 2014 base image. Figure S3: Galena Creek elevation change profile. Figure S4: Sourdough elevation profiles. Figure S5: McCarthy Creek elevation profiles. Figure S6: Surface boulder velocity measurements from 1997–2022 and comparison with remote change detection results.

Author Contributions: Conceptualization, all authors; methodology, all authors; software, T.M.M., R.A. and E.I.P.; validation, T.M.M. and R.A.; formal analysis, T.M.M., R.A. and E.I.P.; investigation, C.F.L., M.S.C., R.A., J.W.H., E.I.P. and T.M.M.; resources, J.W.H. and C.F.L.; data curation, C.F.L., M.S.C., R.A. and T.M.M.; writing—original draft preparation, T.M.M., R.A., E.I.P. and M.S.C.; writing—review and editing, all authors; visualization, T.M.M., E.I.P. and R.A.; supervision, J.W.H., J.S.L. and C.F.L.; project administration, J.W.H., J.S.L. and C.F.L.; funding acquisition, J.W.H., J.S.L. and C.F.L. All authors have read and agreed to the published version of the manuscript.

Funding: This research was funded by the NASA Solar System Workings program, grant number 80NSSC19K0561.

Data Availability Statement: The photogrammetry data, processed orthomosaics, DEMs, photogrammetric processing reports, horizontal change detection results, vertical elevation difference products, surface-based boulder position measurements, and the associated analysis code are openly available from the University of Arizona Research Data Repository (ReDATA) with the following DOI: https://doi.org/10.25422/azu.data.23272220.

Acknowledgments: We thank Kestrel Aerial Services for collecting the Wyoming airborne data presented here. This work utilized SkyMap50 satellite data made available through Soar. Extreme gratitude is felt for the field assistance provided by Brandon Tober, Stefano Nerozzi, Michael Daniel, and Rishi Chandra at the Wyoming sites and by Stefano Nerozzi, Tyler Kuehn, Victor Devaux-Chupin, and Bruno Belotti at Sourdough, Alaska. Many thanks to Noel Potter, Jr. and Noel Lewis Potter for sharing their boulder position data and for their valuable discussion regarding the history of exploration and glaciological research at the Wyoming field sites. Eric Yould provided essential logistical support throughout the years at the Alaska field sites. Thank you to three peer reviewers, whose comments and suggestions greatly improved this manuscript.

Conflicts of Interest: The authors declare no conflict of interest.

Abbreviations

The following abbreviations are used in this manuscript:

CIAS	Correlation Image Analysis Software
GNSS	Global Navigation Satellite System
GPR	Ground-Penetrating Radar
GDAL	Geospatial Data Abstraction Library
UAS	Uncrewed Aerial System
DEM	Digital Elevation Model
GCP	Ground Control Point
CP	Check Point
RMS	Root Mean Square
RTK	Real-Time Kinematic
LIA	Little Ice Age
LGM	Last Glacial Maximum
SNOTEL	Snowpack Telemetry

Appendix A. Thermal Conduction Model

To validate the remotely measured values of surface elevation change, we applied a simple melt model via 1D thermal conduction through the supraglacial debris layer. The objective of this model is to calibrate a realistic value for the thermal conductivity of the debris using the thinning rate measured with differenced DEMs at Galena Creek alongside temperature and snow depth data from the *Evening Star* meteorological station, which belongs to the SNOTEL network operated by the United States Department of Agriculture (station ID = 472). This station is located in the adjacent valley to the east of Galena Creek.

Using the SNOTEL data between the dates of 23 August 2020, and 8 August 2022, the melt rate was fixed to zero for dates with nonzero snow depth. For dates with zero snow, the melt rate ($\frac{\mathrm{m}}{\mathrm{day}}$) is provided by the following:

$$M = k\frac{dT}{dz}\frac{86{,}400}{\rho_{ice}L_f}, \tag{A1}$$

where k is the thermal conductivity of the debris layer, dT is simplistically assumed to be the SNOTEL air temperature measurement (T_{ice} = 0 °C), dz is the thickness of the debris layer, ρ_{ice} is the density of the ice (900 $\frac{\mathrm{kg}}{\mathrm{m}^3}$), and L_f is the latent heat of fusion (334,000 $\frac{\mathrm{J}}{\mathrm{kg}}$) [50]. For Galena Creek, we assume the debris thickness to be 1.5 m based on previous ice exposure observations and GPR measurements [1,3,31]. We test thermal conductivity values spanning the range of 0.3–1.8 $\frac{\mathrm{W}}{\mathrm{mK}}$, which is a feasible range for supraglacial debris, although it is likely that rock glacier debris resides on the lower end of this range due to its relatively high porosity [51,52]. The interpreted result of 20 cm cumulative melt during the

2020–2022 interval for Galena Creek is consistent with a thermal conductivity of 0.42 $\frac{W}{mK}$, approaching the lower bound of the plausible range (Figure A1b).

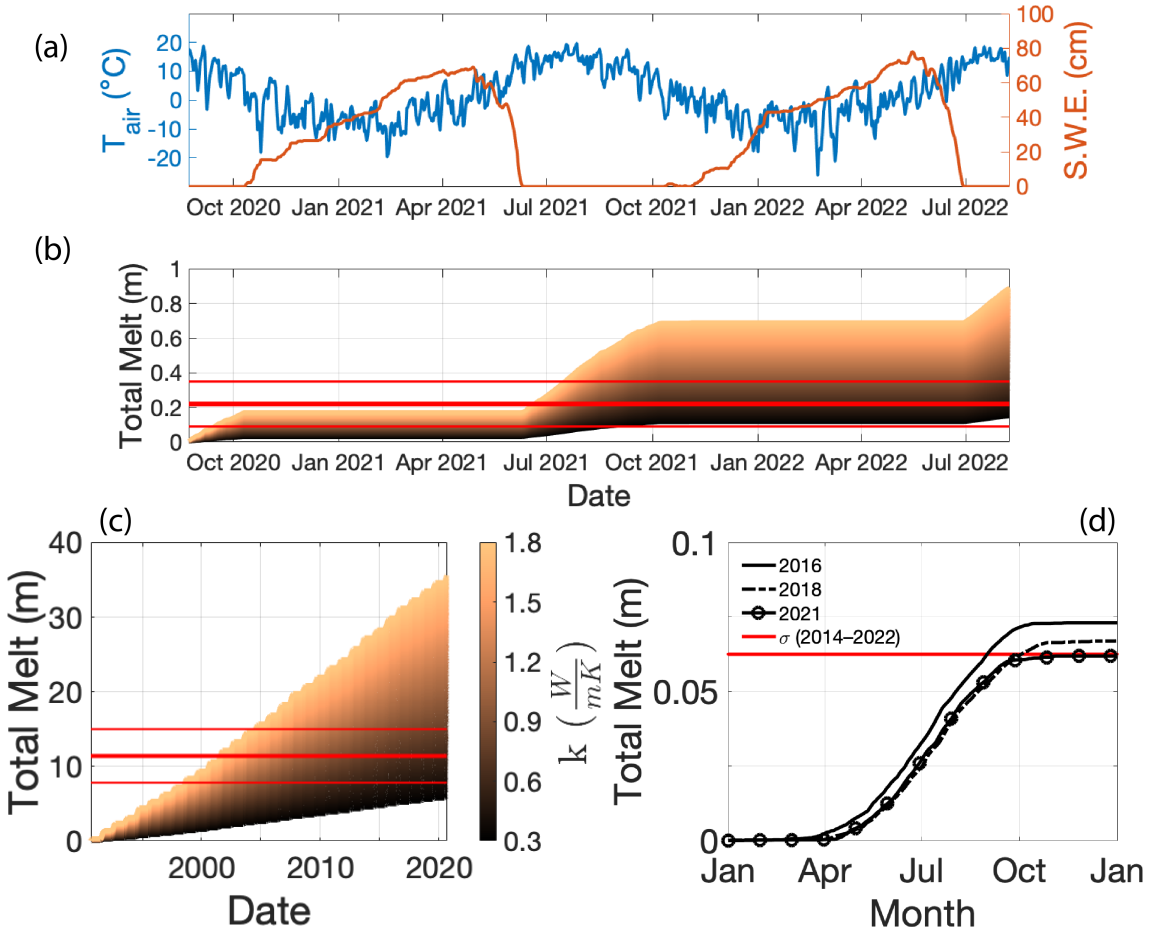

Figure A1. (**a**) Air temperature and snow water equivalent (SWE) data reported for the *Evening Star* SNOTEL site between 23 August 2020, and 8 August 2020. (**b**) Modeled melt over that same time interval for a range of possible thermal conductivity values for the debris layer and a debris thickness of 1.5 m. The horizontal red lines indicate the mean (thick line) and standard deviation (thin lines) of the photogrammetrically measured elevation change at upper Galena Creek. (**c**) Modeled melt using the *Evening Star* SNOTEL data between 1 September 1990, and 1 September 2020 for a debris thickness of 0.5 m as measured at upper Sulphur Creek in August 2020. The horizontal red lines indicate the expected mean (thick line) and standard deviation (thin lines) of the cumulative melt for that time period using melt rates measured between 1985 and 2020. (**d**) Modeled melt for Sourdough using air temperatures measured by an automated weather station near the rock glacier's toe, assuming a value of 3 m for the debris thickness and a thermal conductivity of 0.42 $\frac{W}{mK}$. The red line shows the standard deviation of the annual elevation change rate measured photogrammetrically between 2014 and 2022.

We applied the same thermal conduction model to the *Evening Star* SNOTEL data for the dates between 1 September 1990 and 1 September 2020 using a debris thickness of 0.5 m in order to test the remotely sensed cumulative surface lowering of between 18–28 m for upper Sulphur Creek over the 1985–2020 time interval. Although the SNOTEL data lack five years of data in comparison with the DEM interval, the thermal conduction results support the observation that upper Sulphur Creek thinned at a rate of tens of cm per year over three decades for plausible conductivities of the debris (Figure A1c), leading to cumulative melt well over 10 m for that period, further validating our photogrammetric results for Sulphur Creek.

We additionally tested the result of negligible surface elevation change for Sourdough and McCarthy Creek with the thermal conduction model using air temperature data acquired from an automated weather station on the lower lobe of Sourdough. Due to gaps in field campaigns, only the years 2016, 2018, and 2021 contained a complete and continuous calendar year of temperature data. We calculated the melt at Sourdough during each of these years using dz = 3 m and k = 0.42 $\frac{\mathrm{W}}{\mathrm{mK}}$ (Figure A1d). Each of these years returns melt rates less than 10 $\frac{\mathrm{cm}}{\mathrm{yr}}$. Further, these melt rates are likely overestimates, as this weather station does not measure the presence of snow; thus, this conditional step is removed from the melt rate calculation. Removing the condition that the melt rate equals zero when the snow depth is greater than zero leads to an increase in the estimated melt rates for both Galena Creek and Sulphur Creek by a factor of approximately 1.3. After correcting the Sourdough melt rates for this factor, the resulting these rates are within about 1 $\frac{\mathrm{cm}}{\mathrm{yr}}$ of the standard deviation of the 2014–2022 elevation difference product.

Additionally, the location of the weather station at the toe of the rock glacier may bias this calculation towards higher melt rates, as its elevation at the bottom of the rock glacier implies that it has the highest temperature on the surface of the rock glacier assuming normal atmospheric lapse rates. In addition to the uncertainty in the temperature change with increasing elevation and the relationship of the air temperature to the debris surface temperature, this thermal conduction model is subject to uncertainties in the debris thickness. Although the meteorological data indicate that melt may be occurring at Sourdough and McCarthy Creek, the surface change due to this melt falls within the measurement uncertainty of the DEMs used to calculate the surface change over the 2014–2021 interval for McCarthy Creek and the 2014-2022 interval for Sourdough. Future refinement of rock glacier melt rate estimates should consider the effects of nonconductive heat fluxes [52].

References

1. Potter, N. Ice-Cored Rock Glacier, Galena Creek, Northern Absaroka Mountains, Wyoming. *Geol. Soc. Am. Bull.* **1972**, *83*, 3025–3057. [CrossRef]
2. Anderson, R.S.; Anderson, L.S.; Armstrong, W.H.; Rossi, M.W.; Crump, S.E. Glaciation of alpine valleys: The glacier–debris-covered glacier–rock glacier continuum. *Geomorphology* **2018**, *311*, 127–142. [CrossRef]
3. Petersen, E.I.; Levy, J.S.; Holt, J.W.; Stuurman, C.M. New insights into ice accumulation at Galena Creek Rock Glacier from radar imaging of its internal structure. *J. Glaciol.* **2019**, *66*, 1–10. [CrossRef]
4. Wahrhaftig, C.; Cox, A. Rock glaciers in the Alaska Range. *Geol. Soc. Am. Bull.* **1959**, *70*, 383–436. [CrossRef]
5. Haeberli, W.; Hallet, B.; Arenson, L.; Elconin, R.; Humlum, O.; Kääb, A.; Kaufmann, V.; Ladanyi, B.; Matsuoka, N.; Springman, S.; et al. Permafrost creep and rock glacier dynamics. *Permafr. Periglac. Process.* **2006**, *17*, 189–214. [CrossRef]
6. IPA Action Group; Rock Glacier Inventories and Kinematics (RGIK). Towards Standard Guidelines for Inventorying Rock Glaciers: Baseline Concepts (Version 4.2.2). Available online: www.rgik.org (accessed on 20 April 2023).
7. Kääb, A.; Vollmer, M. Surface Geometry, Thickness Changes and Flow Fields on Creeping Mountain Permafrost: Automatic Extraction by Digital Image Analysis. *Permafr. Periglac. Process.* **2000**, *11*, 315–326. [CrossRef]
8. Outcalt, S.I.; Benedict, J.B. Photo-Interpretation of two Types of Rock Glacier in the Colorado Front Range, U.S.A. *J. Glaciol.* **1965**, *5*, 849–856. [CrossRef]
9. White, S.E. Rock Glacier Studies in the Colorado Front Range, 1961 to 1968. *Arct. Alp. Res.* **1971**, *3*, 43–64. [CrossRef]
10. Francou, B.; Reynaud, L. 10 year surficial velocities on a rock glacier (Laurichard, French Alps). *Permafr. Periglac. Process.* **1992**, *3*, 209–213. [CrossRef]
11. Berthling, I.; Etzelmüller, B.; Eiken, T.; Sollid, J.L. Rock glaciers on Prins Karls Forland, Svalbard. I: Internal structure, flow velocity and morphology. *Permafr. Periglac. Process.* **1998**, *9*, 135–145. [CrossRef]
12. Konrad, S.K.; Humphrey, N.F.; Steig, E.J.; Clark, D.H.; Potter, N.; Pfeffer, W.T. Rock glacier dynamics and paleoclimatic implications. *Geology* **1999**, *27*, 1131–1134. [CrossRef]
13. Bucki, A.K.; Echelmeyer, K.A. The flow of Fireweed rock glacier, Alaska, U.S.A. *J. Glaciol.* **2004**, *50*, 76–86. [CrossRef]
14. Bertone, A.; Barboux, C.; Bodin, X.; Bolch, T.; Brardinoni, F.; Rafael Caduff, R.; Christiansen, H.H.; Darrow, M.M.; Delaloye, R.; Etzelmüller, B.; et al. Incorporating InSAR kinematics into rock glacier inventories: Insights from 11 regions worldwide. *Cryosphere* **2022**, *16*, 2769–2792. [CrossRef]
15. Brencher, G.; Handwerger, A.L.; Munroe, J.S. InSAR-based characterization of rock glacier movement in the Uinta Mountains, Utah, USA. *Cryosphere* **2021**, *15*, 4823–4844. [CrossRef]
16. Liu, L.; Millar, C.I.; Westfall, R.D.; Zebker, H.A. Surface motion of active rock glaciers in the Sierra Nevada, California, USA: Inventory and a case study using InSAR. *Cryosphere* **2013**, *7*, 1109–1119. [CrossRef]

17. Kääb, A. Remote Sensing of Mountain Glaciers and Permafrost Creep. *Schriftenreihe Physische Geographie Glaziologie und Geomorphodynamik*; Geographisches Institut der Universität Zürich: Zürich, Switzerland, 2005; Volume 48.
18. Robson, B.A.; MacDonell, S.; Ayala, Á.; Bolch, T.; Nielsen, P.R.; Vivero, S. Glacier and rock glacier changes since the 1950s in the La Laguna catchment, Chile. *Cryosphere* **2022**, *16*, 647–665. [CrossRef]
19. Gärtner-Roer, I.; Brunner, N.; Delaloye, R.; Haeberli, W.; Kääb, A.; Thee, R. Glacier–permafrost relations in a high-mountain environment: 5 decades of kinematic monitoring at the Gruben site, Swiss Alps. *Cryosphere* **2022**, *16*, 2083–2101. [CrossRef]
20. Vivero, S.; Bodin, X.; Farías-Barahona, D.; MacDonell, S.; Schaffer, N.; Robson, B.A.; Lambiel, C. Combination of Aerial, Satellite, and UAV Photogrammetry for Quantifying Rock Glacier Kinematics in the Dry Andes of Chile (30° S) Since the 1950s. *Front. Remote Sens.* **2021**, *2*, 784015. [CrossRef]
21. Lei, Y.; Gardner, A.; Agram, P. Autonomous Repeat Image Feature Tracking (autoRIFT) and Its Application for Tracking Ice Displacement. *Remote Sens.* **2021**, *13*, 749. [CrossRef]
22. Kenner, R.; Phillips, M.; Beutel, J.; Hiller, M.; Limpach, P.; Pointner, E.; Volken, M. Factors Controlling Velocity Variations at Short-Term, Seasonal and Multiyear Time Scales, Ritigraben Rock Glacier, Western Swiss Alps. *Permafr. Periglac. Process.* **2017**, *28*, 675–684. [CrossRef]
23. Heid, T.; Kääb, A. Repeat optical satellite images reveal widespread and long term decrease in land-terminating glacier speeds. *Cryosphere* **2012**, *6*, 467–478. [CrossRef]
24. Delaloye, R.; Lambiel, C.; Gärtner-Roer, I. Overview of rock glacier kinematics research in the Swiss Alps. *Geogr. Helv.* **2010**, *65*, 135–145. [CrossRef]
25. Jones, D.B.; Harrison, S.; Anderson, K.; Betts, R.A. Mountain rock glaciers contain globally significant water stores. *Sci. Rep.* **2018**, *8*, 2834. [CrossRef] [PubMed]
26. Barsch, D. The problem of the ice-cored rock glacier. In *Rock Glaciers*; Giardino, J.R., Shroder, J.E., Jr., Vitek, J.D., Eds.; Allen & Unwin: Boston, MA, USA, 1987; pp. 45–53.
27. Clark, D.H.; Steig, E.J.; Potter, N.; Gillespie, A.R. Genetic variability of rock glaciers. *Geogr. Ann. Ser. A Phys. Geogr.* **1998**, *80*, 175–182. [CrossRef]
28. Ackert, R.P., Jr. A Rock Glacier/Debris-Covered Glacier System at Galena Creek, Absaroka Mountains, Wyoming. *Geogr. Ann. Ser. A Phys. Geogr.* **1998**, *80*, 267–276. [CrossRef]
29. Potter, N.; Steig, E.J.; Clark, D.H.; Speece, M.A.; Clark, G.M.; Updike, A.B. Galena Creek rock glacier revisited—New observations on an old controversy. *Geogr. Ann. Ser. A Phys. Geogr.* **1998**, *80*, 251–265. [CrossRef]
30. Steig, E.J.; Fitzpatrick, J.J.; Potter, N.; Clark, D.H. The geochemical record in rock glaciers. *Geogr. Ann. Ser. A Phys. Geogr.* **1998**, *80*, 277–286. [CrossRef]
31. Meng, T.M.; Petersen, E.I.; Holt, J.W. Rock glacier composition and structure from radio wave speed analysis with dipping reflector correction. *J. Glaciol.* **2023**, *69*, 639–657. [CrossRef]
32. Kunz, J.; Kneisel, C. Glacier–permafrost interaction at a thrust moraine complex in the glacier forefield Muragl, Swiss Alps. *Geosciences* **2020**, *10*, 205. [CrossRef]
33. Bodin, X.; Rojas, F.; Brenning, A. Status and evolution of the cryosphere in the Andes of Santiago (Chile, 33.5° S.). *Geomorphology* **2010**, *118*, 453–464. [CrossRef]
34. Wee, J.; Delaloye, R. Post-glacial dynamics of an alpine Little Ice Age glacitectonized frozen landform (Aget, western Swiss Alps). *Permafr. Periglac. Process.* **2022**, *33*, 370–385. [CrossRef]
35. Potter, N. (Dickinson College, Carlisle, PA, USA). Personal communication, 2022.
36. Östrem, G. Ice Melting under a Thin Layer of Moraine, and the Existence of Ice Cores in Moraine Ridges. *Geogr. Ann.* **1959**, *41*, 228–230. [CrossRef]
37. Petersen, E.I.; Holt, J.W.; Levy, J.S.; Meng, T.M.; Tober, B.S.; Christoffersen, M.; Stuurman, C.M.; Cardenas, B. The transition from Alpine Glacier to Rock Glacier at Sulphur Creek, Wyoming. In Proceedings of the American Geophysical Union Fall Meeting, San Francisco, CA, USA, 9–13 December 2019; Abstract Number C41E–1506.
38. Potter, N.L.; Potter, N.; Retelle, M.J. Continued Movement and Ablation Monitoring, Galena Creek Rock Glacier, Absaroka Mountains, WY. In Proceedings of the Geological Society of America Annual Meeting, Denver, CO, USA, 25 September 2016; Abstract Number 81-14.
39. Nolan, M.; Larsen, C.; Sturm, M. Mapping snow depth from manned aircraft on landscape scales at centimeter resolution using structure-from-motion photogrammetry. *Cryosphere* **2015**, *9*, 1445–1463. [CrossRef]
40. Heid, T.; Kääb, A. Evaluation of existing image matching methods for deriving glacier surface displacements globally from optical satellite imagery. *Remote Sens. Environ.* **2012**, *118*, 339–355. [CrossRef]
41. U.S. Geological Survey. USGS 1/3 Arc Second n45w110: U.S. Geological Survey. 2023. Available online: www.sciencebase.gov/catalog/item/63c78c29d34e06fef14edbd2 (accessed on 13 February 2023).
42. Gesch, D.B.; Oimoen, M.J.; Evans, G.A. Accuracy assessment of the U.S. Geological Survey National Elevation Dataset, and comparison with other large-area elevation datasets—SRTM and ASTER. In *U.S. Geological Survey Open-File Report 2014–1008*; U.S. Geological Survey: Wriston, WV, USA, 2014
43. Debella-Gilo, M.; Kääb, A. Sub-pixel precision image matching for measuring surface displacements on mass movements using normalized cross-correlation. *Remote Sens. Environ.* **2011**, *115*, 130–142. [CrossRef]

44. Wirz, V.; Gruber, S.; Purves, R.S.; Beutel, J.; Gärtner-Roer, I.; Gubler, S.; Vieli, A. Short-term velocity variations at three rock glaciers and their relationship with meteorological conditions. *Earth Surf. Dyn.* **2016**, *4*, 103–123. [CrossRef]
45. Taylor, J.R. *An Introduction to Error Analysis: The Study of Uncertainties in Physical Measurements*, 2nd ed.; University Science Books: Sausalito, CA, USA, 1997.
46. Vivero, S.; Hendrickx, H.; Frankl, A.; Delaloye, R.; Lambiel, C. Kinematics and geomorphological changes of a destabilising rock glacier captured from close-range sensing techniques (Tsarmine rock glacier, Western Swiss Alps). *Front. Earth Sci.* **2022**, *10* , 1017949. [CrossRef]
47. Kaufmann, V.; Kellerer-Pirklbauer, A.; Seier, G. Conventional and UAV-Based Aerial Surveys for Long-Term Monitoring (1954–2020) of a Highly Active Rock Glacier in Austria. *Front. Remote Sens.* **2021**, *2*, 732744. [CrossRef]
48. Davis, P. Holocene glacier fluctuations in the American Cordillera. *Quat. Sci. Rev.* **1988**, *7*, 129–157. [CrossRef]
49. Wiles, G.C.; Jacoby, G.C.; Davi, N.K.; McAllister, R.P. Late Holocene glacier fluctuations in the Wrangell Mountains, Alaska. *Geol. Soc. Am. Bull.* **2002**, *114*, 896–908. [CrossRef]
50. Cuffey, K.M.; Paterson, W.S.B. *The Physics of Glaciers*, 4th ed.; Elsevier: New York, NY, USA, 2010.
51. Monnier, S.; Kinnard, C. Reconsidering the glacier to rock glacier transformation problem: New insights from the central Andes of Chile. *Geomorphology* **2015**, *238*, 47–55. [CrossRef]
52. Petersen, E.I.; Hock, R.; Fochesatto, G.J.; Anderson, L.S. The Significance of Convection in Supraglacial Debris Revealed Through Novel Analysis of Thermistor Profiles. *JGR Earth Surf.* **2022**, *127*, 47–55. [CrossRef]